DISSERTATION

VORTICAL HOT TOWERS, THEIR AGGREGATE EFFECTS AND THEIR RESOLUTION DEPENDENCE IN THE FORMATION OF HURRICANE DIANA (1984)

Submitted by

Juan Marcus Hidalgo

Department of Atmospheric Science

In partial fulfillment of the requirements

For the Degree of Doctor of Philosophy

Colorado State University

Fort Collins, Colorado

Summer, 2007

COLORADO STATE UNIVERSITY

May 1, 2007

WE HEREBY RECOMMEND THAT THE DISSERTATION PREPARED UNDER OUR SUPERVISION BY JUAN MARCUS HIDALGO ENTITLED VORTICAL HOT TOWERS, THEIR AGGREGATE EFFECTS AND THEIR RESOLUTION DEPENDENCE IN THE FORMATION OF HURRICANE DIANA (1984) BE ACCEPTED AS FULFILLING IN PART REQUIREMENTS FOR THE DEGREE OF DOCTOR OF PHILOSOPHY.

Committee on Graduate Work

Gerhard Dangelmayr

Christopher A. Davis

Roger A. Pielke

Wayne H. Schubert

Adviser: Michael T. Montgomery

Department Head: Richard H. Johnson

ABSTRACT OF DISSERTATION

VORTICAL HOT TOWERS, THEIR AGGREGATE EFFECTS AND THEIR RESOLUTION DEPENDENCE IN THE FORMATION OF HURRICANE DIANA (1984)

Recent authors have hypothesized that small-scale deep convective towers possessing intense values of cyclonic vertical vorticity in their cores (vortical hot towers) play a critical role in tropical cyclogenesis via a two stage process: (1) preconditioning the local environment by creating small-scale potential vorticity anomalies and humidifying the lower to middle troposphere, and (2) merger, axisymmetrization and collection of these potential vorticity anomalies to generate the larger scale vortex. In this study we further investigate the role played by vortical hot towers in the upscale growth process. We simulate the evolution of Hurricane Diana in a full-physics numerical model with 1km grid spacing and compare our results to previous, coarser resolution simulations. We employ traditional weather analysis techniques and new innovative means of displaying large and complex datasets to investigate the interaction between the cloud scale features and the larger system scale environment. The results are compared to prior studies to assess if simulated vortical hot tower dynamics exhibit a significant dependence on model resolution.

We find the basic physics of the vortical hot tower pathway is largely unchanged as grid-spacing decreases from 3km to 1km for simulations of Hurricane Diana. The differences between our high resolution simulation and coarser resolution simulations are mainly associated with fine scale variability. Our 1km simulation represents nearly an order of magnitude more convective towers with smaller spatial scales than what was observed in previous simulations. We find maximum updraft velocities in our 1km simulation typically between $15ms^{-1}$ and $20ms^{-1}$ with instantaneous maximum values as high as $35ms^{-1}$, though these values typically decrease during the simulation. We also find that, while the cores in the vortical hot towers are significantly moistened by the vertical transport of moisture in the updraft, the larger-scale environment actually dries significantly due to horizontal advection. Lastly, we examine a series of vortex merger events and find that merger activity is a ubiquitous and important aspect of the genesis of Hurricane Diana. Our results broadly confirm previous work using coarser numerical resolution and provide new insights into the hypothesized upscale growth process in incipient hurricanes.

Juan Marcus Hidalgo
Department of Atmospheric Science
Colorado State University
Fort Collins, Colorado 80523
Summer, 2007

ACKNOWLEDGEMENTS

First and foremost, I would like to thank my adviser, Prof. Michael Montgomery, for providing valuable counseling during this study. He has served as a close friend as well as a mentor to me, and I would not have been able to complete this work without his help. I am in awe of his breadth of knowledge and his passion for the tropical environment and tropical dynamics in particular.

I would also like to thank the remaining members of my committee: Dr. Chris Davis, Prof. Gerhard Dangelmayr, Prof. Roger Pielke, Sr., and Prof. Wayne Schubert. I appreciate your guidance and patience in this endeavor. Dr. Davis in particular provided crucial comments and insights in the early stages of this study with regard to the use of the MM5 mesoscale modeling system.

Lastly I would like to thank my friends and colleagues associated with the Montgomery Research Group including Saurabh Barve, Eric Hendricks, Kevin Mallen, Dr. Richard Moore, Kate Musgrave, Dr. John Persing, Wes Terwey, and Dr. Kevin Tory. I appreciate your friendship and support. I am particularly indebted to Wes Terwey for being available at a moments notice to discuss everything from tropical dynamics to mesoscale meteorology to numerical methods and, of course, football.

Lastly, I would like to think the Air Force for providing financial support for this work. I would also like to thank my fellow Air Force graduate students Rich Buckley, Brian Griffith, Lee Nelson and Tim Nobis for their support and encouragement. Lee Nelson, in particular, has been instrumental in helping me both personally and professionally, and I'm grateful for his friendship.

This work was supported by the Air Force Institute of Technology's Civilian Institute Program and by an NSF Grant ATM 0101781. Computations were performed on NCAR supercomputers blackforest, bluesky and bluevista through a computer time grant provided by the NCAR Scientific Computing Division.

DEDICATION

This work is dedicated to my wife Cindy and my daughters Samantha and Hannah without whose love and support I could not have completed this project. They were particularly understanding during the final year of my program. Trying to graduate while still meeting my obligations as a husband and father has been difficult at best. My family gave me the necessary motivation and support and for that I am forever grateful.

CONTENTS

LIST OF FIGURES

LIST OF TABLES

Chapter 1

INTRODUCTION

Hurricanes generally develop under environmental conditions that include sea-surface temperatures greater than 26°C, low vertical wind shear, cyclonic relative vorticity in the lower troposphere, low-level convergence, and deep convection, among other criteria (Gray 1968; Frank 1987; Montgomery and Enagonio, 1998, hereafter ME98). While these environmental conditions and their impact on hurricane genesis are well documented, comparatively little is known about the fundamental physics of how a weak tropical disturbance organizes into a coherent warm-core cyclone. Our limited understanding is further complicated by the fact that only a small number of convective disturbances actually attain tropical storm status (approximately 80 per year—Gray 1968; Frank 1987; ME98). Furthermore, many genesis events occur over ocean areas where there are virtually no *in situ* observations of the formation process. Both of these realities adversely affect our ability to observe tropical cyclogenesis in great enough detail or at sufficiently fine scales to illuminate the physics that are key to the formation process. As such, comparatively little progress has been made in understanding the key physical mechanism(s) that hastens the transition of a group of discrete thunderstorms into a tropical cyclone. This is in direct opposition to the relatively great strides made in the

science of track and intensity forecasting (see Sheets 1990). Clearly, a better understanding of the fundamental physics of tropical cyclogenesis will have a profound impact on the science of meteorology and will enable forecasters to more accurately predict genesis events by allowing them to focus their efforts on the most likely formation areas.

1.1 Fundamental Theoretical Work

Over the past several years, many studies have focused on the fundamental pathways and precursors to cyclogenesis to include, among others, moistening of the lower atmosphere, the impact of mid-level convective vortices and stratiform convection on the storm environment, the axisymmetrization of potential vorticity anomalies that feed energy and vorticity into the parent vortex and the interaction of deep convective cores with the larger scale environment (i.e. Molinari et. al. 1997; Ritchie and Holland 1997; Bister and Emanuel 1997; Simpson 1997; Montgomery and Enagonio 1998; Ritchie and Holland 1999; Molinari and Vollaro 2000; Enagonio and Montgomery 2001; Dickinson and Molinari 2002; Davis and Bosart 2003; Hendricks et. al. 2004; Montgomery et. al. 2006). Much of this body of work has examined how precursors act as catalysts to generate cumulus convection and then interact with the convection to eventually form the cyclone (here we loosely define tropical cyclogenesis precursors as physical phenomena which consistently precede, on the order of days, the formation of the low-level tropical circulation center and the attendant warm core). Ooyama (1964) and Charney and Eliassen (1964) were among the first to hypothesize a connection between cumulus convection and a developing tropical cyclone through a cooperative interaction process.

Independent of the work of each other, the authors hypothesized a positive feedback between cumulus overturning and the larger scale vortex that was eventually coined conditional instability of the second kind (CISK, Smith 1997). Other studies have demonstrated that the primary mechanism in tropical storm intensification is a transfer of heat by cumulus convection from the ocean surface to the upper troposphere (Ooyama 1969; Rotunno and Emanuel (1987). Emanuel et al. (1994) later termed this intensification mechanism wind induced surface heat exchange (WISHE).

1.2 Early, Idealized Modeling Studies

Other authors have approached the cyclogenesis problem from a slightly different perspective by investigating the role of local and system scale changes induced by cumulus convection and the more indirect effects of these changes on the cyclogenesis process. Montgomery and Kallenbach (1997, hereafter MK97) conducted idealized experiments to investigate the role of convectively generated potential vorticity anomalies in the production of hurricane spiral bands and associated intensity changes. In their study MK97 used a two-dimensional, barotropic, non-divergent, inviscid model of flow on an *f*-plane and demonstrated a mechanism by which radially propagating vortex Rossby waves could intensify the parent vortex. Their proposed intensification mechanism primarily involved wave-mean flow interactions and the axisymmetrization of potential vorticity anomalies into the larger scale cyclone. Montgomery and Enagonio (1998) validated the work of MK97 in a three-dimensional, non-linear, quasigeostrophic model. Further extensions to a rapidly rotating regime were examined by Möller and Montgomery (1999, 2000) using the asymmetric balance model of Shapiro and

Montgomery (1993) and by Enagonio and Montgomery (2001) using a shallow water primitive equation model.

In all of the above studies, the authors relied on basic numerical models of the atmosphere and idealized environmental conditions to better understand the fundamental physics of the cyclogenesis problem. This is a common practice in hurricane research in which simple atmospheric models are coupled with parameterizations of sub grid scale processes to carry out thought experiments related to the tropical environment. In particular, cumulus convection is often parameterized because computer technology has generally not been adequate to fully resolve convective scale processes and the details of their interaction with the larger scale environment. While this type of numerical approximation of the tropical atmosphere often yields promising results in resolving the gross details of the convection and its evolution, the fine scale structure of the convection and its effect on larger scales are often lost.

1.3 Full Physics Modeling Studies

Because of recent advances in computer technology, it is now possible for researchers to use full physics models to perform very high resolution simulations of tropical cyclones (e.g., Liu et al. 1997; Braun 2002). Recent work by Davis and Bosart (2001, hereafter DB01) did just this in their simulation of Hurricane Diana (1984). DB01 used MM5 with 3 nested domains (grid spacing of 81km, 27km, and 9km) and parameterized cumulus convection to successfully simulate Diana as it evolved from its pre-cursor baroclinic origins to a warm core tropical cyclone. The 36 to 48 hour period preceding the development of Diana was characterized by an early season cold front over

the southeastern US that eventually became stationary over and to the east of the Florida peninsula (Bosart and Bartlo 1991). As late as 12UTC 7 Sep 84, approximately 24 hours prior to the actual genesis of the storm, there was no evidence of a low-level circulation center or other environmental condition that would have foretold of the tropical development to come. The combination of a strong upper-level trough, upper-level potential vorticity anomaly and a conditionally unstable airmass overlying warm sea surface temperatures was enough to initiate deep convection very quickly over the genesis region east of Florida. As a result Diana developed rapidly from a weakly baroclinic frontal wave cyclone to a named tropical storm over a 24 to 30 hour period (Tropical Storm Diana was named as of 15UTC 8 Sep 84; Bosart and Bartlo 1991). Since Diana formed close to the Florida peninsula and emerged from its baroclinic origins quickly, the authors initialized the simulation with environmental data obtained from numerous surface observations, ship observations, and vertical soundings. That is, the DB01 simulation of the genesis of Hurricane Diana proceeded without the authors having to insert a bogus vortex into the model's initial conditions. They obtained a reasonable simulation of the storm as verified against the observations reported by Bosart and Bartlo (1991).

Davis and Bosart (2002, hereafter DB02) extended DB01 by investigating the sensitivity of their simulation to various changes in physical parameterizations and input data. DB02 refined their domain structure to include a fourth domain having a near-cloud resolving grid spacing of 3km with explicitly calculated cumulus convection rather than parameterized convection. While providing crucial insights into the physical processes in the tropical atmosphere and the effectiveness of using mesoscale models to

simulate hurricanes (specifically with regard to Hurricane Diana), the work of Davis and Bosart did not allow a detailed examination of the upscale cascade process that occurs as individual thunderstorms interact with the environment and organize into a larger scale vortex. This was due in large part to their necessary use of cumulus parameterizations[1].

1.4 Previous VHT-Focused Modeling Studies

Hendricks et al. (2004, hereafter H04) closed this gap and examined DB02's 3km results to illuminate the fine scale details of Diana's genesis. By focusing on cloud scale convective features and the interaction of these features with the larger scale environment, the authors examined the upscale energy cascade resulting in the formation of the storm. The H04 study was an in-depth examination of deep convective vortical updrafts, which they termed vortical hot towers (VHTs), and the role they played in Diana's genesis. The authors highlighted how these VHTs interact with the environment and feedback on themselves and the emerging larger scale vortex to build the tropical cyclone. H04 suggested that tropical cyclogenesis in Hurricane Diana occurred via a two stage process:

1. Multiple VHTs vortically precondition the local environment by the diabatic production of potential vorticity anomalies from intense convective updrafts. In this stage the VHTs consume and compete with each other for convective

---

[1] Although DB02 (Section 3.e.2, pp, 1111-1116) explicitly represented cumulus convection on their 3km grid, the authors did not focus on the 3km data in their pre-genesis analysis. They mentioned these results primarily in the context of post cyclogenesis.

available potential energy (CAPE) and angular momentum rather than cooperating to generate the storm (H04; Ooyama 1982).

2. The low-level potential vorticity anomalies merge and axisymmetrize to generate the tropical storm scale vortex. The vortex axisymmetrization process in this stage occurs via a quasi-two dimensional manner strongly analogous to barotropic vortex dynamics (H04; McWilliams 1984).

Montgomery et al. (2006, hereafter M06) examined further the role of VHTs in the tropical cyclogenesis process. They posed the genesis problem in terms of the transformation of individual deep convective cores into a warm core vortex through their interaction with a simulated mid-level MCV. Using the Colorado State University Regional Atmospheric Modeling System (Pielke et. al. 1992, Cotton et al. 2003) with resolutions of 2km and 3km and initializing with a single idealized cyclonic MCV, the simulations captured the formation of VHTs and their role in the upscale transfer of convective scale energy to the system scale vortex. They showed that an MCV perturbed non-axisymmetrically by a low-level heat source (a warm bubble) could generate VHTs through the convectively-induced convergence of pre-existing cyclonic vertical vorticity and the tilting and stretching of horizontal vorticity by deep updraft cores (stretching of the pre-existing *vertical* vorticity also occurs). The interaction of the VHTs and the MCV resulted in multiple vortex mergers and axisymmetrization of the potential vorticity anomalies to generate the tropical cyclone (M06). These findings were consistent with the two stage process first proposed by H04 for the Diana case and suggested a pathway

by which a mid-level MCV could foster the tropical cyclogenesis process in a locally quiescent environment.

Although not an investigation of VHTs and their collective impacts on the cyclogenesis process, one additional modeling study must be mentioned. In 2002 Powers and Davis (hereafter PD02) simulated the evolution of Hurricane Diana using MM5 in a single domain configuration at 1.2km grid spacing. The primary goal of this study was to determine the feasibility of using a mesoscale numerical model to simulate hurricane formation and evolution. Comparing their simulation to the 3km results of DB02, PD02 found no significant differences in the larger scale evolution of the storm with regard to track and intensity forecasts. They concluded that, while a coarser resolution simulation ($dx = dy = 3\text{km}$) did indeed capture the broader scale evolution, their fine resolution simulation ($dx = dy = 1.2\text{km}$) was more accurate at capturing the structural elements of the storm (i.e. tangential winds and rain bands). PD02 also concluded that a more realistic simulation of cloud scale features, and not any significant improvements in track and intensity forecasts, was the main benefit of increasing resolution to order $dx = 1\text{km}$ for tropical cyclones. Since there was general agreement in the simulation of the larger scale aspects of the storm, this suggests a convergence of the system scale quantities in the Diana simulations as grid spacing decreases to near 1km. However, the noticeable difference in local-scale (cloud-scale) effects suggests there is potentially much to be learned about the convective scale processes associated with tropical cyclogenesis.

1.5 Recent VHT-Related Observational Studies

While much of the previous work on VHTs and VHT dynamics has focused on

model simulations, a few recent papers have documented the existence of likely VHT structures in satellite, flight level winds and radar data. Reasor et al. (2005) was a study of mesoscale features observed by airborne Doppler radar during the genesis of Hurricane Dolly (1996). The authors presented very convincing evidence of multiple small-scale circulation centers in the pre-Dolly environment with horizontal dimensions on the order of 10-30km and maximum relative vorticity values approaching $50\times10^{-4}s^{-1}$. The observational data presented and the analysis performed provided strong support that mesoscale circulations and, in particular, VHT dynamics played a significant role in the formation of the Hurricane Dolly.

Hendricks et al. (2006) mainly used rapid scan visible satellite imagery and scatterometry data and in their study of the mesoscale features associated with the genesis of Tropical Storm Gustav (2002). Due to the lack of radar coverage over the storm, satellite data proved invaluable in observing and inferring the mesoscale nature of the genesis process. The environmental wind over the genesis area occasionally sheared off the upper-level clouds and revealed an unobstructed view of the low-level clouds and associated low-level circulation. During one such shearing episode, two clearly defined meso-vortices approximately 25km-45km in diameter emerged from underneath deep convective regions and were observed in the low-level cloud features (see Figure 1.1). Since these vortices had similar temporal and spatial scales as the observed convective cores (deduced from overshooting tops in the cirrus shield), since the meso-vortices emerged from underneath deep convection and since there are no islands in the genesis region to generate lee vortices, the authors surmised the low-level circulation centers must have been formed by the stretching of vertical vorticity by intense convective

updrafts as in H04 and M06 (Hendricks et al. 2006). Thus, this study provided a satellite based observation of the genesis associated VHT activity complementing the Reasor et al. (2005) radar based observations.

Sippel et al. (2006) also used radar data in their study of the formation of Tropical Storm Allison (2001), but they relied primarily on land based Doppler radar supplemented with airborne radar, satellite observations and surface observations to achieve continuous coverage of the genesis process. Allison formed very near the Texas coast in early June 2001, and genesis was captured completely by the Houston/Galveston NWS NEXRAD Doppler radar (Sippel et al. 2006). This allowed the authors a nearly unrestricted view of the genesis process with remotely sensed data (and limited *in-situ* observations). Within Allison's genesis region, they found several meso-scale vortices (identified by the radar velocity displays) with horizontal dimensions that ranged from the meso-β (10-100km) to the meso-γ (1-10km). Many of these vortices were generally collocated with areas of strong precipitation and, as such, were most likely vortical hot towers (particularly the smaller meso-β and larger meso-γ vortices). The authors, however, found that the convection was neither deep nor intense enough to warrant hot tower status, and, as a result, referred to these vortices as "convective burst vortices" to distinguish them from VHTs and MCVs. They also presented evidence of potential merger events as the smaller scale vortices were advected around the developing larger scale flow with two to three of them appearing to consolidate over the time period examined. The Sippel et al. (2006) study is important because it is likely the first observational study of tropical cyclogenesis able to resolve apparent VHT convective and vortical structures with sizes on the order of 1km and it provides further support for the

VHT tropical cyclogenesis pathway.

1.6 The Current Study

In the present study we build on the work of DB02, PD02, H04 and M06 and further examine the formation process of Hurricane Diana with MM5 configured to have a grid spacing of 1km on its finest grid and explicitly calculated cumulus convection. Based on the near convergence of large scale features seen in PD02 and on the recommendation of Bryan et al. (2003) regarding the resolution necessary to adequately model deep convection, the 1km grid spacing for this simulation allows us to more fully investigate the upscale growth, self-organization, and local and system scale processes involved in genesis of Hurricane Diana. In this simulation we focus on VHT dynamics and thermodynamics and investigate the impact of vortical hot towers on tropical cyclogenesis and the system scale environment. We assess whether or not the VHT theories presented by H04 and M06 change as we approach true cloud resolving scales. We also examine the genesis process itself to determine if the formation of Diana was inherently "bottom-up" or "top-down." Additionally, we extend the theories of H04 and M06 regarding the life cycle of vortical hot towers, their characteristic maximum values of vorticity and vertical velocity, and the impacts of vortex mergers on tropical cyclogenesis. Our overarching goal is this study is to determine if the VHT pathway to tropical cyclogenesis simulated in H04 and M06 has a sensitive dependence on model resolution.

The outline of the dissertation is as follows. Chapter 2 describes the configuration of the model and outlines the experiments that were performed. In Chapter 3 we discuss the

output of the model from a larger scale perspective. We first compare our simulated Hurricane Diana to the observational data set of Bosart and Bartlo (1991) and then to the modeled data sets of DB01, DB02, PD02, and H04. An overview and analysis of the smaller scale features (i.e. meso-α, 100km to 1,000km scales) is discussed in Chapter 4. In Chapter 5 we present an assessment of the convective scale features and focus on individual VHTs and their evolution and impact on the larger scale environment. Interpretation of the results, a summary of conclusions and recommendations for future work is presented Chapter 6.

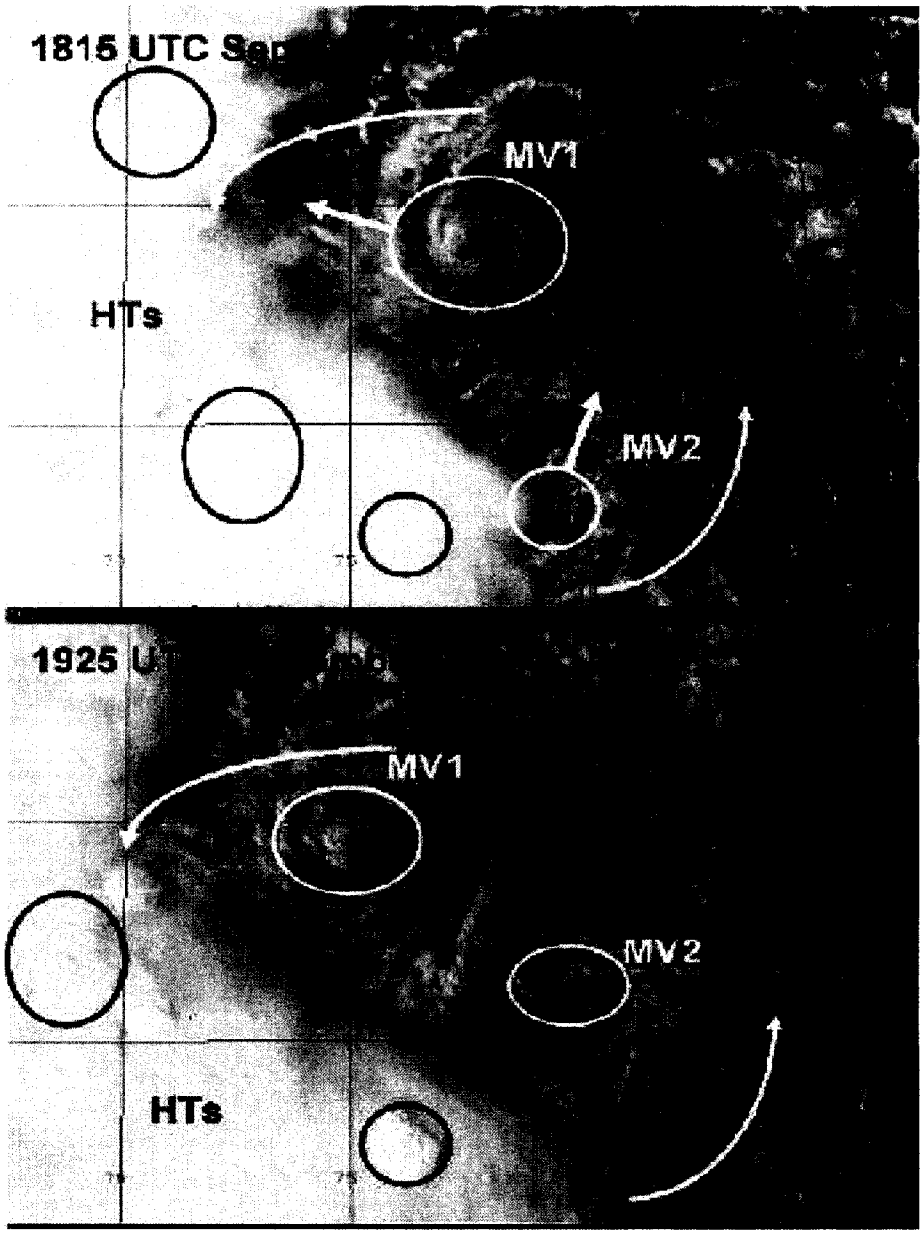

Figure 1.1. Visible satellite image of Tropical Storm Gustav at 1815UTC (upper) and 1925UTC (lower) on 9 Sep 2002. Both images cover a geographic area with dimension 110km (N-S) by 94km (E-W) (Taken from Figure 6 of Hendricks et al, 2006).

Chapter 2

DESCRIPTION OF THE MODEL

2.1 Introduction

The model used for this study is version 3.7.2 of the Pennsylvania State University-National Center for Atmospheric Research (PSU-NCAR) fifth generation mesoscale model (MM5) as described in Grell et al. (1994). This model is nonhydrostatic, compressible and integrates the primitive equations via leapfrog time stepping with an Asselin filter—see Appendix for a description of the model equations. In this study we performed a number of experiments which will be described in the following sections.

2.2 Model Configuration

2.2.1 Control Run—1km Grid Spacing (denoted Diana1)

For our control experiment we employed a domain structure with four nested domains of increasing spatial and temporal resolution (two-way nests). The outermost domain was configured to cover most of North America and portions of the Atlantic and Pacific Oceans, while the subdomains progressively focused more on the eastern United States and on the Western Atlantic just east of Florida (see Figure 2.1). Horizontal grid

spacing for the coarsest domain was 27km on a grid 180 by 300 gridpoints (north-south by east-west). Nested domains had horizontal grid spacing of 9km, 3km and 1km on grids sized 350 by 301, 343 by 322, and 508 by 490 gridpoints, respectively. Throughout this text, we refer to each domain in the control simulation (and all simulations) by its grid spacing (i.e. 27km grid, 9km grid, etc.).

The size of the 27km grid was chosen to represent the synoptic scale forcing of the atmosphere and to cover, as closely as possible, the same geographic area covered by the coarse domains in DB01, DB02, and H04 (see Figure 2.2). However, the 27km grid was not used during our control experiment; data from this grid was used for initialization of the model only. Boundary and initial conditions files were created based on data for the 27km grid and then interpolated to the 9km grid (the first inner nest). As a result the coarsest domain in our numerical simulations was actually the 9km grid, with necessary files interpolated from the larger 27km outer grid. This was done in an effort to conserve computer resources while still capturing the essence of atmospheric large scale forcing outside of the southeastern United States and western Atlantic Ocean. Additionally, this step was necessary to be consistent with previous modeling studies of Diana (DB01, DB02, H04). That is, previous studies of Hurricane Diana used an outermost domain similar to our 27km grid. While we don't employ the 27km grid in our numerical simulation, the use of data from the 27km grid to initialize our 9km grid provides a level of consistency with previous studies.

Each domain employed 37 terrain following σ levels with vertical grid spacing of order 100m near the surface gradually increasing to approximately 4,000m near the model top (p = 50hPa). The time step for the outermost domain in the numerical

simulation (9km grid) was set to 15sec with time steps of 5sec and 1.667sec for the 3km and 1km grids, respectively. Subgrid scale processes were represented by the following schemes: Medium Range Forecast (MRF) boundary layer scheme of Hong and Pan 1996, Dudhia radiation scheme (Dudhia 1999) and the Numerical Weather Prediction Explicit Microphysics scheme (NEM) of Schultz (1995). As in DB01, DB02 and H04, cumulus convection on the 9km grid is represented by the Kain-Fritsch cumulus parameterization scheme (Kain and Fritsch 1990), while cumulus convection on the 3km and 1km grids was explicitly represented.

2.2.2 Rerun of Hendricks et al., 2004—3km Grid Spacing (denoted Diana3)

In addition to the 1km control run mentioned above, we also performed a coarser resolution simulation repeating the control experiment of H04[2] This was necessary for 2 reasons: 1) it provided a baseline of data against which to compare our 1km results and 2) the establishment of the 3km baseline was necessary because H04 used version 2.0 of MM5 and we used version 3.7.2. Rather than use previous results from a different model release to assess the effect of resolution on the VHT process, we recreated the H04 simulation with MM5 version 3.7.2 and performed a more meaningful comparison in which differences due to model versions did not have to be addressed.

The domain structure was the same as specified in DB02 and H04 and was nearly identical to the aerial coverage in our 1km experiment (see Figure 2.1 and Figure 2.2). The horizontal grid spacing on the outermost domain was 81km on a grid 60 by 100

[2] The H04 study did not actually integrate the model in time. Rather, H04 analyzed the output data from the 3km grid of DB02. As such, the coarser simulation run we performed in this case is more technically a rerun of the DB02 numerical simulation.

gridpoints (north-south by east-west). Nested domains had horizontal grid spacing of 27km, 9km and 3km on grids sized 91 by 91, 151 by 133, and 148 by 148 gridpoints, respectively. The vertical structure of each domain was identical to the Diana1 experiment with 37 terrain-following σ levels from the lower surface to the model top of 50hPa. The time step for the outermost domain was set to 120sec with time steps of 40sec, 13.33sec and 4.44sec for the 27km, 9km and 1km grids, respectively. Subgrid scale processes were represented by the following schemes: MRF boundary layer scheme of Hong and Pan (1996), Dudhia radiation scheme (Dudhia 1999) and the NEM Microphysics scheme of Schultz (1995). To maintain consistency with the DB01, DB02 and H04 experiments, cumulus convection on the 81km, 27km and 9km grids was represented by the Kain-Fritsch cumulus parameterization scheme (Kain and Fritsch 1990). Cumulus convection on the 3km grid was explicitly calculated.

2.2.3 Rerun of Diana3 Without Surface Fluxes—3km Grid Spacing (denoted Diana3noflx)

This sensitivity experiment was set up exactly as the Diana3 experiment using MM5 with one major exception. In an attempt to determine if the VHT pathway to tropical cyclogenesis is pre-WISHE, we configured the model such that the latent and sensible heat fluxes from the surface layer of the model were completely turned off. This was achieved via a namelist variable in the MM5 input files. All other aspects of this simulation including initial condition, boundary conditions, objective analysis technique, domain configuration and cumulus parameterization were identical to the Diana3 experiment.

2.3 Initial Condition

The initial condition for all model runs was based on data from the NCAR/National Center for Environmental Prediction (NCEP) re-analysis project with data adjusted to account for surface and upper air observation via objective analysis. Sea surface temperatures (SST) were based on observed Navy SSTs with adjustments made east of the Florida peninsula for the hand analyzed SSTs of DB01 (which were based on buoy data). All experiments were initialized at 12UTC 7 Sep 84, 27 hours prior to the naming of tropical storm Diana by the National Hurricane Center at 15UTC 8 Sep 84 (Lawrence and Clark, 1985).

2.3.1 Diana1 Experiment

The 9km and 3km grids were initialized at 12UTC 7 Sep 84 (t = 0h) while the 1km grid was initialized at 00UTC 8 Sep 84 (t = 12h). Objective analysis of observations into the model initial conditions was accomplished via a multiquadric objective analysis scheme (Nuss and Titley 1994). It is worth noting that our initial conditions are based on observed and re-analyzed environmental variables only; that is, no bogus vortex was inserted into the initial data to generate a tropical storm.

2.3.2 Diana3 Experiment

To be consistent with the DB02 and H04 studies, the 81km, 27km and 9km grids were initialized at 12UTC 7 Sep 84 (t = 0h) while the 3km grid was initialized at 09UTC

8 Sep 84 (t = 21h). As in the case of our Diana1 simulation the model initial conditions are based on observed and re-analyzed environmental variables only; no bogus vortex was inserted into the initial data to generate a tropical storm.

Objective analysis of observations into the model initial conditions was accomplished via a Cressman objective analysis scheme (Cressman 1959). The reason for the different objective analysis schemes was due to the performance of the methods at different scales. We completed the Diana3 experiment before attempting the Diana1 experiment and used the Cressman objective analysis scheme. When we proceeded to work on the Diana1 experiment, we initially used the Cressman method in our objective analysis step. However, this method produced artificial bulls-eyes in the initial fields regardless of the radii of influence used. As a result we decided to use the multiquadric objective analysis scheme of Nuss and Titley (1994) and found the results to be acceptable without any of the bulls-eyes seen with the Cressman scheme. It is important to note that we also reran our Diana3 experiment using the Nuss and Titley objective analysis method to determine if slightly different initial conditions would affect the model results. We found the results of the 3km simulation showed no significant differences regardless of objective analysis method used. Nonetheless, to be consistent with DB02 and H04, the results presented in this dissertation for the Diana3 experiment are those that use the Cressman objective analysis method to ingest observations into the initial first guess fields.

All other details of the numerical experiment were the same as discussed in DB02 and H04 (i.e. physical parameterizations and input data) with one exception. Our first attempt at repeating the H04 results did not generate a tropical storm by t = 60h. After

extensive consultations with Dr. Chris Davis at NCAR, we found that the mid and low-levels of our model were initially too dry relative to observations and remained too dry throughout the simulation. This is easily seen in Figure 2.3 in which we compare observed soundings for Cape Kennedy, Florida (Bosart and Bartlo 1991), to an initial sounding for the same location in our Diana3 simulation (note that the dashed sounding in Figure 2.3a is valid 3 hours prior to the sounding in Figure 2.3b). While both the observed and simulated soundings are similar, there is an observed saturated layer between roughly p = 600hPa and p = 700hPa at 09UTC 7 Sep (Figure 2.3a, dashed line) that is noticeably drier in our Diana3 initial sounding (Figure 2.3b). Since both our simulation and the DB02 simulation used the same data to initialize the model, our first thought was that this discrepancy was most likely the result of changes in the model between version 2.0 and version 3.7.1, though we could not find a specific change to the model that would tend to retard the tropical cyclogenesis process.

We then examined our objective analysis method and found a small number of observations were being excluded because of the threshold values we applied to accept/reject observations. Consequently, we adjusted our threshold values and increased our radii of influence slightly to enable observations to have a larger impact on the first guess fields. The end result was the same; no tropical vortex developed by the end of the simulation. As a last resort, we decided to artificially moisten the low-levels of the atmosphere in the region of the model where we observed the apparent lack of moisture and where Diana was observed to form according to H04, DB02 and Bosart and Bartlo (1991). In this region (see Figure 2.4), we modified the initial relative humidity field such that the values were increased by 20% between 600hPa to 925hPa, though we

limited the maximum allowed relative humidity to be 103% (3% supersaturation). The degree of moistening on the boundaries of the box was adjusted to increase gradually from 2.5% to 20% so as not to introduce a step function into the model initial conditions. As a result, low and mid-level moisture values in our simulation were more consistent with observations (see Figure 2.3 and Figure 2.5). And, when the model was rerun with these adjusted initial moisture fields, a tropical cyclone developed with an evolution and storm track that was broadly consistent with the H04 and DB02 simulations.

2.3.3 Diana3noflx Experiment

Initial condition for this simulation was exactly the same as in the Diana3 experiment to include the artificial moistening of the initial low level moisture fields in the genesis region.

2.4 Additional Considerations

To the author's knowledge, our control simulation is believed to be the first numerical study investigating the convective scale aspects of tropical cyclogenesis in a full physics model with 1km grid spacing. While Powers and Davis (2002) used MM5 with 1.2km grid spacing to simulate the evolution of Hurricane Diana, their focus was not on the formation stage and the associated convective scale kinematic and thermodynamic processes supporting Diana's transformation into a tropical storm. This important study focused mostly on the feasibility of using mesoscale numerical models for forecasting tropical cyclogenesis, with a particular emphasis on the numerical prediction of track and

intensity. Our work complements the work of PD02 quite nicely by focusing on the role of mesoscale and convective scale features in the tropical cyclogenesis process, and in particular, the genesis of Hurricane Diana.

Except otherwise noted (i.e., for plots or computations taken from H04 or DB02), we use the output from our 3km experiment (Diana3) in performing new calculations or creating new plots for the H04 simulation. We must also point out explicitly that the artificial moistening of the initial relative humidity field was only performed on data for the H04 rerun (Diana3). In our finer resolution simulation (Diana1) we did not artificially adjust the initial conditions in any way to generate the storm.

Finally, we would be remiss were we not to mention some of the more logistical aspects of this study, and in particular, our control experiment. We performed our Diana1 simulation on NCAR's bluesky computer and ran the model out to t = 60h (00UTC 10 Sep 84) with temporal resolution for the output data of $\Delta t = 10\,\text{min}$. Based on file size and wall clock limitations on the NCAR computers, this single simulation ran over a period of 3 weeks (via 13 restarts) and generated over 250Gb of raw data.

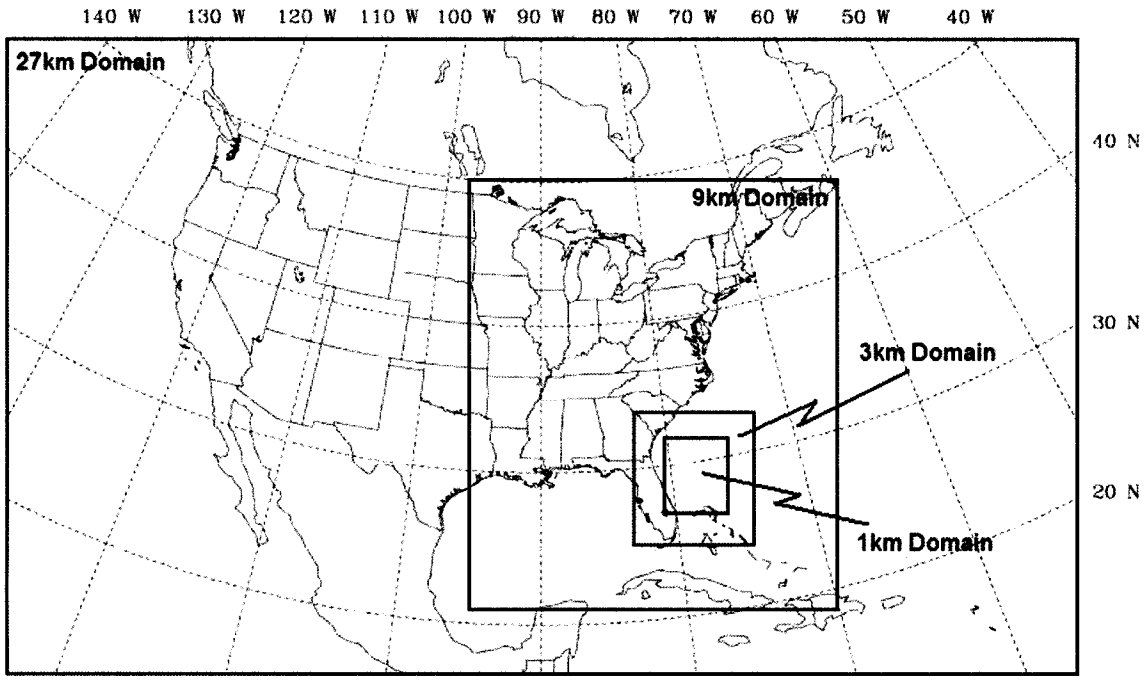

Figure 2.1. Approximate geographic locations of all domains in the Diana1 experiment. Only the 9km, 3km, and 1km grids were used in the numerical simulations. The 27km grid was used in creating initial and boundary condition files which were then interpolated to the 9km grid. During the model evolution, the 9km grid was the outermost domain (the 27km grid was inactive).

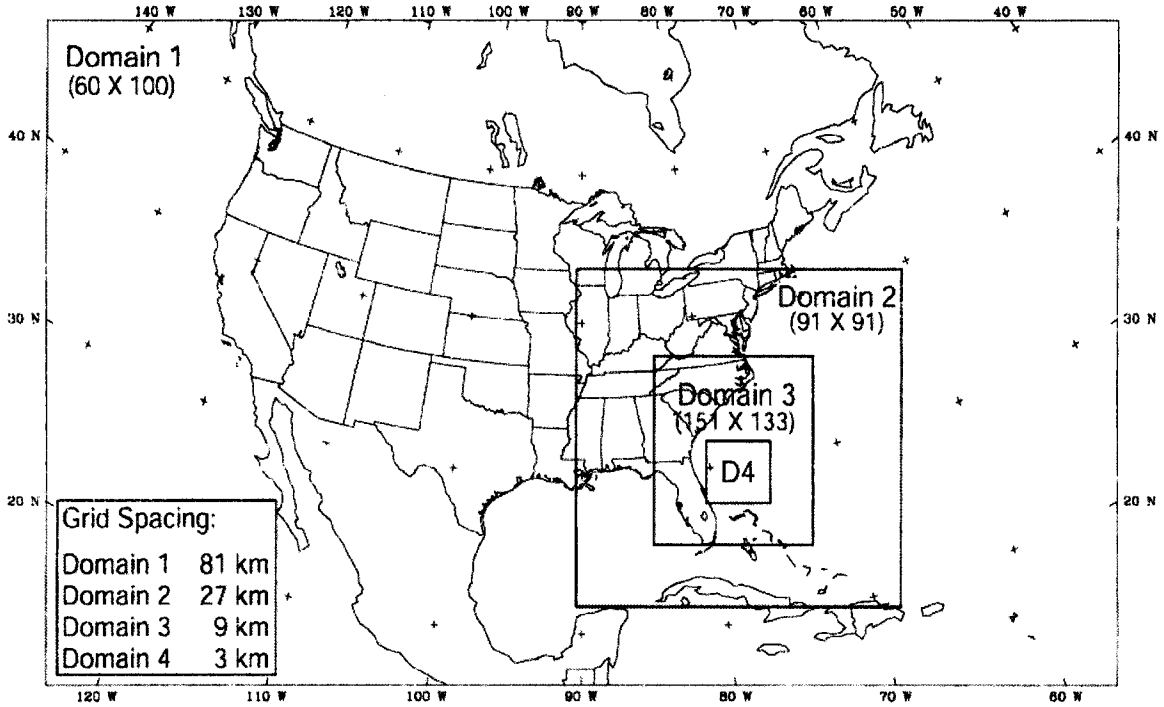

Figure 2.2. Approximate geographic locations of all domains in the Diana3 and Diana3noflx experiments (Taken from Figure 1 of DB02).

Experiment	Inner Nest Grid Spacing	Outer Nest Grid Spacing	MM5 Version	Comments
DB01	9km	81km	2.0	
DB02	3km	81km	2.0	Extension of DB01 experiment with addition of 3km inner nest. Authors performed several sensitivity studies relative to DB01.
PD02	1.2km	1.2km	2.0	Single domain simulation with 1.2km grid spacing.
H04	3km	81km	2.0	Data used in this study was from 3km grid of the DB02 run.
Diana1	1km	9km*	3.7	
Diana3	3km	9km*	3.7	Rerun of DB02/H04 case using MM5 version 3.7.
Diana3noflx	3km	9km*	3.7	Latent and sensible heat fluxes turned off in surface layer.

*Initial conditions, lateral boundary conditions and lower boundary conditions for these runs were based on a data from a larger 27km outer domain. The 27km domain was only used to initialize the model and generate boundary condition files. It was not active during the simulation.

Table 2.1. Summary table of numerical experiments examined and/or referred to in this dissertation.

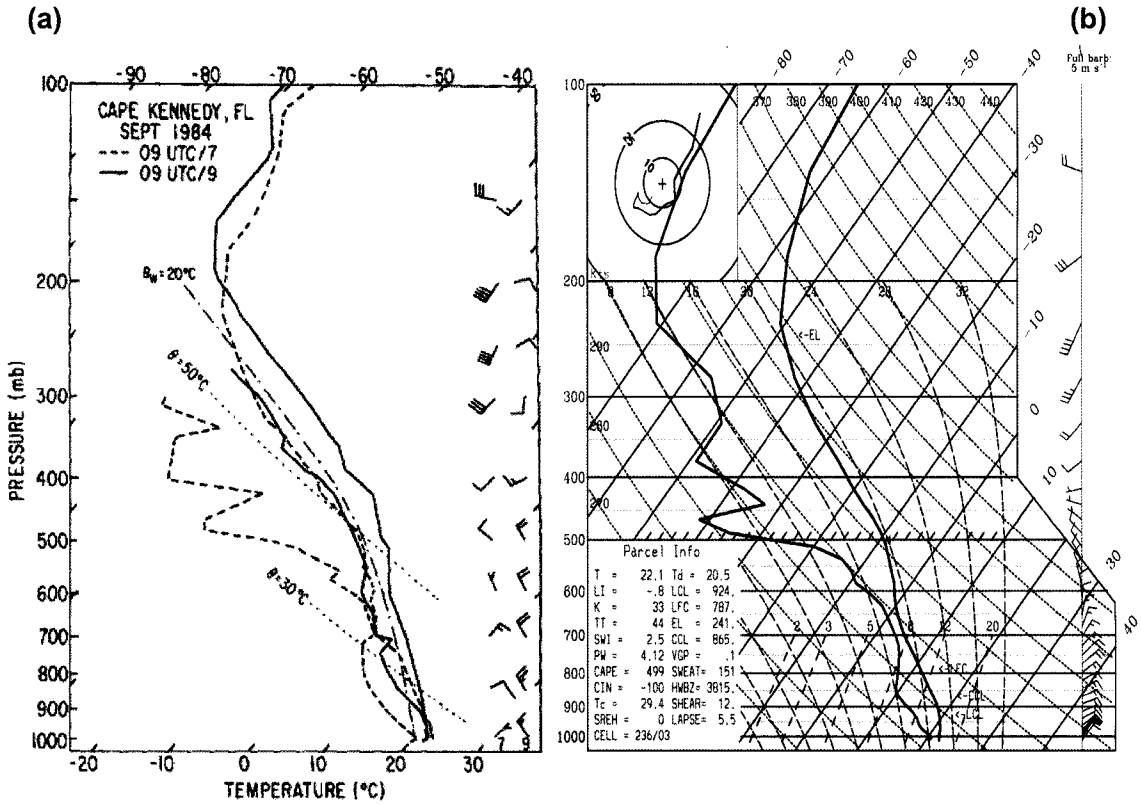

Figure 2.3. (a) Vertical sounding observed at Cape Kennedy, FL (KXMR) at 09UTC 7 Sep 84 (dashed line) and 09UTC 9 Sep 84 (solid line, taken from Figure 10 of Bosart and Bartlo 1991). (b) Vertical sounding at KXMR for the Diana3 experiment at 12UTC 7 Sep 84 (t = 0h) *before* the atmosphere was artificially moistened. Notice the saturated layer between 600hPa and 700hPa in (a) is present but noticeably drier in (b).

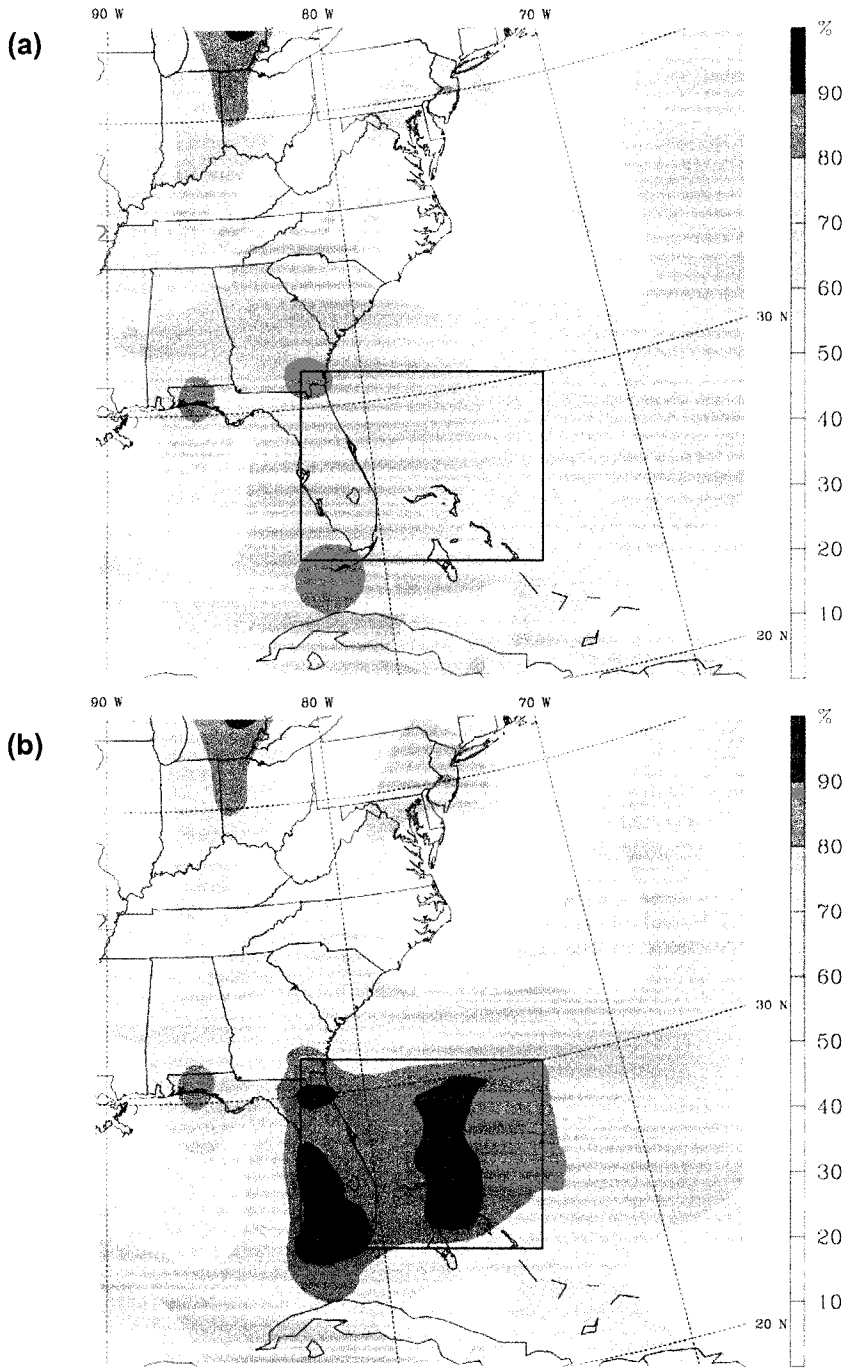

Figure 2.4. Plot of initial relative humidity values at 850hPa for the Diana3 and Diana3noflx experiments. The data is plotted on the 27km grid for (a) the case of the original moisture field before the artificial moistening occurred and (b) the moisture field that resulted after the atmosphere was artificially moistened. The black box indicates the geographic region over which we increased the low and mid-level moisture values.

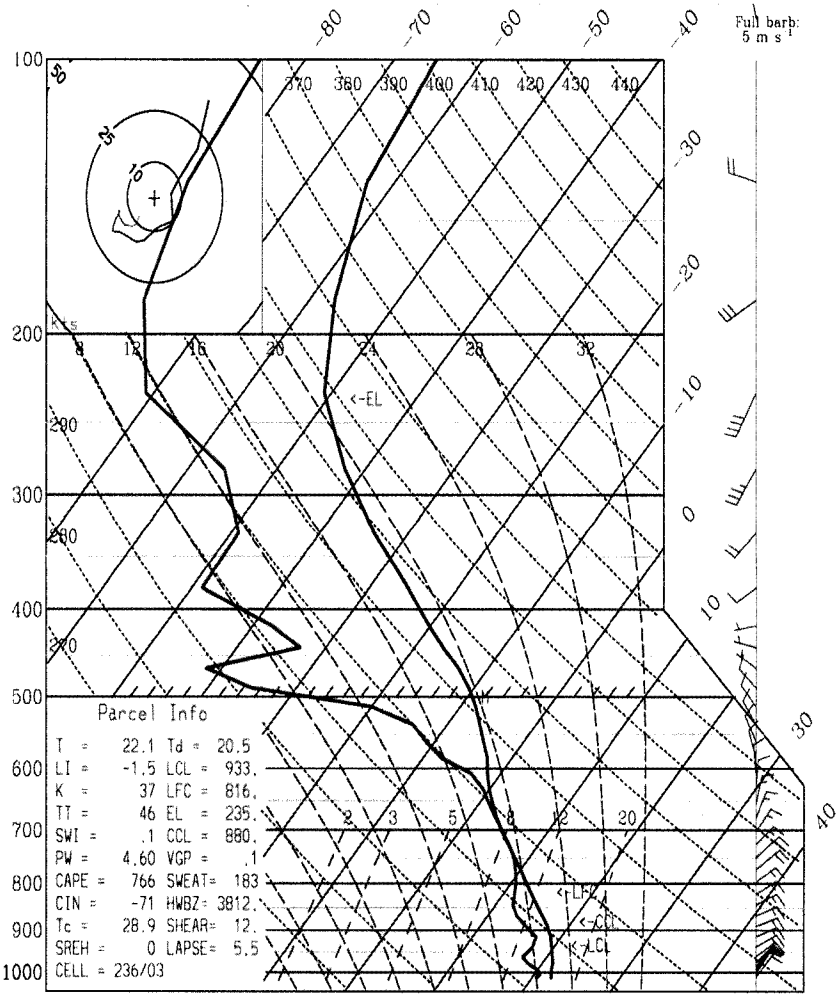

Figure 2.5. Vertical sounding at KXMR for our Diana3 simulation *after* the atmosphere was artificially moistened. Compare this sounding to Figure 2.3 and note the increase in moisture below 600hPa and the representativeness of this sounding to Figure 2.3a.

Chapter 3

SIMULATED EVOLUTION OF SYNOPTIC FIELDS

3.1 Introduction

A full description of the observed synoptic and mesoscale environmental conditions leading up to the formation of Hurricane Diana can be found in Bosart and Bartlo (1991). In this chapter we focus on the evolution of our simulated hurricane from pre-cyclogenesis to the formation of a warm core cyclone that eventually became Hurricane Diana. With the intent of verifying the model output, we compare our model data to the observations documented in Bosart and Bartlo (1991) and to the results of previous modeling studies. In most of the analysis that follows we focus on data from the Diana1 experiment and generally restrict our discussion to the 9km grid for descriptions of the initial condition and the evolution of synoptic fields. The description of the initial model condition is solely from the Diana1 simulation. When necessary to examine finer scale aspects of the simulation we also present selected output from the 3km grid of Diana1. In the last two sections of this chapter, for completeness, we briefly discuss results from our 3km simulations, though this is not the primary focus of the chapter.

3.2 Initial Condition

3.2.1 Surface and Low-Level Features

The initial sea-level pressure and surface wind fields for the 9km grid (see Figure 3.1a) indicate a weak convergence zone east of the Florida peninsula associated with the remnants of a cold front that moved through the southeastern United States in the previous 24 hours and stalled off the Florida coast north of the Bahamas (see Figure 3.2). A surface high pressure system north of this convergence zone is centered over the New England states bringing an early season cold outbreak across the entire eastern seaboard. Associated with this anticyclone, winds off the east coast of the US have a strong northerly component with speeds as high as $15ms^{-1}$ due to the tight pressure gradient east of the US mainland. Over the New England states along the axis of a high pressure ridge and extending south and southwestward from the anticyclone center, light and variable winds are observed. These lighter wind speeds extend into the southern states and gradually increase in strength farther to the south over the Gulf of Mexico where moderate easterly flow is observed. From the mid-west through the Great Lakes region, the surface pressure gradient tightens again, and this results in significant southerly flow with wind speeds up to $15ms^{-1}$. More important to the study at hand, the surface conditions over the Bahamas indicate a noteworthy inverted trough with marked cyclonic curvature of the surface wind field extending south across Cuba into the Caribbean Sea.

Though the model initial conditions were not dynamically balanced after objective analysis (as was done in DB01, DB02, and H04), the surface winds generally follow the isobars of sea-level pressure with an expected component of the flow toward lower

pressure resulting from surface friction. The main exceptions to this occur in the Gulf of Mexico, over eastern Oklahoma, over the Bahamas and south of Newfoundland where there is obvious wind flow through small-scale closed isobars that vaguely resemble bullseyes. Additionally, there is notable cross-isobaric flow where very strong pressure gradients exist off the coast of Virginia and over the mid-western United States. [NOTE: By t = 1h (not shown) these bullseyes in sea-level pressure are no longer apparent. And, by t = 12h (Figure 3.1b) the sea-level pressure field is close to a dynamically balanced state as measured by the degree to which the surface winds are nearly parallel to the sea-level pressure isobars. Examining hourly plots of sea-level pressure and surface winds, this near balance state appeared as early as t = 6h (not shown).]

The post-frontal anticyclonic structure of the low-level wind and pressure fields off the eastern seaboard is also reflected in the low-level vorticity field observed at model initialization. Figure 3.3 is a plot of absolute vertical vorticity on the 925hPa pressure surface at t = 0h. This plot indicates the existence of an elevated region of positive low-level vorticity (greater than $7.5\times10^{-5}s^{-1}$) extending from the Bahamas northward to Newfoundland. The presence of this region of higher vorticity values can be attributed primarily to the strong pressure gradient in the western Atlantic Ocean and the convergence zone farther south along the old frontal boundary. This pool of relative high vorticity will prove to be important in the simulation as deep convective updrafts are generated which then converge and intensify the pre-existing vorticity to generate the vortical hot towers, a subset of which ultimately consolidate and form the warm core cyclone. This finer scale aspect of the simulation will be discussed in greater detail in Chapter 4.

3.2.2 Mid and Upper-level Features

Let us now turn our attention to the mid and upper-levels and examine initial geopotential height, wind and temperature patterns on the 9km grid. While similar conditions are observed at both 500hPa and 300hPa, we focus our attention on the 300hPa surface since conditions are more prominent at this level in the atmosphere (i.e. deeper pressure and temperature anomalies and stronger wind speeds at 300hPa compared to 500hPa—see Figure 3.4 and Figure 3.5). The initial conditions at upper-levels indicate a significant pressure trough over the Florida peninsula with strong south-southwesterly flow over much of the Bahamas. This trough is part of a deeper low pressure area centered over the New England states where the strongest pressure gradients and winds speeds are observed. The southern flank of the trough over Florida, particularly at the p = 300hPa pressure level, exhibits strong cyclonic curvature and is associated with a significant upper-level low pressure anomaly such that the trough closely resembles a cut-off low. Maximum wind speeds at upper-levels are $25ms^{-1}$ to the east of the trough axis with generally weaker winds to the west of the axis suggesting that the trough is still deepening at the time of model initialization.

Associated with this upper-level anomaly and probably more important for genesis of the storm is the structure of the potential vorticity (PV) field over the eastern United States. The initial isentropic PV field ($\theta = 340K$, see Figure 3.6) shows a significant positive anomaly with closed contours over the southeastern U.S. Peak values are greater than 2.5 PVU over the eastern U.S and greater than 5 PVU over northern Florida. This positive PV anomaly is coupled with a deep upper-level thermal trough that extends from

the northeast along the eastern seaboard into the Caribbean (see Figure 3.4 and Figure 3.5). Though difficult to see due to the limited geographic coverage, mid and upper-level temperatures in this trough are at least 4°C colder than the environment indicating a potential source of upper-level forcing and convective instability over the region. Vertical soundings over the genesis area reflect this potential for convective instability. Figure 3.7 shows initial vertical soundings at Cape Kennedy, Florida (KXMR), and West End, Grand Bahamas (MYGW). Both soundings indicate a conditionally unstable atmosphere with nearly all indices signifying the potential for convective activity. The MYGW sounding reflects 1249 J kg^{-1} of mixed layer CAPE with 57 J kg^{-1} of CIN while the KXMR sounding only shows 522 J kg^{-1} of mixed layer CAPE with 87 J kg^{-1} of CIN. Other locations sampled in and around the genesis region show the same trend with larger values of CAPE observed to the east near the Bahamas and smaller values observed west along the Florida coast, in general. Thus, the vertical structure of the atmosphere over the entire genesis area indicates significant upper and lower level forcing such that widespread convective activity should be expected to breakout shortly after model initialization.

One rather curious aspect of the initial model sounding over Cape Kennedy that we must mention is the relative lack of low and mid-level moisture relative to the observations in Bosart and Bartlo (1991, see Figure 2.3a). Recall from our discussion of the model configuration in Chapter 2, we had to artificially moisten the low-levels of the model atmosphere in the Diana3 simulation in order for the model to generate a tropical cyclone in a reasonable amount of time. However, for our Diana1 simulation, this was not necessary despite the even drier initial condition observed in the vertical sounding

relative to both observations and the Diana3 simulation (compare Figure 2.3 and Figure 3.7). The only difference between the Diana1 and Diana3 experiments (aside from slightly different domain configurations) was grid spacing. Both simulations used the same source data to generate the initial condition files and perform objective analysis, and both models were configured with the same physics packages. Yet, the coarser resolution simulation required enhanced moisture in the low to mid-levels in order to generate a warm-core vortex. This implies that the Diana1 experiment is capturing an aspect of the tropical atmosphere, in general, and the tropical cyclogenesis process, in particular, that is not fully simulated in the Diana3 experiment.

Finally, just as the initial surface plots displayed notable areas of imbalance in the flow field due to the ingest of observations by the objective analysis scheme, the wind and geopotential height fields at 300hPa and 500hPa also exhibit a noteworthy amount of dynamical imbalance (in the sense that there are areas with a significant degree of ageostrophic flow). This is particularly true over the Great Lakes region where the objective analysis scheme has adjusted the initial conditions to generate small scale wavelike structures in the geopotential height field that are not supported by the wind field. Fortunately, by t = 1h into the simulation (not shown) near-geostrophic balance in the mid and upper-level flow fields is restored and there is little suggestion of a strong ageostrophic component of the winds by t = 6h (not shown). This was similar to the timing of the adjustment process at the surface. Since near-geostrophic balance was restored very early on in the simulation, we feel this imbalance in the initial conditions does not adversely affect our results.

These initial conditions are broadly similar to what would be expected in the vicinity

of a baroclinic disturbance and have not been adjusted in any way to facilitate the development of a tropical cyclone. Furthermore, there is no vortex apparent in the eventual Diana formation area east of Florida. And, no feature in the initial conditions suggests that tropical development is imminent other than perhaps the inverted surface pressure trough that extends from the Bahamas into the Caribbean Sea. Additionally, we have not inserted a bogus vortex into the initial field to stimulate the formation of a warm core low. This last step is not necessary since other studies by DB01, DB02, PD02, and H04 have shown that MM5 can effectively simulate the genesis of Diana without having to initialize the model with anything other than re-analysis data and observations. Comparing our initial conditions to these previous modeling studies of Diana and to the observational study by Bosart and Bartlo (1991), we are convinced our model initialization is well representative of the environmental conditions existing 24 to 48 hours prior to the formation of Hurricane Diana.

3.3 Diana1 Simulation

3.3.1 Sea-Level Pressure and Surface Winds

During the first 36 hours of the simulation (12UTC 7 Sep 84 to 00UTC 9 Sep 84), the synoptic scale sea-level pressure pattern and surface wind field remain largely unchanged north of 30N. The surface anticyclone in the northeastern United States migrates slightly to the northeast and maintains a central pressure on the order of 1031hPa +/- 2hPa (see Figure 3.1). The central pressure in the surface high is initially 1032hPa and fluctuates by 2 to 3hPa over the course of the simulation before achieving a

central pressure of approximately 1031hPa at t = 36h. Associated with the motion of the anticyclone toward the east, the trough over the southeastern United States becomes more positively tilted with a slight strengthening of the surface pressure gradient east of Florida. As a result of the tightened gradient, winds to the north of the Bahamas intensify while maintaining their cyclonic curvature.

South of 30N, the synoptic sea-level pressure pattern exhibits more obvious changes that are due primarily to the development of Diana as it evolves into a tropical storm rather than the motion/intensity changes associated with the surface anticyclone to the north. The inverted trough in the initial fields over the Bahamas becomes enhanced as closed contours of sea-level pressure emerge by t = 12h. And, by t = 24h the sea-level pressure pattern and surface winds field east of Florida indicate a moderate vortex with maximum wind speeds on the order of 20ms^{-1} north of the local pressure minimum of 1013hPa (see Figure 3.1c). While the maximum winds are tropical storm strength at this point in the simulation, the corresponding absolute vorticity field indicates the system is just beginning the vortex merger/axisymmetrization process (see Figure 3.14c, this will be discussed in greater detail in Section 3.3.4). The actual genesis of Diana appears to occur between 12UTC 8 Sep 84 (t = 24h) and 15UTC 8 Sep 84 (t = 27h) as indicated by the formation of concentric contours of sea-level pressure, a distinct closed circulation center, and the axisymmetrization of several low-level intense vorticity anomalies into a single vorticity core (see Figure 3.8). This is consistent with the analysis of Bosart and Bartlo (1991) who indicated Tropical Storm Diana was named at approximately 15UTC 8 Sep 84 based primarily upon ship observed wind speeds of 15-20ms^{-1} at this time (Lawrence and Clark 1985). During the remaining portion of the model evolution, the

simulated Tropical Storm Diana intensifies somewhat as a result of the axisymmetrization of additional vorticity anomalies and begins to move toward the southwest until it makes landfall around 00UTC 9 Sep 84 (t = 36h) near Fort Pierce, Florida. The storm then turns toward the north-northeast (Figure 3.1d)[3].

3.3.2 Mid and Upper-Level Features

At 500hPa the cyclone centered over the northeastern United States migrates toward the east in parallel with the motion of the surface anticyclone (see Figure 3.5). For the first 20 hours of the simulation (not shown), the mid-level cyclone appears to maintain its intensity as it moves eastward, although we can not be absolutely certain of this as the center of circulation appears outside of the bounds of the 9km grid and is not clearly visible. By t = 24h (Figure 3.5c) the cyclone center moves more toward the south, becomes visible on the 9km grid and clearly indicates the mid-level cyclone has begun to fill. During the same 24hr period, the more southerly anticyclone over Louisiana also

---

[3] Although the timing of cyclogenesis and the initial intensity of our simulated storm are in good agreement with the observational analysis of Bosart and Bartlo (1991), the later phases of the storm life cycle are not well simulated (see Figure 3.9). This is particularly true during the intensification phase which occurs after t = 36h in our simulation. While observations show Diana deepened to a central pressure of approximately 993hPa by 00UTC 10 Sep 84 (t = 60h in our simulation, Bosart and Bartlo 1991) our simulated storm only deepened to 1005hPa by this same time. Additionally, the storm track of our simulated Diana displays a marked departure from the observed storm track between 18UTC 8 Sep 84 (t = 30h) and 12UTC 9 Sep 84 (t = 48h, see Figure 3.9). While these departures from observations are noteworthy, the focus of this study is on storm genesis and not intensification per se. This departure from observation notwithstanding, we feel our simulation of the genesis of the storm is representative of environmental conditions that existed during the formation of Hurricane Diana and provides valuable insights into the physics of tropical cyclogenesis in a baroclinic environment. The applicability of these findings to cyclones that develop in the deep tropics is the subject of an ongoing study and is beyond the scope of this work.

migrates toward the east and clearly broadens such that by the end of this period, almost the entire eastern seaboard is under the influence of ridging conditions at mid-levels. The exception to this trend is over Florida where the mid-level trough in the initial conditions has persisted despite the broad-scale ridging conditions. By t = 24h this trough of low pressure is more dynamically connected to the energetics of tropical cyclogenesis occurring at the surface than it is connected to the mid-level cyclone over Newfoundland (see Figure 3.1c and Figure 3.5c).

Examining Figure 3.5, it becomes clear that the most significant changes in the mid levels occur during the first 24 hours of the simulation. After this time, only modest changes are observed in the geopotential height, wind, and temperature fields. The mid-level anticyclone over the Gulf of Mexico weakens slightly but maintains a closed circulation center, the mid-level anticyclone over the New England states intensifies slightly and, over the genesis area, the mid-level cyclone deepens only slightly after t = 24h. The only other significant change of note after t = 24h occurs in the temperature field. After this time mid-level temperatures show a distinct warming trend as all cold temperature anomalies south of 30N that were initially associated with the mid and upper-level cold dome have been eroded by the convective activity and associated latent heat release.

At 300hPa the trends in the geopotential height fields are broadly similar with a few exceptions (see Figure 3.4). The upper-level ridge that initially extended from the Gulf of Mexico through the Great Lakes region broadens in parallel with the 500hPa ridge, but the degree of broadening at 300hPa is not as widespread. Additionally, the upper-level trough over the genesis area, while fracturing from the upper-level cyclone in the

northeast, fills slightly. Of particular note at upper-levels is the evolution of the temperature anomaly aloft and the corresponding upper-level PV ridge (see Figure 3.10). As deep convection is generated, strong vertical motion transports heat upward and begins to erode the upper-level cold dome as early as 00UTC 8 Sep 84 (t = 12h, Figure 3.4 and Figure 3.5b). By 12UTC 8 Sep 84 (t = 24h) the upper-level cold dome and PV anomaly over the genesis area are almost entirely obliterated by the action of this convective activity. However, not all of the upper-level forcing has vanished. By the end of the first 24 hours of the simulation, a small weakly organized area of colder temperatures and relatively higher PV values persists over southern Florida (Figure 3.4c and Figure 3.10c). The remnants of the initial upper PV anomaly persists until t = 36h while the upper-level temperature anomaly has been entirely obliterated by this point in the simulation (this will be discussed in greater detail in Section 3.3.4).

3.3.3 Vertical Velocity and Moisture Fields

While the sea-level pressure, geopotential height, wind, and temperature fields show only moderate changes, the synoptic scale evolution of other variables is quite dramatic. As one might expect due to the existence of upper-level forcing and convectively unstable vertical soundings, variables indicative of convective activity display a rather interesting evolution during this phase of development. Figure 3.11 is a plot of the vertical velocity field at 500hPa on the 3km grid. Because of the scale of the updraft cores, we choose to focus on data from the 3km grid to provide the reader a more detailed view of the vertical motion field. The 500hPa surface was chosen since H04 discovered in their simulation of Diana that the maximum updraft values were observed near an

altitude of z = 5km. By 00UTC 8 Sep 84 (t = 12h, Figure 3.11b), widespread convection has erupted throughout the genesis area with approximately 50 updraft cores visible off the east coast of Florida (in fact, isolated convective cores were visible in the genesis region as early as 18UTC 7 Sep 84, t = 6h, not shown). This outbreak of convection is generally oriented along the old frontal boundary/convergence zone observed in the initial sea-level pressure and wind fields (Figure 3.1a) where the initial elevated values of low-level absolute vorticity were observed (see Figure 3.3a). The convective activity persists throughout the simulation though the intensity of the convection lessens after the initial burst at t = 12h. And, the updraft cores propagate to the north and east with most of the strongest vertical velocity cores observed near 75W by the 36 hour point in the simulation.

At mid-levels the effect of the convection on the moisture field is noteworthy. As we did for the vertical velocity due to the size of the cores, we again chose to investigate the data on the 3km grid. The eastern coastal areas of Florida are initially dry at 500hPa with relative humidity values generally less than 50% (see Figure 3.12a). Over the course of the simulation, this mid-level moisture field is significantly modified such that, by t = 24h into the simulation (12UTC 7 Sep 84), much of the east coast of Florida has relative humidity values greater than 90%, particularly south of Cape Kennedy (see Figure 3.12c). If one closely examines the plots of 500hPa vertical velocity compared to the plots of relative humidity at the same level (Figure 3.11 and Figure 3.12, respectively), it becomes obvious that the areas with the strongest upward motion values are directly linked to areas of the largest increases in relative humidity. This suggests that the deep convection erupting in the genesis region is transporting moisture upward

from the surface and humidifying the mid-levels of the atmosphere. This moistening mechanism is consistent among each of the four panels plotted in Figure 3.11 and Figure 3.12. We also examined other time periods in the output data and found the collocation of vertical velocity cores and relative humidity "cores" to be consistent throughout the simulation on the 3km grid.

The moistening of the mid and upper-levels by the convection is further evidenced by examining the vertical soundings over Cape Kennedy, a location to the west of the genesis area but still in the vicinity of the convective activity. The initial vertical sounding at this location (Figure 3.7a) indicated relatively dry conditions through the column with typical values of dew point depression on the order of 5°C, particularly up through $p \approx 550\text{hPa}$. Above this level were the driest conditions with typical dew points are on the order of 15 °C to 20 °C colder than the temperature values. By 24 hours into the simulation the vertical sounding at Cape Kennedy (Figure 3.13) shows significant moistening throughout the column with typical dew point depressions reduced to approximately 1°C or less, particularly at mid and upper-levels (above p = 500hPa). Slightly drier conditions exist at lower levels though the entire column is significantly moistened by t = 24h such that typical values of dew point depression are on the order of 1-2°C compared to the 4-5°C dew point depression values initially observed. We surmise the primary mechanism responsible for the moistening of mid and upper-levels in and around the eventual genesis area is the convection that erupts shortly into the simulation which acts to transport moisture upward from the ocean surface.

3.3.4 Vorticity Field

The absolute vertical vorticity field also has the signature of the convection with dipoles of positive/negative vorticity anomalies collocated with the convective updraft cores. To investigate these features more closely, due to their horizontal dimension, we again have chosen to examine plots from the 3km grid (see Figure 3.14). Coincident with the convective cores visible at t = 24h, we see highly vortical cores evident over the entire genesis region. These are the result of the deep convection tilting horizontal vorticity into the vertical and stretching this vertical vorticity to create strong anomalies (M06). Comparing Figure 3.11, Figure 3.12 and Figure 3.14 the reader can visually confirm that these high vorticity cores (both positive and negative) are collocated with the deep convective updrafts. Maximum values in the positive vorticity cores are on the order of $3.5\times10^{-3}s^{-1}$ with the largest negative values on the order of $-2.5\times10^{-3}s^{-1}$. By visual inspection the aerial coverage of the positive vorticity cores seems equal or greater than aerial coverage of the negative vorticity cores. Coupled with the generally positive background vorticity, we expect the average vorticity over the genesis area has increased in magnitude since the initialization of the model due to the action of the convection (H04). We perform explicit calculations to verify or refute this change in aggregate vorticity in Chapter 4.

As the simulation progresses over the next 12 hours in association with the genesis of Hurricane Diana, the absolute vorticity field takes on a different character. This is evident as early as t = 24h when the aerial extent of the low level negative vorticity is significantly less than earlier in the simulation. While there are still clear regions with anticyclonic vorticity anomalies, the area of the domain with cyclonic absolute vorticity is much larger and more widespread despite the fact that the number of strong cyclonic

vorticity core has decreased slightly. By t = 36h, the absolute vorticity field has become concentrated in two regions of the domain: a line of convection on the eastern side of the domain that is propagating away from the genesis region and has little consequence on the genesis of Diana, and a concentrated area of increased vorticity values associated with the developing tropical storm just east of Lake Okeechobee on the western side of the domain. The western area of elevated vorticity has a strong central core with maximum value of approximately $3.8\times10^{-3}s^{-1}$ and a band of elevated vorticity north of the core spiraling into the central vortex. The structure of this vortex is such that the area in the immediate vicinity of the vortex (within 100km of the center) has a strong positively bias with only 1 to 2 negative vorticity anomalies visible to the south and southeast of the storm center. Additionally, the structure of the low level vorticity field by t = 36h is such number of positive vorticity anomalies is also limited with many of them on the western side of the domain having been axisymmetrized into the emerging master vortex associated with Hurricane Diana.

We now turn our attention to the evolution of the upper-level potential vorticity on the θ = 340K surface (see Figure 3.10). During the early stages of the model evolution, this upper-level forcing was important in initiating the widespread convection and subsequent VHT activity. And, as a result, the net effect of the convective cores is to nearly annihilate the upper-level PV anomaly due to the upward transport of heat. Very early on in the model evolution (as early as t = 6h, not shown), the upper PV anomaly is permeated by the deep convection, and this convective activity begins to erode the PV anomaly. Much of the anomaly is annihilated by t = 12h, but, throughout the simulation, a small area of positive upper-level PV remains intact over southern Florida. This

remaining upper-level PV anomaly plays an important role in the genesis phase of Diana's development. This is explained in the following paragraph.

As the Tropical Storm Diana begins to emerge around t = 24h to t =27h, the cyclone is initially weak and disorganized with a circulation center not clearly visible in the sea-level pressure data (Figure 3.1c and Figure 3.8a). Additionally, while VHTs are present at this time, the intensity of these cores appears to have waned somewhat in terms of number density, aerial coverage, and maximum vorticity values since the initial surge in convective activity around t = 12h (Figure 3.11b, c and Figure 3.14b, c). As the center of circulation moves toward the west and southwest during this early genesis period, the cyclone moves under the remaining upper-level PV anomaly at approximately t = 27h (15UTC 8 Sep 84, Figure 3.8c and Figure 3.10c). A second burst of convective activity is subsequently generated, and multiple new VHTs and VHT merger events occur. This action helps to organize the tropical cyclone resulting in the birth of Tropical Storm Diana at approximately t = 27h into the simulation.

It is important to note that the PV anomaly that persists over southern Florida throughout the genesis phase is associated with a cyclone that originated as part of the mid-level fractured trough visible in the initial fields (see Figure 3.5). As the simulation progresses this fractured trough deepens into a mid-level cyclone over southern Florida that persists throughout much of the genesis phase. Concurrent with the deepening mid-level vortex, the development of tropical depression Diana progresses such that the storm moves toward the southwest under this mid-level cyclone and, once under this vortex, it is then that we see a distinct consolidation/merger of absolute vorticity into a central core (i.e., t = 27h see Figure 3.8d). This is broadly consistent with the findings of M06 who

showed that a pre-existing mid-level vortex is a critical ingredient in the generation of vertical hot towers and the subsequent cascade of energy from the VHT scale to the system scale in tropical cyclogenesis.

3.4 Diana3 Simulation

In this section we present a very brief summary of the Diana3 synoptic evolution. We will focus mainly on the differences between the Diana3 results and the Diana1 results already discussed in this chapter and will analyze only a few key output parameters. Furthermore, we restrict our discussion to the pre-cyclogenesis and genesis phases of development since the initial conditions for both simulations are based on the same dataset of NCEP/NCAR reanalysis data and observations (aside from the adjustments to the relative humidity field discuss in Section 2.3.2). For all parameters the domain of each plot differs between the two experiments. However, we have attempted to choose output from a grid of the Diana3 simulation which matches as closely as possible the plots presented thus far in this chapter (in terms of geographic coverage). This requires that we examine output from the 27km grid of the Diana3 simulation (see Figure 2.2) to be compared against output from the Diana1 9km grid generally presented thus far.

3.4.1 Sea-Level Pressure Field and Surface Winds

We begin with the evolution of the sea-level pressure field. Figure 3.15 shows plots of sea-level pressure and surface winds at synoptic output times from t = 0h to

t = 36h. We compare these plots against Figure 3.1 and first note that the domains are different in terms of aerial coverage. The upper left corner of plots from the Diana3 simulation (Figure 3.15 and others that follow) roughly corresponds to the triple intersection point common to the states of Minnesota, Iowa and Wisconsin. While the lower right of plots from both simulations is roughly at 18°N and 70°W, though the eastern boundary of the Diana3 plots is roughly 100km to 200km further east. It is important to keep these differences in geographic coverage in mind when comparing output data. Notwithstanding the differences in the plotting areas, the evolution of sea-level pressure for both simulations is nearly identical outside of the genesis area. Both simulations maintain a surface anticyclone centered over the New England states with center pressures on the order of 1031hPa +/-2hPa and with maximum surface winds east and west of this high pressure region near $15ms^{-1}$. In both numerical experiments, the surface anticyclone migrates slightly toward the east while maintaining ridging conditions over nearly the entire eastern seaboard. The only noticeable difference in the evolution of the anticyclone north of about 30°N occurs near t = 24h (Figure 3.1c and Figure 3.15c) when the Diana1 simulation tends to intensify the central pressure 2-4hPa greater than what is observed for the Diana3 simulation. Further south in the genesis region, the differences in the sea-level pressure evolution are much more dramatic. While the Diana1 simulation generates a very modest storm with wind speeds near $15ms^{-1}$ north of the storm center with a central pressure near 1010hPa by t = 36h, the Diana3 simulation creates a significantly stronger storm. The simulated Tropical Storm Diana becomes evident in the sea-level pressure and surface wind field as early as t = 12h in the Diana3 simulation (Figure 3.15b) when we see closed isobars and a distinct

cyclonic circulation emerge in the wind field. By t = 24h, a clear center and corresponding surface low develops (central pressure ~ 1004hPa) and is beginning to intensify. By t = 36h in the Diana3 simulation (Figure 3.15d) the central pressure has fallen to 999hPa and surface winds are symmetric about the apparent storm center with maximum values approximately 20ms^{-1}, though winds are slightly stronger to the north because of the proximity of the storm to the previously mentioned surface anticyclone.

3.4.2 Mid-Level Geopotential Height, Winds and Temperature

The differences in the simulations are much more subtle when we examine plots of mid-level (p = 500hPa) geopotential height, winds and temperature in each simulation (Figure 3.5 and Figure 3.16). Both the Diana1 and Diana3 experiments indicate the presence of a mid-level cyclone initially centered over the New England states. This cyclone is further associated with a mid and upper-level trough over the southeastern United States which was previously shown to play a noteworthy role in the genesis process. Over the course of each simulation, the mid-level cyclone migrates quickly toward the east such that, by t = 36h, the initial trough axis that extended from the northeast through the Florida peninsula is replaced by weak ridging conditions. The exception to this is off the east coast of Florida where the mid-level trough in the initial conditions has deepened to a closed low associated more closely with the tropical cyclogenesis at the surface. The mid-level circulation center is located near 30N and 80W and is more obvious in the Diana3 simulation than in the Diana1 simulation (as to be expected since the 3km numerical experiment developed a much deeper tropical cyclone at the surface). The deeper intensity of the warm core low at the surface is

further reflected in the evolution of the 500hPa temperature field which clearly shows the annihilation of the mid-level temperature trough and the corresponding emergence of a warm anomaly by $t = 36$h. This discrepancy in the strength of the mid-level vortex is the main difference between the two simulations at mid-levels. Other aspects of the simulations observed at mid-levels in the atmosphere are generally the same.

3.4.3 Low-Level Absolute Vorticity Field

For the analysis of the low-level absolute vorticity field, we've chosen to investigate data plotted on the 9km domain of the Diana3 simulation. The reasons for this minor modification are 1) to resolve the details of the vorticity field which are not readily observed on the larger grids and 2) to be consistent with the absolute vorticity plots already presented in this chapter for the Diana1 simulation (consistent in terms of aerial coverage). Figure 3.17 is a plot of low-level absolute vorticity (p = 925hPa) from the Diana3 simulation at synoptic output times from $t = 0$h to $t = 36$h. Comparing this figure to the corresponding figure from the Diana1 simulation (Figure 3.14), the reader will immediately notice major differences in the nature and evolution of the low-level absolute vorticity field for each simulation. The first and likely most obvious difference is the number of resolved anomalies. The time periods plotted in Figure 3.17 indicate approximately 3-5 eddies ($\eta \geq 1.2 \times 10^{-3} s^{-1}$) are resolvable at any one time in the simulation (this is consistent at other output times as well). Contrast this with the number of anomalies present in the Diana1 plots, and it becomes clear that the 1km simulation is resolving an order of magnitude more anomalies. Additionally, the size of the resolved eddies are much larger in the Diana3 simulation than in the Diana1 simulation. This

difference is obvious visually when comparing Figure 3.14 against Figure 3.17. However, the difference is the eddy size is even more dramatic when one considers the geographic coverage of the plots in Figure 3.14 is nearly twice as large as the geographic coverage of Figure 3.17 (329,000km^2 compared to 178,000km^2). If the absolute vorticity plots in Figure 3.17 were then mapped to the grid for the plots in Figure 3.14, the vorticity anomalies in the Diana3 simulation would then appear nearly twice as large. Thus, the eddies resolved in the Diana3 simulation are significantly larger than the anomalies resolved in the Diana1 simulation. Both of these differences (number and size of the anomalies), though, could be expected since the number of gridpoints over a given area in the Diana1 simulation is nine times the number of gridpoints for the same area in the Diana3 simulation.

What is not expected is the difference in intensity, and, in particular, the number of *anticyclonic* eddies resolved in each simulation. While the Diana3 simulation is devoid of virtually any anticyclonic anomalies in the field,[4] the Diana1 simulation contains nearly as many negative vorticity cores as there are positive vorticity cores. And, the strength of the anomalies in each simulation is also significantly different. Many of the negative anomalies in the Diana1 simulation have minimum values that are quite significant though not quite as large as the magnitude of the positive anomalies ($\eta \approx -2.5\times10^{-3}\,s^{-1}$ compared to $\eta \approx 3.5\times10^{-3}\,s^{-1}$). These anticyclonic cores permeate the domain in the Diana1 simulation and result in a highly textured appearance to the low-level absolute vorticity field. This is in stark contrast to the smooth and nearly

[4] According to M06 negative anomalies must be present in the flow due to the dipole structure that results from tilting horizontal vorticity into the vertical. These anomalies are either too small or too weak to be captured by the lowest contour level.

continuous region of anomalous cyclonic vorticity present in the genesis region of the Diana3 simulation. Minimum negative vorticity values in the region are generally $\eta \approx -0.4\times10^{-3}\,s^{-1}$, almost an order of magnitude weaker than in Diana1, and occur in very limited areas in the domain.

Finally, we must also mention the differences in the strength of the cyclonic absolute vorticity anomalies, which are significant, though not as dramatic as for the anticyclonic cores. The Diana1 simulation produces vorticity anomalies with maximum values greater than $\eta \approx 3.5\times10^{-3}\,s^{-1}$, while the magnitude of the maximum vorticity anomalies in the Diana3 simulation are approximately $\eta \approx 2.0\times10^{-3}\,s^{-1}$, roughly two-thirds of the Diana1 maximum values.

Aside from the differences in the general appearance and intensity, the evolution of the vorticity field exhibits further significant differences between the two simulations. Both simulations exhibit similar characteristics important to the tropical cyclogenesis process (cyclonic vorticity anomalies develop and a subset of those merge to form the tropical vortex), but the path taken to the end state differs in each experiment. While the Diana1 simulation shows significant cyclonic and anticyclonic anomalies forming as early as t = 6h (not shown), similarly strong vorticity anomalies (i.e., an order of magnitude or greater than background values) don't form in the Diana3 simulation until approximately t = 16h (not shown). Further examination of the Diana3 output reveals only 3-5 strong low-level absolute vorticity anomalies are present at any given time. The main vortex that forms at the end of the simulation is the result of the merger of these intermediate vortices. And, by the end of the Diana3 simulation, the entire field of absolute vorticity is dominated by the central tropical vortex with no additional strong

vorticity anomaly apparent in the domain. In contrast, the Diana1 simulation reveals on the order of 20-50 cyclonic and anticyclonic vorticity anomalies present in the field at a given time with only a small subset of these merging to form the tropical vortex. Furthermore, by the end of the Diana1 simulation, the absolute vorticity field maintains its highly textured appearance such that the tropical vortex, while still dominant, has a size that is only slightly larger than the vorticity anomalies elsewhere in the domain.

3.4.4 Mid-Level Relative Humidity Field

We next investigate differences in the evolution of the mid-level relative humidity fields between the Diana1 and Diana3 simulations. Recall that the initial conditions in the Diana3 simulation included an artificial moistening of the low to mid-levels of the atmosphere (20% increase in relative humidity in the layer between p = 900hPa and p = 600hPa, see Section 2.3). In our analysis of the relative humidity fields, we attempt to isolate, as much as possible, differences that may arise from this different initialization scheme and present data from above the artificially moistened layer at p = 500hPa. We recognize this will not remove the effect of the additional low-level moisture since convective updrafts will likely transport low-level moisture upward. However, since we are concerned with understanding the atmosphere associated with hurricane formation, *how* the moisture field evolves in an environment that supports tropical cyclogenesis is of prime importance. Since the un-moistened Diana3 simulation did not generate a tropical vortex, we would not have the ability to investigate the scale dependent nature of the cyclogenesis process without artificially modifying the initial moisture field for the Diana3 simulation. We remind the reader that artificial moistening of the atmosphere

was not necessary for our control simulation, Diana1.

An analysis of Figure 3.12 and Figure 3.18 reveal the evolution of the mid-level moisture fields for both simulations are very similar. The main differences that arise do not seem to be dependent on the artificially increase of moisture at low to mid-levels. Rather, it would appear from the plots that the biggest differences in the evolution of mid-level relative humidity arise due to the location and strength of the updraft cores in the simulation and the location of the emerging tropical cyclone center of circulation. Relative humidity plots from the Diana1 experiment (Figure 3.12) show the effect of the deep convective updrafts on the moisture field as they transport low-level moisture upward and moisten the mid and upper-levels of the atmosphere. That is, the location and size of the deep updraft cores in the mid-level vertical velocity field (Figure 3.11) correspond quite well with the areas of supersaturation in the relative humidity field (Figure 3.12). In the plots of relative humidity in the Diana3 simulation, we do not observe a similar feature despite the additional moisture source available at low-levels. In fact, Figure 3.18 indicates only a very isolated number of areas of supersaturation in the Diana3 simulation while Figure 3.12 shows numerous localized areas of supersaturation permeating the entire relative humidity field. This would suggest the updrafts observed in the Diana1 simulation are deeper, more intense, and/or more widespread than the Diana3 updrafts.

A second difference in the relative humidity fields can be attributed to the location of the circulation center and its effect on the horizontal advection of the moisture. Recall from Figure 3.9 that the storm in the Diana1 simulation had begun moving toward the south-southwest by t = 36h and made initial landfall just north of Miami before moving

back toward the north. Examining the evolution of the absolute vorticity field for the Diana3 simulation (Figure 3.17), we see that this storm moved toward the north-northwest by t = 36h, in direct contrast to the track of the Diana1 storm. This difference is reflected in the plots of relative humidity at t = 36h (see Figure 3.18d and Figure 3.12d). The more northerly position of the storm in the Diana3 simulation is indicated by high relative humidity bands that appear to spiral into the center of circulation near 30N; the more southerly position of the storm in the Diana1 simulation is also indicated by banded moisture features that appear to spiral into the center of circulation just north of Miami, FL. These moisture bands are indicative of rain bands associated with the developing storm and are the result of the combined effects of vertical transport by the deep updraft cores and the horizontal advection of moisture into and around the storm environment (while relative humidity is not a conserved variable, it does give us insight into the vertical and horizontal motions occurring at this level in the atmosphere).

Despite differences in these more specific details of the relative humidity fields, the evolution of relative humidity is consistent between the two simulations. Both numerical experiments exhibit consistent features: 1) the maximum of relative humidity initially located to the northeast of the genesis center is advected into the storm environment and is modified and further moistened by the deep updraft cores, 2) high relative humidity/rain bands are observed at the end of each simulation after the storm has developed, and 3) the existence of a relatively dry slot of air to the south of the circulation center (trajectories suggest much of this dry air originated to the north behind the weak front, not shown). Much of the observed differences can be attributed to local effects of the convective cores and to differences in the simulated storm track.

3.5 Diana3noflx Simulation

Finally, we briefly analyze the output from our 3km simulation in which all latent and sensible hear fluxes from the surface layer were turned off in an attempt to assess if the VHT pathway to tropical cyclogenesis is a pre-WISHE process. That is, we examine the Diana3noflx output to determine if a signature of VHT activity develops without the flux of latent and sensible heat from the ocean surface. If indeed we see VHT like structures developing along with a general increase of vorticity in the genesis region, this would suggest that the VHT route to tropical cyclogenesis occurs before wind dependent surface fluxes are allowed to interact with the genesis process and amplify the developing vortex.

The evolution of the low level absolute vorticity field over the last 12 hours of the Diana3noflx simulation (t = 36h and t = 48h) is presented in Figure 3.19. At first glance, it would appear this simulation has not created any features that resemble the VHTs produced in the Diana1 and Diana3 experiments, particularly if one focuses solely on the output from the 9km grid. However, a close examination of the 3km output (the bottom row in Figure 3.19) reveals that indeed VHT signatures (i.e. intense vorticity anomalies) have developed in the field by t = 48h. However, we note the Diana3noflx anomalies differ significantly from the anomalies in the Diana1 and Diana3 simulation in at least three ways: the Diana3noflx anomalies 1) are significantly weaker, 2) are smaller and less widespread and 3) appear much later in the simulation than the anomalies in either of the previously mentioned simulations. Clearly latent and sensible fluxes of heat from the ocean surface are important in the generation and maintenance of convection over the

tropical oceans, and this sensitivity experiment is the ultimate test of the impact of wind-induced surface fluxes on the tropical cyclogenesis process. However, these results suggest that, even when we turn off *all* latent and sensible fluxes from the ocean surface (which is certainly more extreme than just turning off the wind-dependent fluxes), the VHT pathway to tropical cyclogenesis is still active, though much subdued. That is, the pre-cyclogenesis phase of development in H04's two-stage tropical cyclogenesis process is likely not dependent on wind-dependent surface fluxes for the initial development of deep vortical hot towers. While fluxes from the surface would certainly enhance the convection and speed up the genesis process, they are clearly not required *a priori* for the generation of VHTs and the associated pre-cyclogenesis activity, at least for the case of Hurricane Diana as simulated in MM5.

3.6 Summary of Model Synoptic Data

We have presented evidence that our 1km MM5 simulation performed reasonably well in capturing the evolution of synoptic scale environmental conditions associated with the genesis of Hurricane Diana. While we noted some discrepancies with regard to storm track and intensity, the essence of Diana's genesis appears well represented. It is also clear that our synoptic scale model evolution is consistent with previous modeling studies of Diana (e.g. DB01, DB02, H04, PD02) and previous investigations of VHT dynamics in the context of tropical cyclogenesis (e.g. H04 and M06). This is not altogether unexpected as most of the above mentioned modeling studies also used MM5 and showed that MM5 was effective in simulating Diana's genesis and evolution. In this study, however, we have employed a slightly different version of the model with

horizontal grid spacing finer than previous genesis studies. We have thus shown the robustness of MM5 to simulations of hurricane genesis and, in particular, the genesis of Hurricane Diana. We have verified previous conclusions by H04 and PD02 that 3km horizontal grid spacing in a full physics model (such as MM5) is sufficient to accurately simulate the evolution of synoptic conditions related to tropical cyclogenesis. Lastly, we have shown evidence suggesting that the VHT pathway to tropical cyclogenesis is a pre-WISHE process in the case of Hurricane Diana. While VHT activity is dependent upon surface fluxes for tropical cyclogenesis to be complete, latent and sensible fluxes from the ocean do not appear to be required *a priori* to initiate VHT activity. This suggests that VHT activity in general may not sensitively depend on surface fluxes, though more study is necessary to confirm this in other storms.

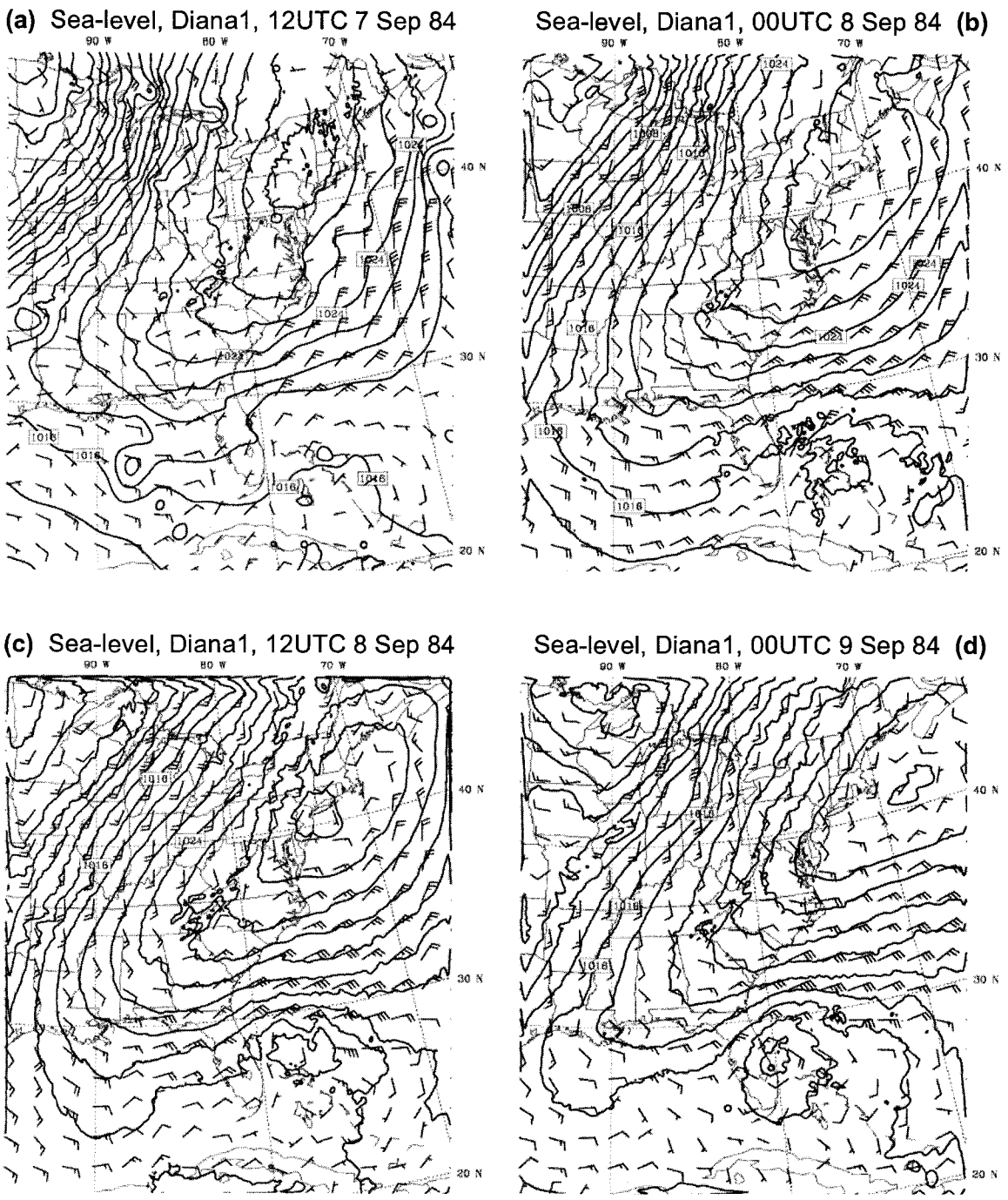

Figure 3.1. Evolution of sea-level pressure (SLP) and surface wind fields on the 9km grid of the Diana1 simulation. Fields are plotted at (a) 12UTC 7 Sep 84 (t = 0h), (b) 00UTC 8 Sep 84 (t = 12h), (c) 12UTC 8 Sep 84 (t = 24h) and (d) 00UTC 9 Sep 84 (t = 36h). Sea-level pressure contours are every 2hPa and each full barb represents a wind speed of 5ms^{-1}.

(a) 00UTC 7 Sep 84

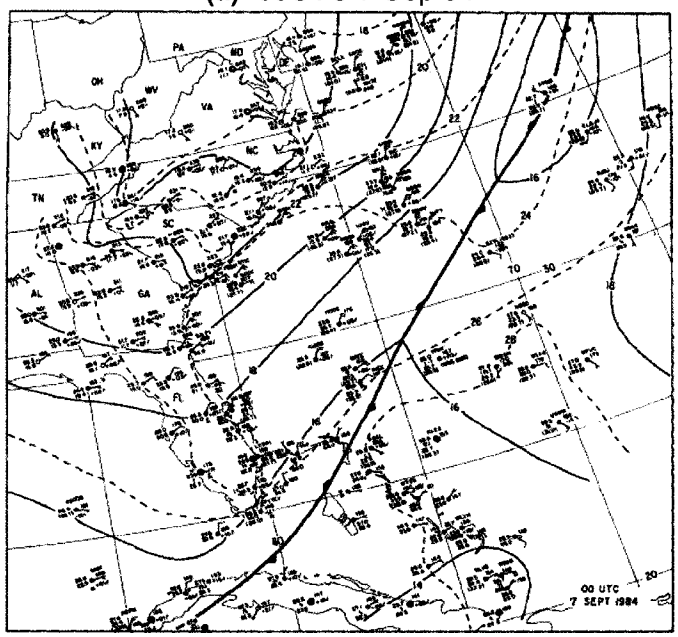

(b) 00UTC 8 Sep 84

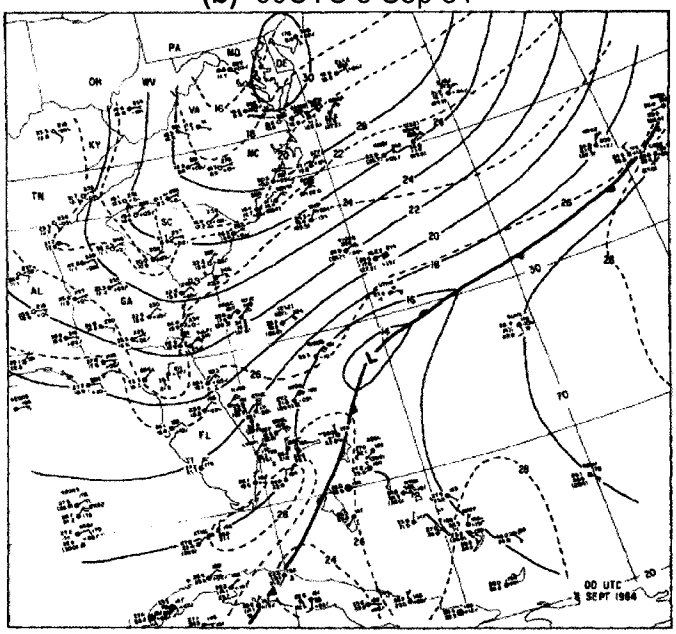

Figure 3.2. Surface section maps showing observed mean sea-level pressure, surface temperature, dewpoint and winds at (a) 00UTC 7 Sep 84 and (b) 00UTC 8 Sep 84. Isobars (solid lines) are every 2hPa, and temperatures (dashed lines) are every 2°C. (Taken from Figure 8 of Bosart and Bartlo, 1991)

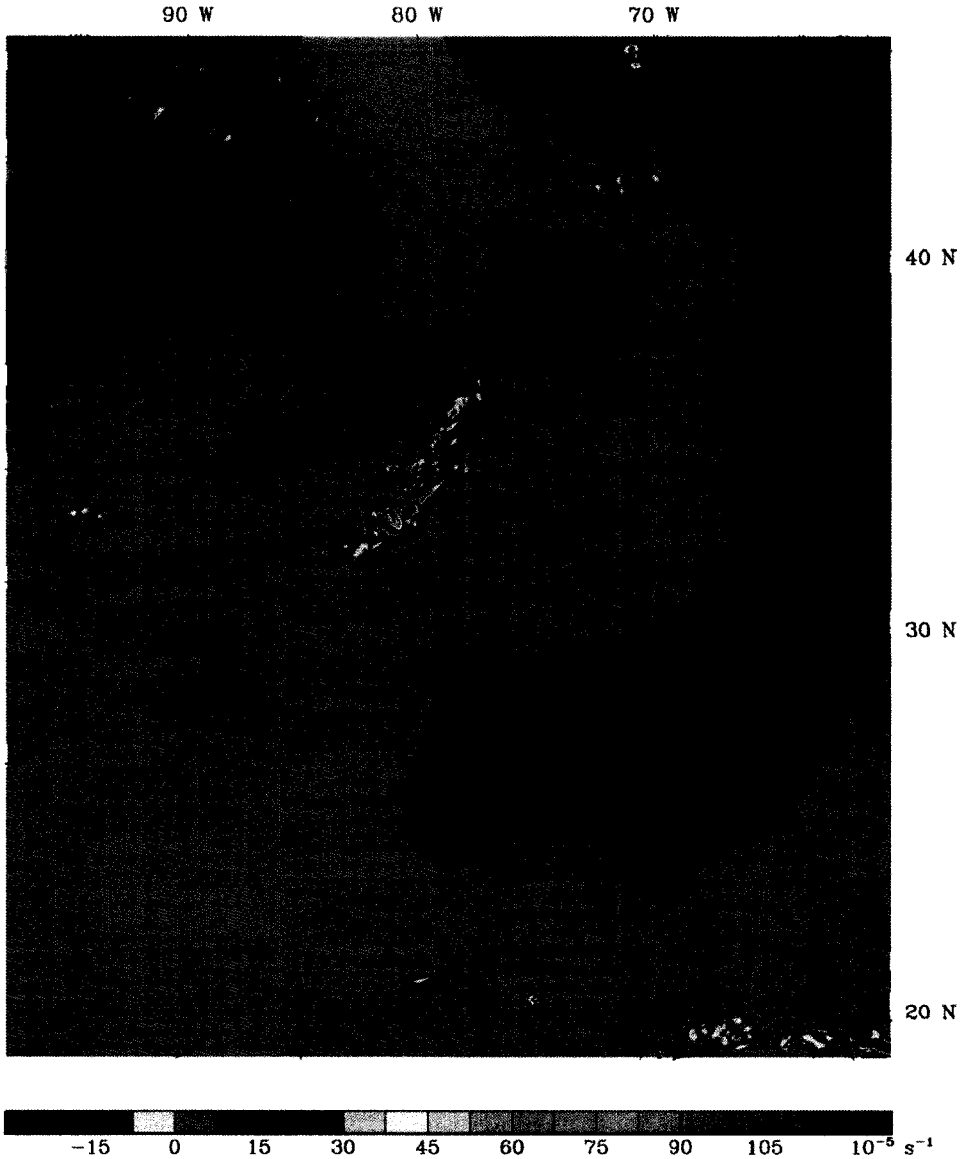

Figure 3.3. Initial absolute vertical vorticity on the 925hPa pressure surface for the 9km grid.

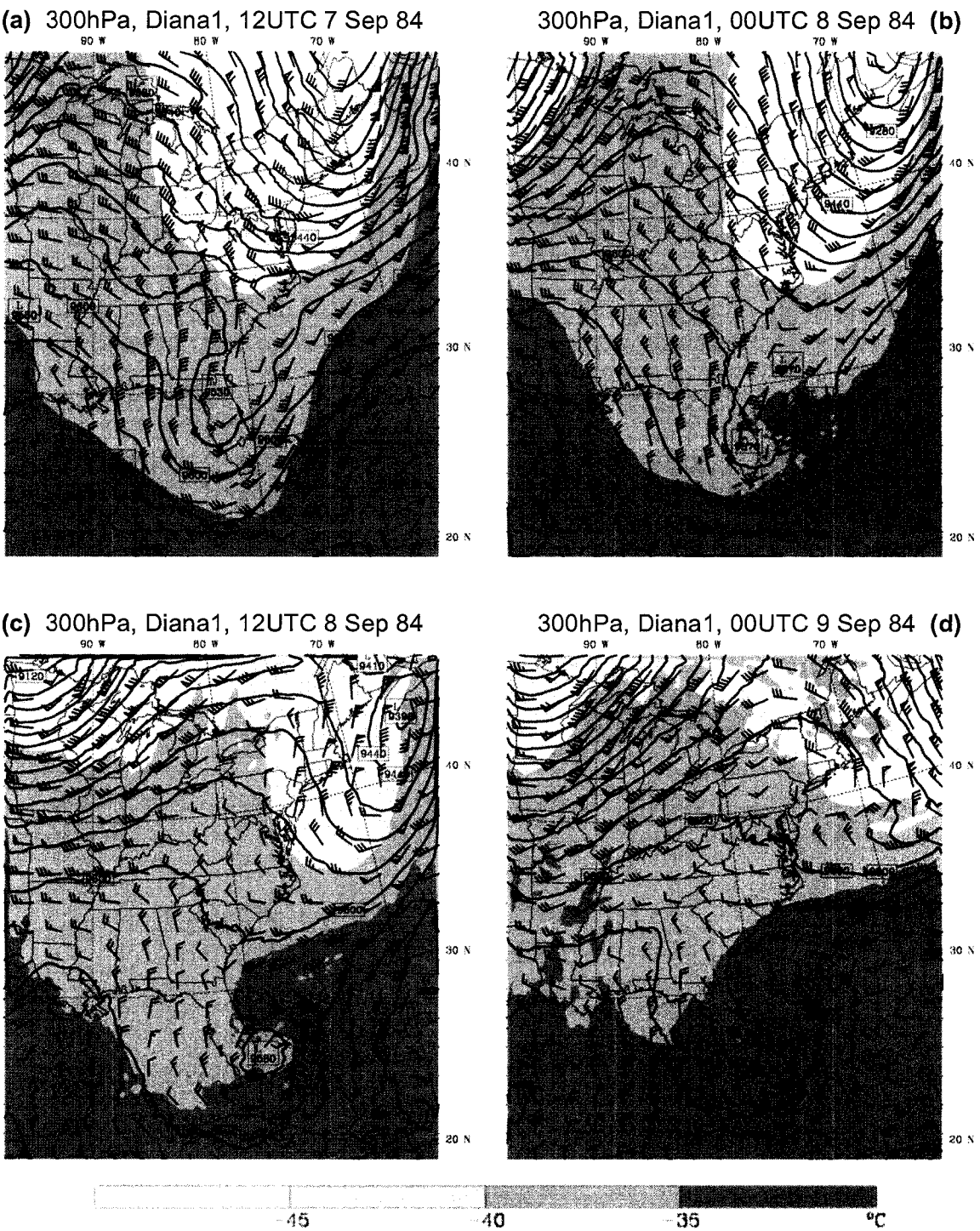

Figure 3.4. Evolution of 300hPa geo-potential height, wind and temperature fields on the 9km grid for the Diana1 simulation. Fields are plotted at (a) 12UTC 7 Sep 84 (t = 0h), (b) 00UTC 8 Sep 84 (t = 12h), (c) 12UTC 8 Sep 84 (t = 24h) and (d) 00UTC 9 Sep 84 (t = 36h). Geopotential height contours are every 40m, temperature contours are every 5 °C and each full barb represents a wind speed of 5ms^{-1}.

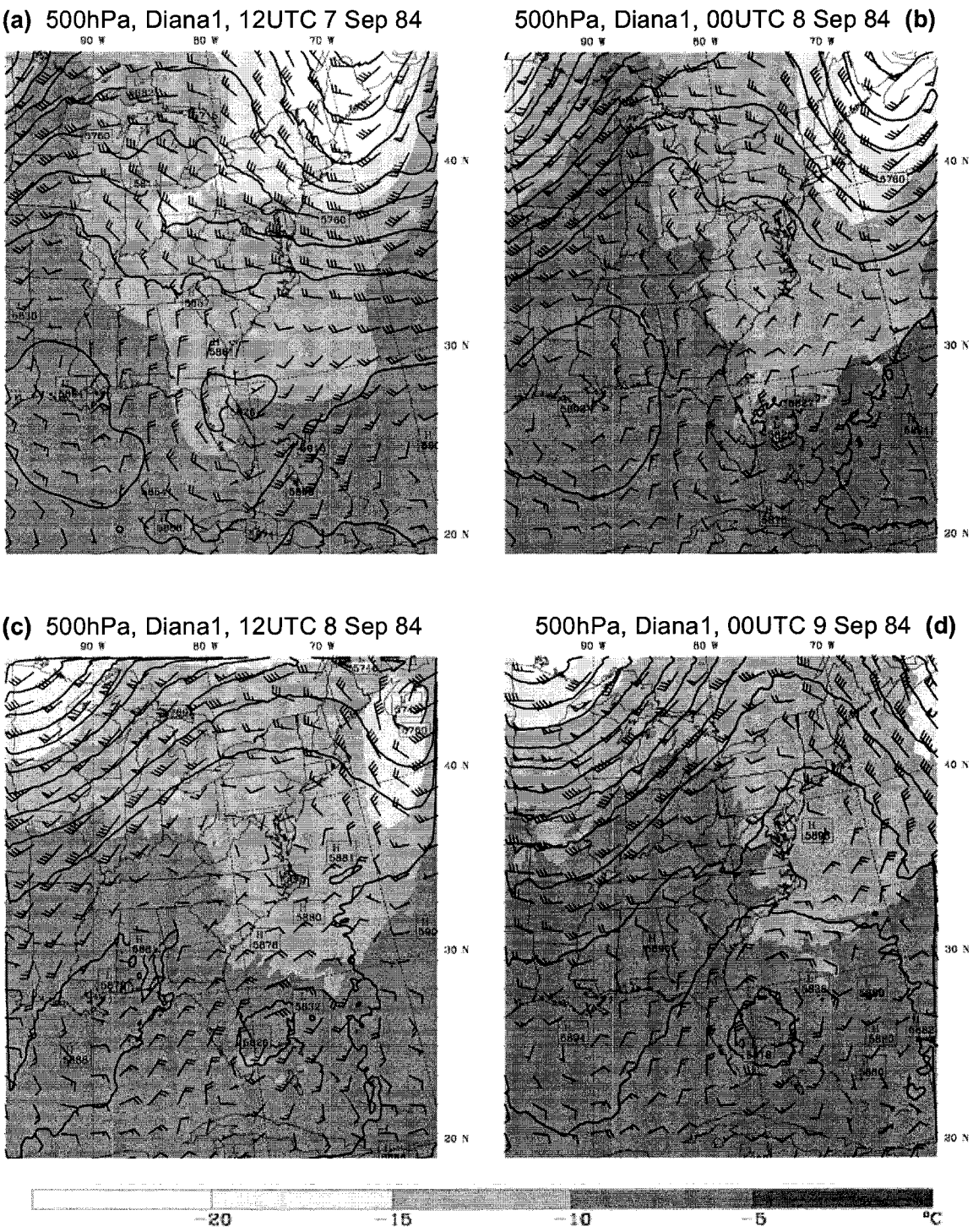

Figure 3.5. Evolution of 500hPa geo-potential height, wind and temperature fields on the 9km grid for the Diana1 simulation. Fields are plotted at (a) 12UTC 7 Sep 84 (t = 0h), (b) 00UTC 8 Sep 84 (t = 12h), (c) 12UTC 8 Sep 84 (t = 24h) and (d) 00UTC 9 Sep 84 (t = 36h). Geopotential height contours are every 40m, temperature contours are every 5 °C and each full barb represents a wind speed of 5ms^{-1}.

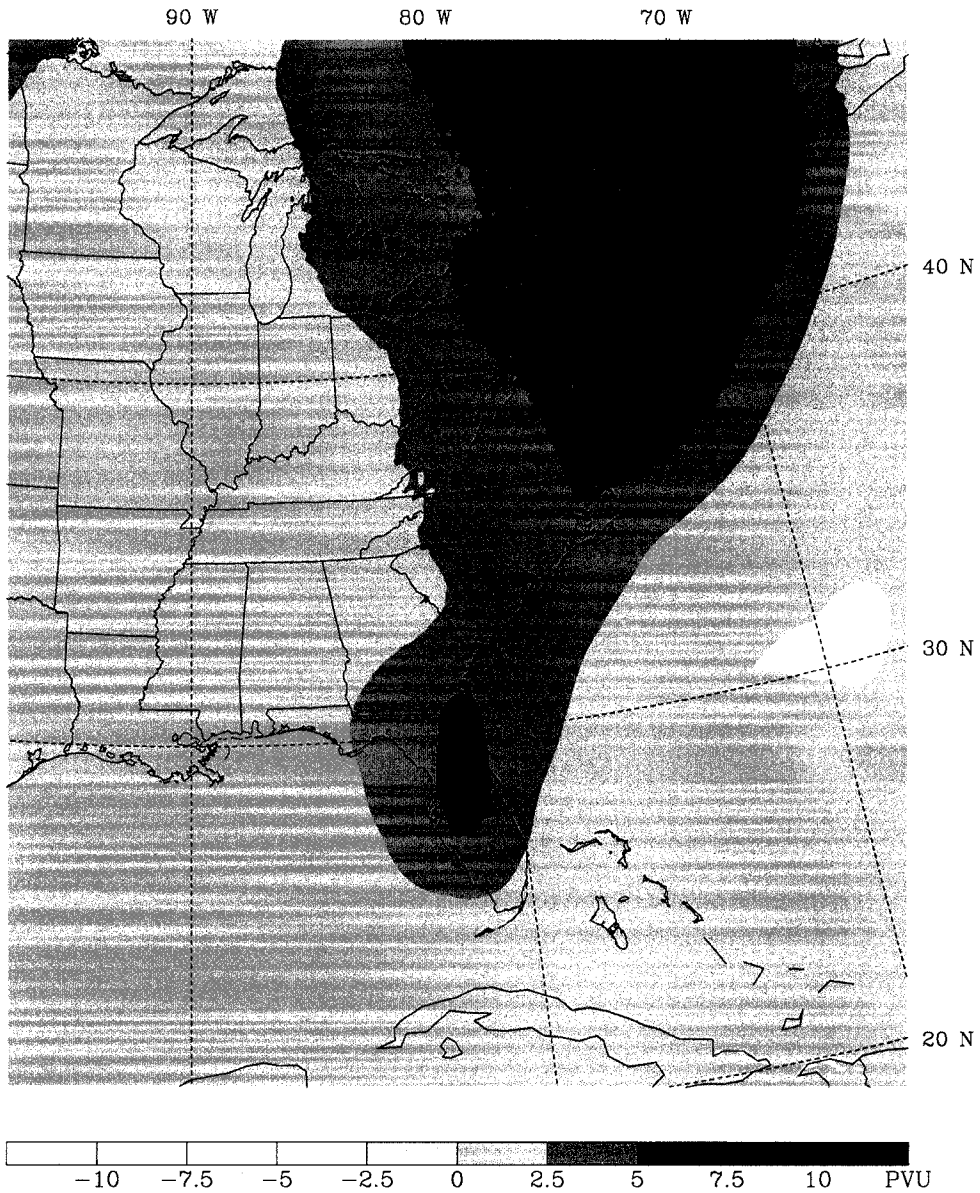

Figure 3.6. Initial potential vorticity (340K surface) in PVU on the 9km grid.

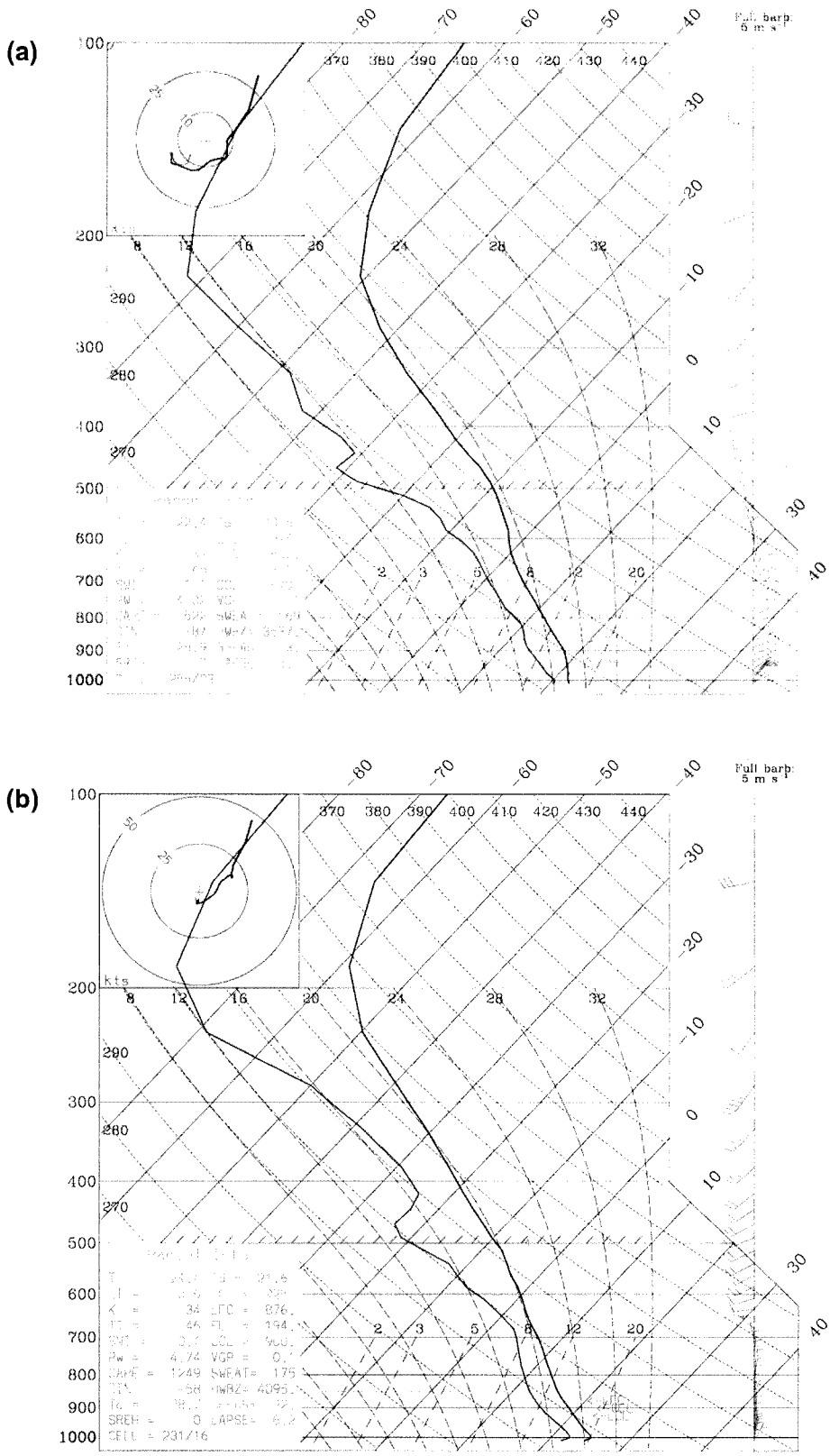

Figure 3.7. Skew-T/Log P diagram at model initialization for (a) Cape Kennedy, Florida, and (b) West End, Grand Bahamas (computed from data on the 9km grid).

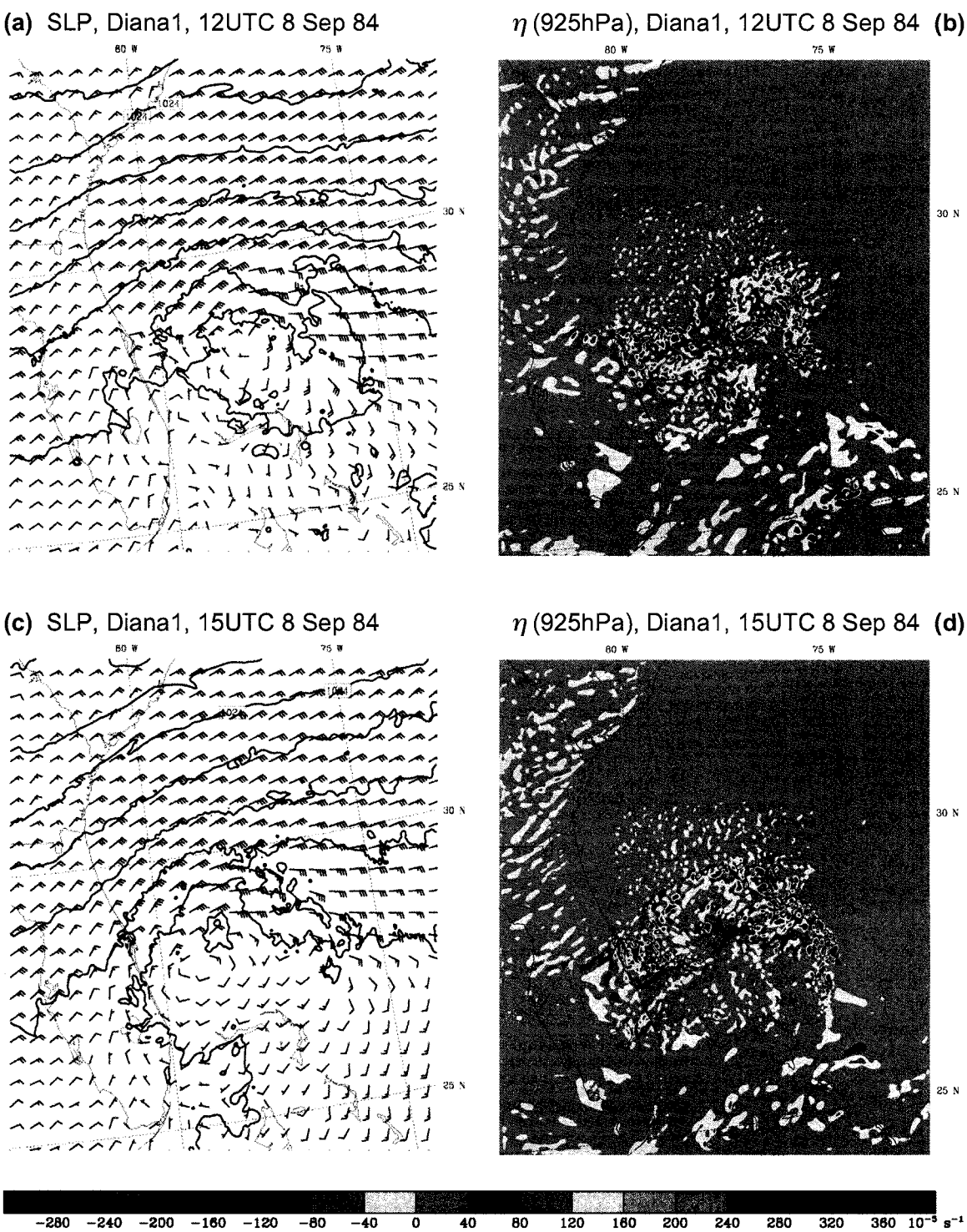

Figure 3.8. Sea-level pressure and surface winds (left column) and low-level (p =925hPa) absolute vorticity field (right column) near the timing of the genesis of Hurricane Diana as indicated in the observational analysis of Bosart and Bartlo (1991). Plots (a) and (b) are valid at 12UTC 8 Sep 84 (t = 24h). Plots (b) and (c) are valid at 15UTC 8 Sep 84 (t = 27h).

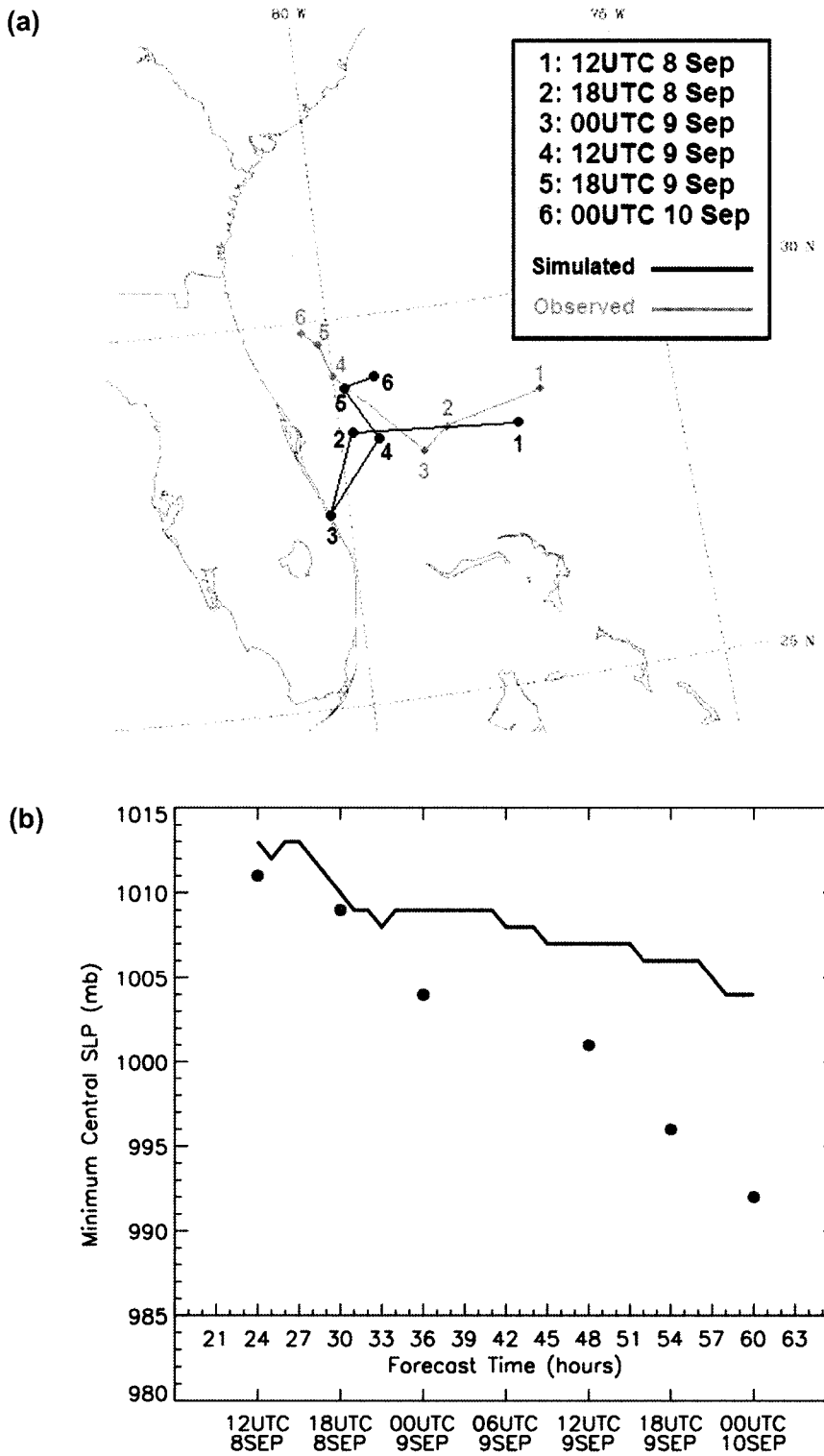

Figure 3.9. (a) Track and (b) intensity of simulated storm (black) and observed storm (gray). Times are listed in table in upper right portion of (a). Observed storm track and intensity adapted from Figure 2 of Powers and Davis (2002).

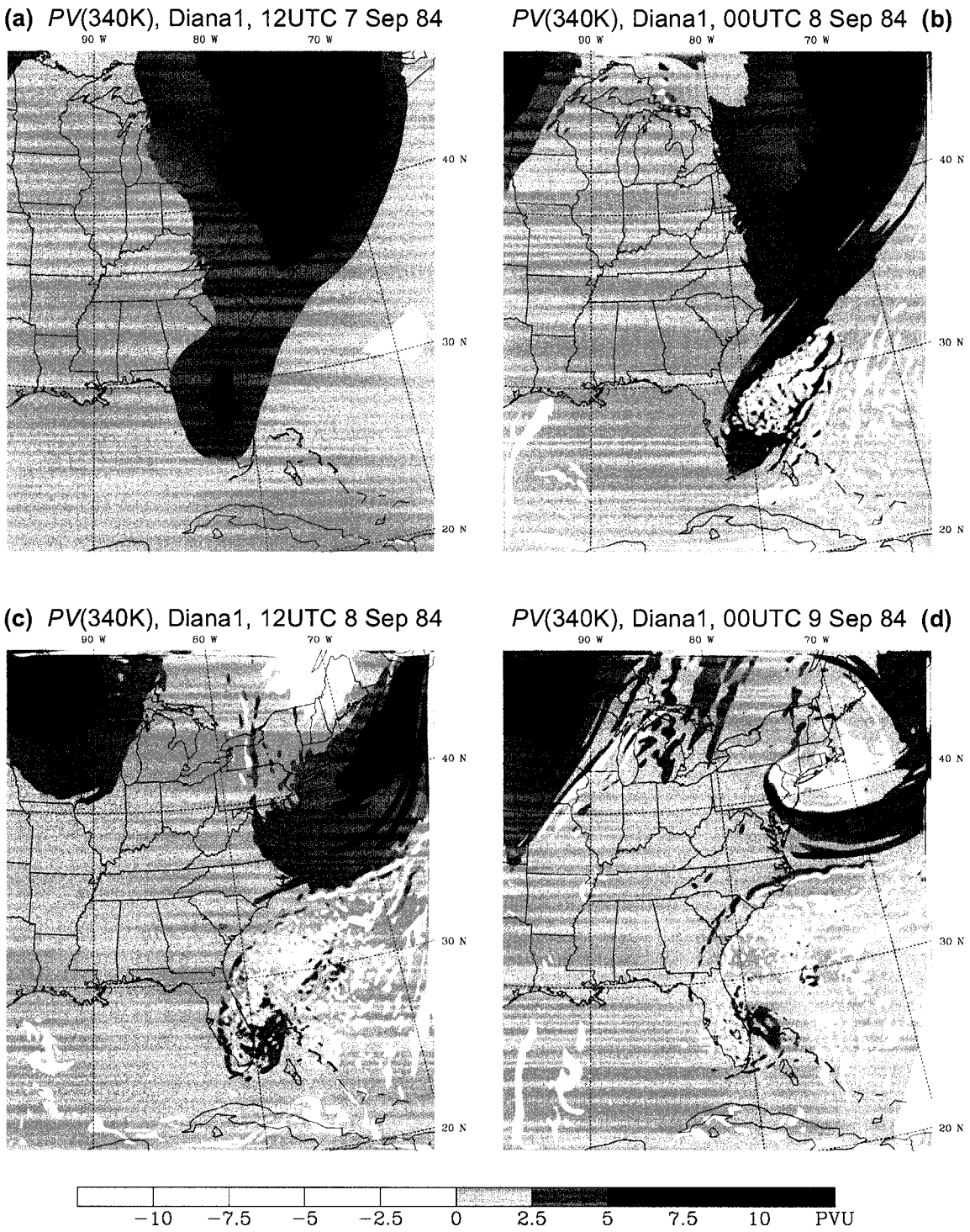

Figure 3.10. Evolution of potential vorticity (340K surface) in PVU on the 9km grid for the Diana1 simulation. Fields are plotted at (a) 12UTC 7 Sep 84 (t = 0h), (b) 00UTC 8 Sep 84 (t = 12h), (c) 12UTC 8 Sep 84 (t = 24h) and (d) 00UTC 9 Sep 84 (t = 36h). Contours are the same as in Figure 3.6.

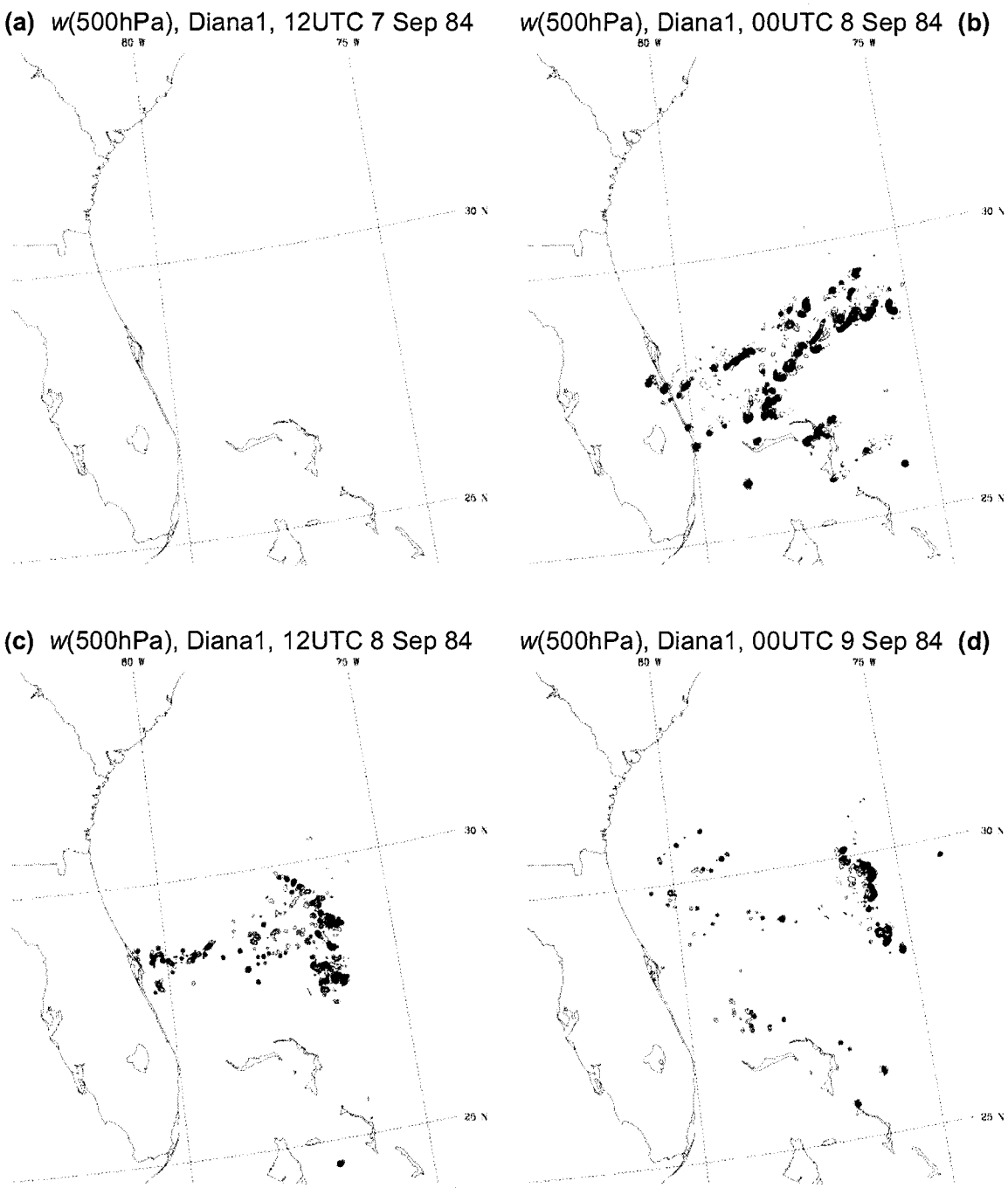

Figure 3.11. Evolution of the vertical velocity field at p = 500hPa on the 3km grid for the Diana1 simulation. Fields are plotted at (a) 12UTC 7 Sep 84 (t = 0h), (b) 00UTC 8 Sep 84 (t = 12h), (c) 12UTC 8 Sep 84 (t = 24h) and (d) 00UTC 9 Sep 84 (t = 36h). Contours are every 1 ms^{-1}. Negative contours are dashed. Zero contour is omitted.

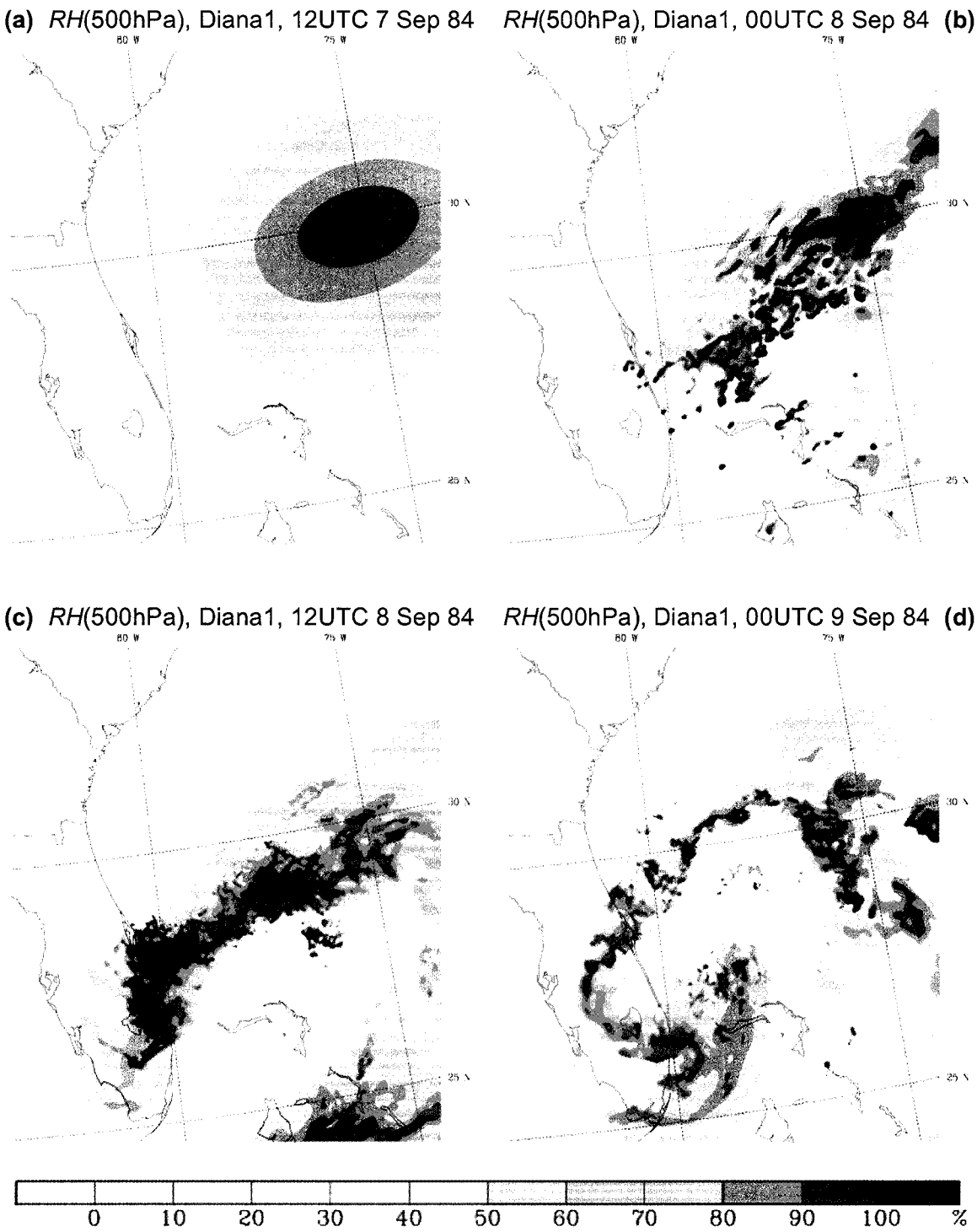

Figure 3.12. Evolution of 500hPa relative humidity field on the 3km of the Diana1 simulation. Fields are plotted at (a) 12UTC 7 Sep 84 (t = 0h), (b) 00UTC 8 Sep 84 (t = 12h), (c) 12UTC 8 Sep 84 (t = 24h) and (d) 00UTC 9 Sep 84 (t = 36h). Shaded contours are every 10% beginning at 50%.

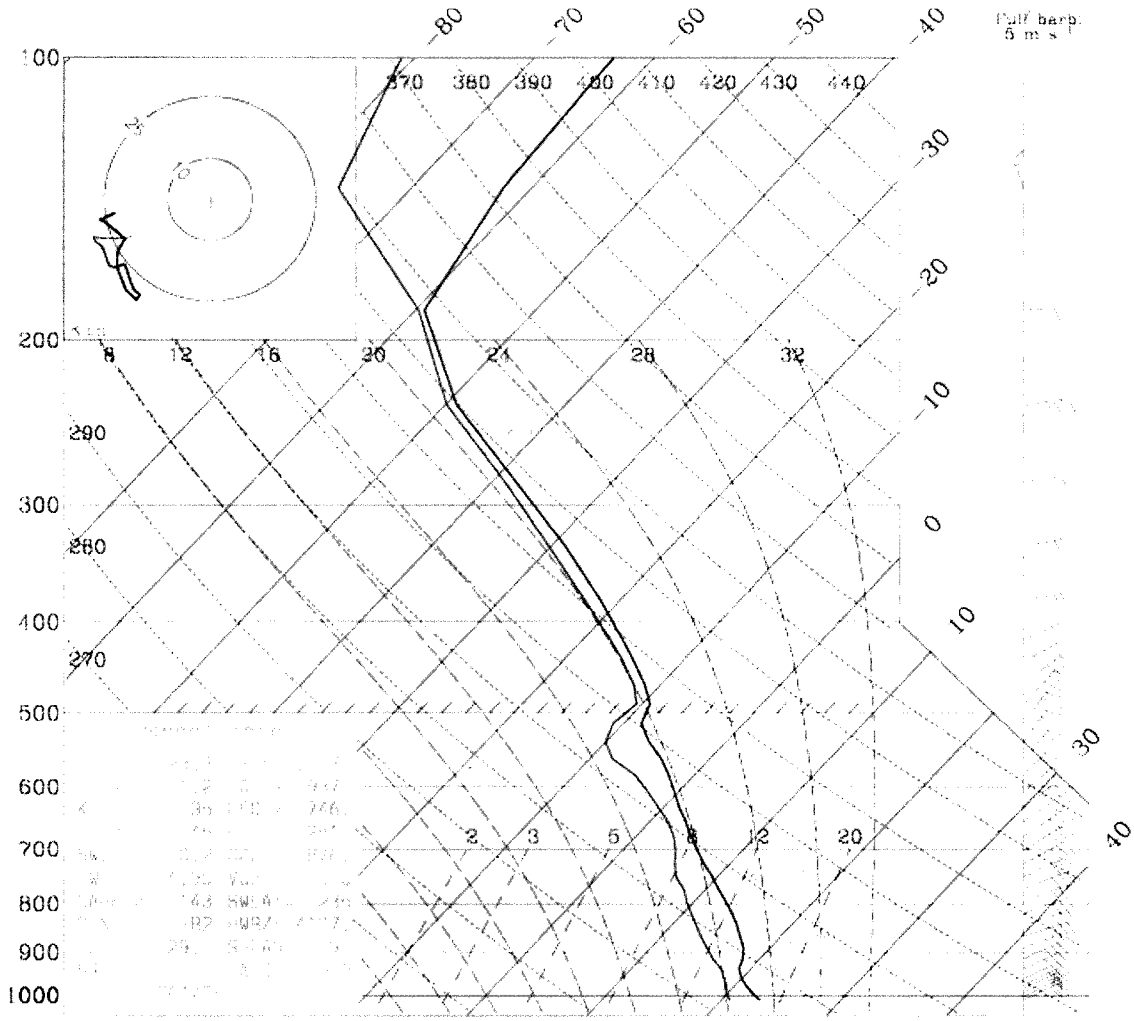

Figure 3.13. Skew-T/Log P diagram for Cape Kennedy Florida at t = 24h into the simulation (12UTC 8 Sep 84). Each full wind barb represents a wind speed of 5ms^{-1} (computed from data on the 9km grid).

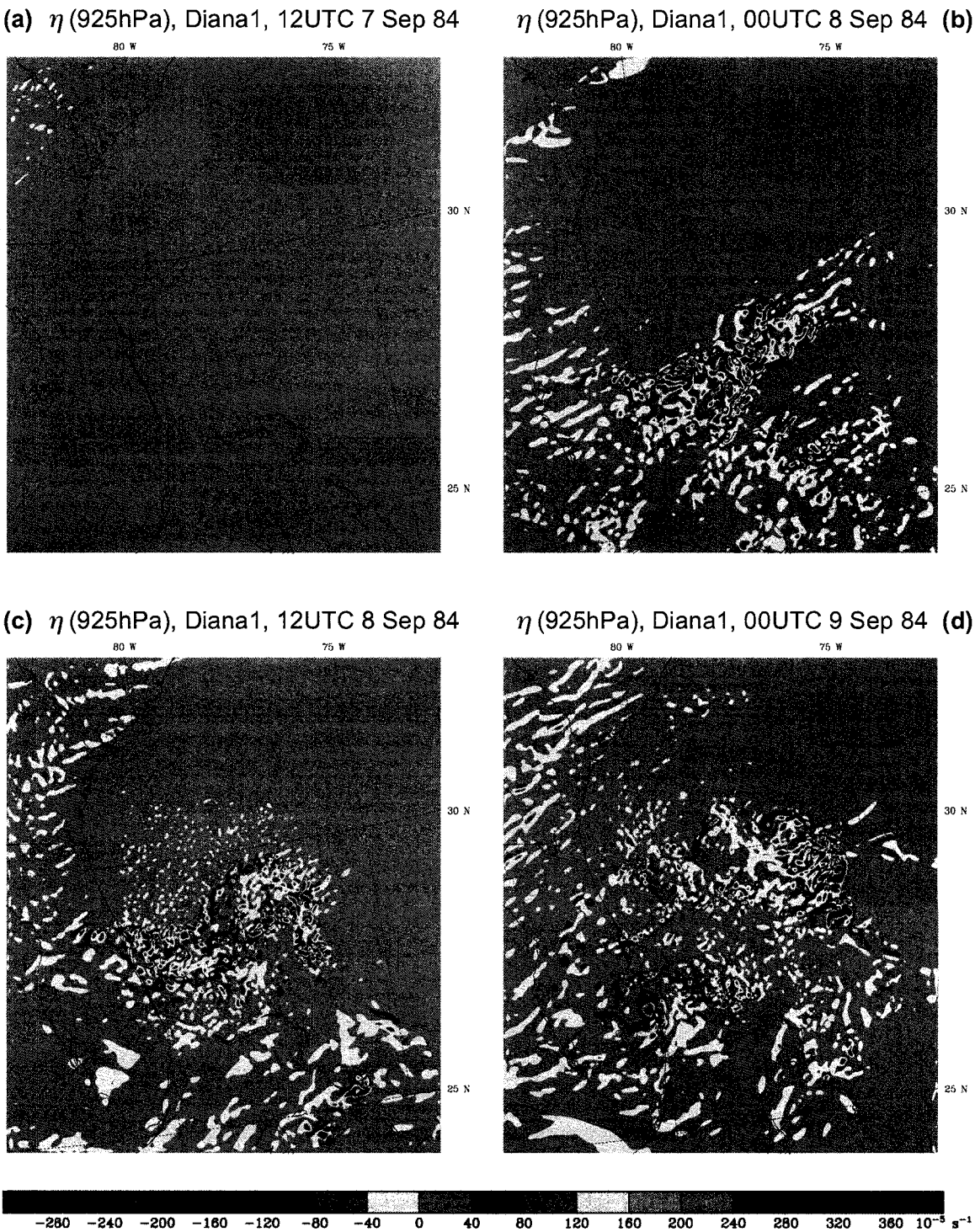

Figure 3.14. Evolution of absolute vorticity at 925hPa on the 3km grid during the pre-cyclogenesis phase. Fields are plotted at (a) 12UTC 7 Sep 84 (t = 0h), (b) 00UTC 8 Sep 84 (t = 12h), (c) 12UTC 8 Sep 84 (t = 24h) and (d) 00UTC 9 Sep 84 (t = 36h). Note that the shading is significantly different than the shading in Figure 3.3.

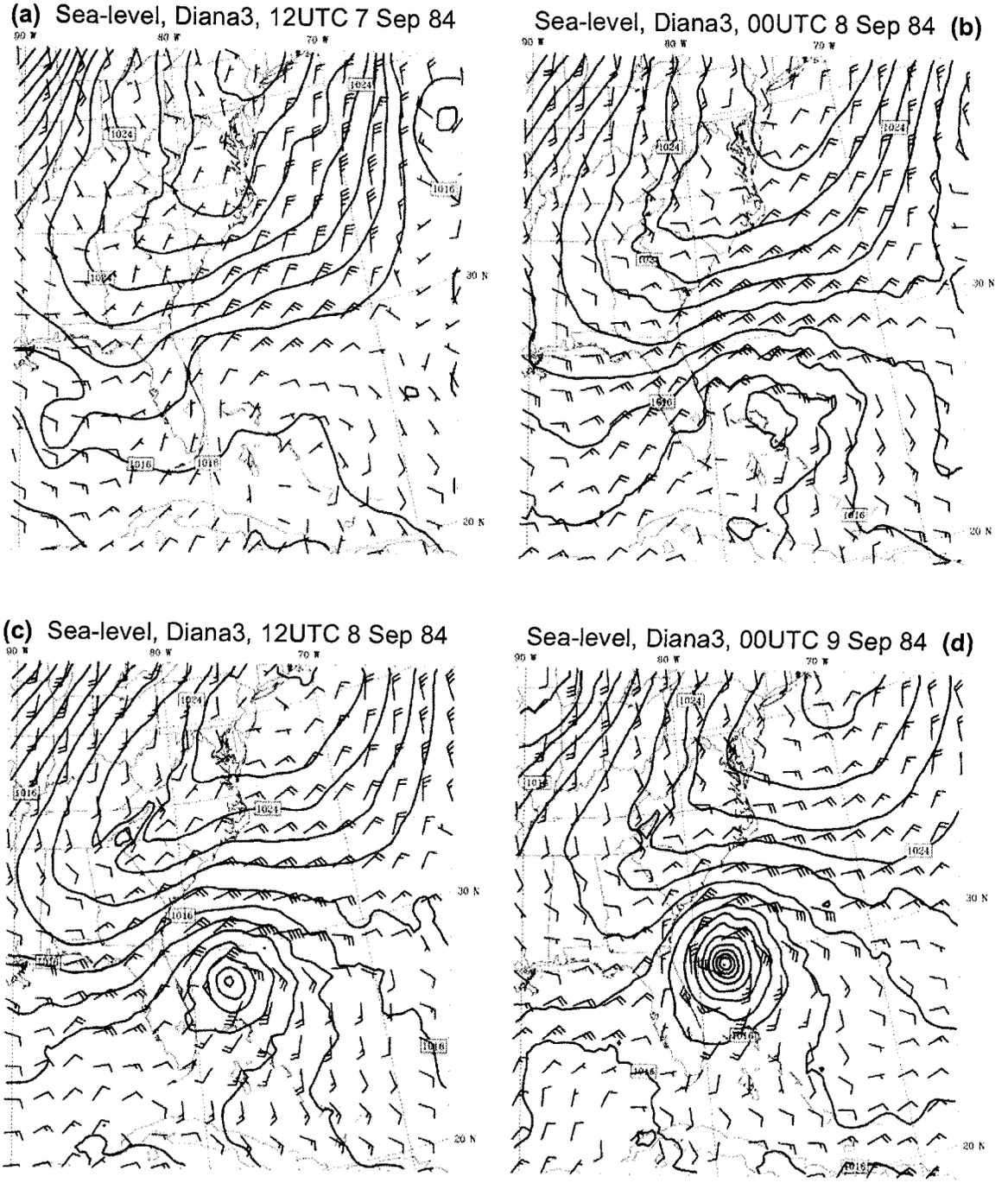

Figure 3.15. Evolution of the sea-level pressure field and surface winds for the Diana3 simulation on the 27 km grid. Fields are plotted at (a) 12UTC 7 Sep 84 (t = 0h), (b) 00UTC 8 Sep 84 (t = 12h), (c) 12UTC 8 Sep 84 (t = 24h) and (d) 00UTC 9 Sep 84 (t = 36h). Contours and wind barbs are the same as in Figure 3.1.

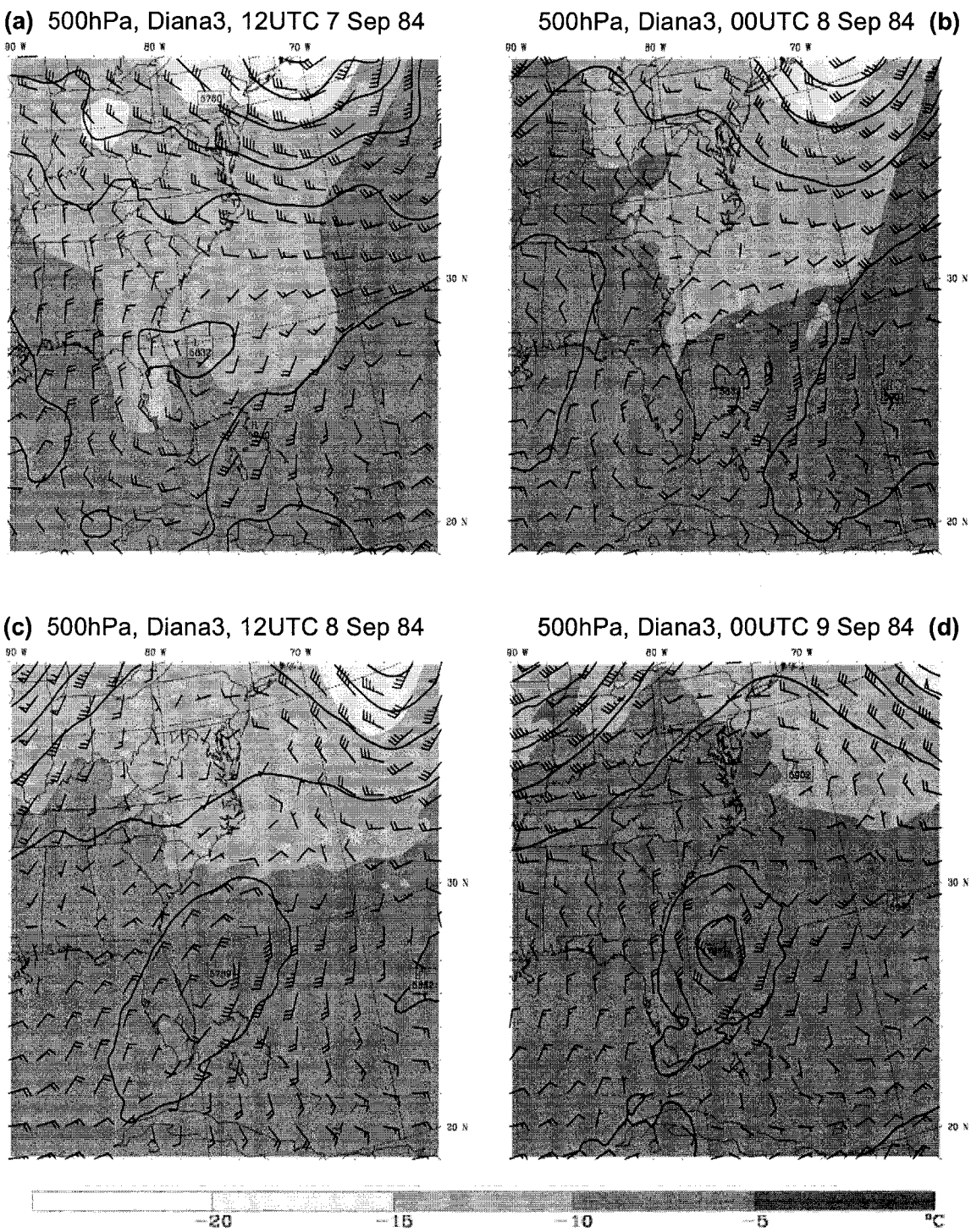

Figure 3.16. Evolution of 500hPa geo-potential height, wind and temperature fields for the Diana3 simulation on the 27 km grid. Fields are plotted at (a) 12UTC 7 Sep 84 (t = 0h), (b) 00UTC 8 Sep 84 (t = 12h), (c) 12UTC 8 Sep 84 (t = 24h) and (d) 00UTC 9 Sep 84 (t = 36h). Contours and wind barbs are the same as in Figure 3.5.

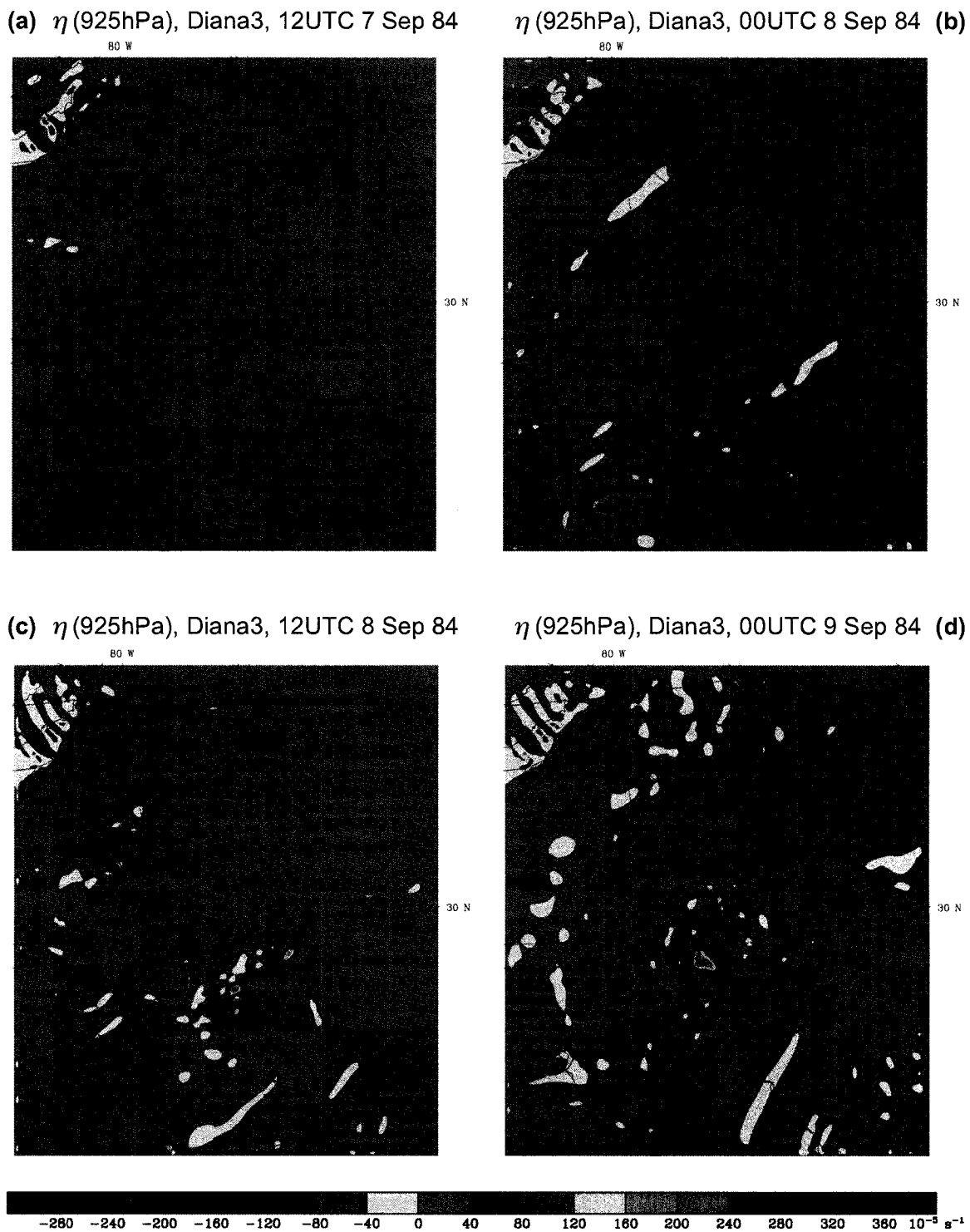

Figure 3.17. Evolution of absolute vorticity at 925hPa for the Diana3 simulation on the 9 km grid. Fields are plotted at (a) 12UTC 7 Sep 84 (t = 0h), (b) 00UTC 8 Sep 84 (t = 12h), (c) 12UTC 8 Sep 84 (t = 24h) and (d) 00UTC 9 Sep 84 (t = 36h). Contours are the same as in Figure 3.14.

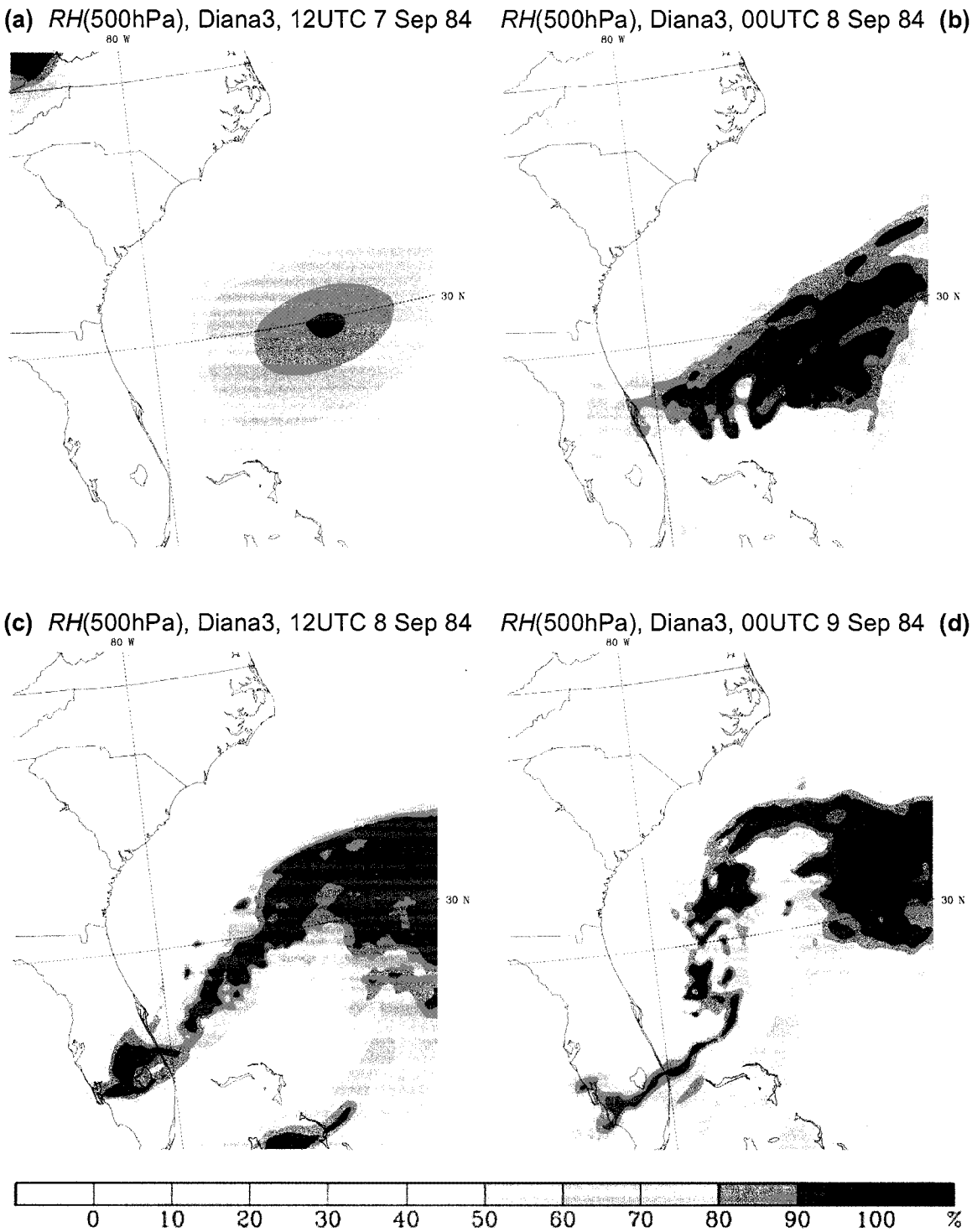

Figure 3.18. Evolution of 500hPa relative humidity field for the Diana3 simulation on the 9 km grid. Fields are plotted at (a) 12UTC 7 Sep 84 (t = 0h), (b) 00UTC 8 Sep 84 (t = 12h), (c) 12UTC 8 Sep 84 (t = 24h) and (d) 00UTC 9 Sep 84 (t = 36h). Contours are the same as in Figure 3.12.

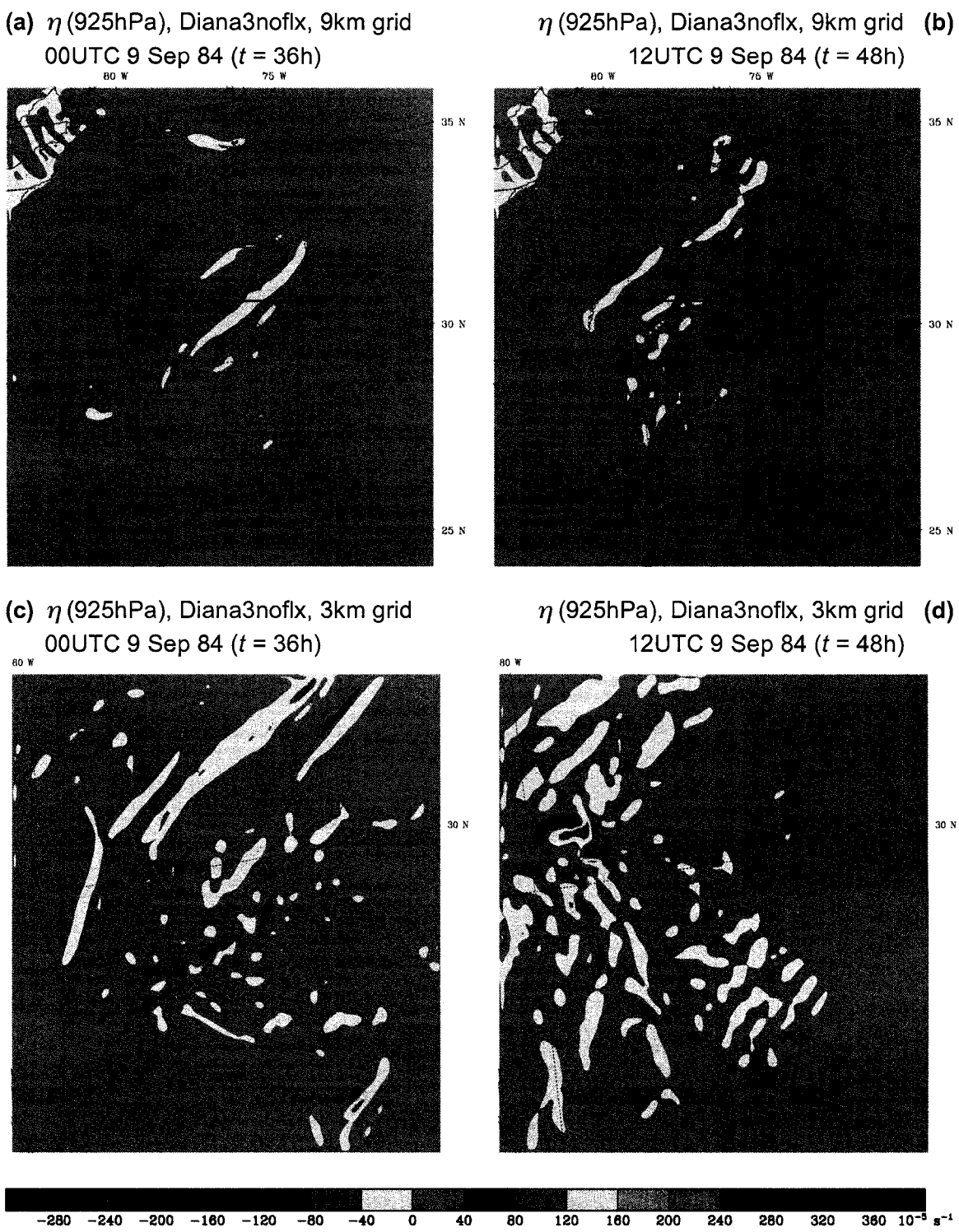

Figure 3.19. Evolution of absolute vorticity at 925hPa for the Diana3noflx simulation on the 9 km grid (upper row) and 3km grid (lower row). Fields are plotted at 00UTC 9 Sep 84 (t = 36h, left column) and 12UTC 9 Sep 84 (t = 48h, right column). The boxes in the upper plots show the relative position of the 3km grid on the 9km grid. Contours are the same as in Figure 3.17.

Chapter 4

EVOLUTION OF MESOSCALE FEATURES

4.1 Introduction

We now turn our attention to the mesoscale aspects of the simulation of Hurricane Diana. For each phase of Diana's development we compare key mesoscale aspects of our Diana1 experiment versus the H04 simulation (and our Diana3 experiment, when necessary). The analysis in this chapter focuses on two main areas: 1) the mesoscale nature and evolution of the absolute vorticity and moisture fields in each simulation with emphasis on impacts due to VHTs and 2) the aggregate impact of VHT activity on the system scale environment. Based on our findings, we determine whether or not (or to what degree) the previous conclusions of H04 hold at horizontal grid spacing finer than 3km. This analysis also gives us the opportunity to re-examine the conclusions of M06 specifically with regard to the VHT pathway to tropical cyclogenesis and how that mechanism changes (if at all) in the framework of a full-physics simulation initialized with environmental conditions rather than idealized conditions.

For the analysis that follows, we examine output from the 3km grid of the H04 simulation and compare this data against the 1km grid of our Diana1 simulation since these grids are the finest resolution grids in each case (see Figure 2.1 and Figure 2.2).

Also, each domain covers approximately the same geographic area east of the Florida peninsula allowing for a more meaningful comparison of the data. When helpful to further quantify the resolution dependency of the genesis process or when specific data or analysis techniques do not exist from the H04 study we will introduce data from the 3km grid of our Diana3 simulation. As stated in Chapter 2, the H04 numerical experiment and our Diana3 simulation are not the same. Our Diana3 experiment was an attempt to recreate the H04 experiment with a different version of MM5 that required a modification to the initial conditions to generate Hurricane Diana (see Section 2.3.2). As a result, when we present the output of the Diana3 experiment, the intent is to clarify the differences between genesis simulations that may be attributable to changes in resolution rather than a strict comparison of previous 3km work to our 1km simulation.

In a slight deviation from the discussion order in Chapter 3, we begin this chapter with the results of the H04 and Diana3 simulations and close with discussion of the Diana1 simulation. The reason for this is to establish a baseline of comparison with previous modeling studies first. Then, we present our Diana1 high resolution output and compare our *new* results against this baseline.

4.2 H04 Study

4.2.1 Summary of H04 Results

We begin by summarizing and analyzing the results of the 3km H04 simulation. According to H04, the first stage of the evolutionary process resulting in the genesis of Hurricane Diana was a pre-conditioning phase characterized by an outbreak of

widespread convection over the eventual genesis area. The convective cores were generally oriented along a low-level convergence zone associated with an early season cold front that moved through the southeastern United States. This convergence/frontal zone provided a source of low-level vorticity resulting in significant values of cyclonic vertical vorticity over the entire genesis region (see Chapter 3). A conditionally unstable atmosphere coupled with a significant upper-level potential vorticity anomaly and associated upper-level cold dome supplied additional forcing over the region and further helped to initiate the convective outbreak. The upper-level features were also connected to a developing mid-level vortex that fractured from its parent low far to the north. The mid-level vortex supplied a source of horizontal and vertical vorticity over the genesis region which was shown by M06 to have a fundamental role in the tropical cyclogenesis process through tilting and stretching of this vorticity by deep convection. As the convection matured and became widespread, the individual cores developed similar characteristics. They were typically associated with intense diabatically generated low-level positive vorticity anomalies that arose from the tilting of ambient horizontal vorticity into the vertical (due to the mid-level vortex, see Chapter 3) and the subsequent stretching of that vorticity and the background cyclonic vorticity by intense updraft velocities (H04, M06). Together, the convective updraft cores and their associated cyclonic vorticity anomalies comprised the individual VHTs that previous authors, namely H04 and M06, have directly connected to the tropical cyclogenesis process. These authors suggested that VHTs generated during the pre-conditioning phase of development permeate the low-level vorticity field and act in a non-cooperative manner as they feed off the CAPE in the atmosphere. That is, they pulse the genesis region and

compete with each other for the available CAPE rather than cooperate to form the system scale vortex (H04, M06).

The effect of the VHTs on the local environment during a tropical cyclogenesis episode has two noteworthy effects: (1) as each convective updraft erupts and then dies out, the low-level vorticity anomaly associated with the updraft core persists leaving a signature of the vortex in the field (H04, M06; see Figure 4.1) and (2) the presence of these VHT cores leads to a secondary circulation that provides a net flux of angular momentum inward to the genesis area resulting in an increase in the ambient values of vorticity over a much larger area (H04, M06). The end result is that the complex of VHTs acts collectively to increase the overall values of low-level cyclonic vorticity in the genesis region, producing an environment that is "primed" for cyclogenesis (H04, M06).

4.2.2 H04 Vorticity Field

Based on their 3km results, H04 divided the cyclogenesis of Diana into two phases: a preconditioning phase in which the VHTs form and lead to secondary circulations that flux angular momentum into the genesis region, and a merger phase in which a subset of the VHT axisymmetrize to form the cyclone. According to H04, the pre-conditioning phase of the genesis of Hurricane Diana lasted from roughly t =21h to t = 27h (09UTC 8 Sep 84 to 15UTC 8 Sep 84) with the merger phase occurring from approximately t = 27h to t = 36h (15UTC 8 Sep to 00UTC 9 Sep 84). Figure 4.2 shows plots of low-level absolute vorticity values from the H04 simulation at t = 23h, t = 24h and t = 25h. These plots are representative of the character of the absolute vorticity field during Diana's pre-conditioning phase and give us an indication of the VHT activity occurring at this time in

the simulation. In Figure 4.2 we see multiple vertical vorticity maxima (~5) embedded within a very broad area of elevated vorticity values likely associated with the frontal boundary/convergence zone present in the synoptic and mesoscale data (Bosart and Bartlo 1991, H04). Note the limited number of high vorticity cores ($\eta \geq 3.0\times10^{-3}\,s^{-1}$, the red and purple shaded areas) and the limited merger events that likely occur over the 3 hour period encompassed by the plots. Also noteworthy is the relatively large aerial distribution of positive vorticity values over the whole of the domain. By visual inspection, the area of positive vorticity seems larger and more intense than the negative, and there is a lack of large negative vorticity cores in the domain, particularly at lower levels (the left column in Figure 4.2). By and large, the magnitude of the strongest anticyclonic anomalies is or the order of $\eta \approx -1.0\times10^{-3}\,s^{-1}$, less than one-third the magnitude of the strongest cyclonic anomalies ($\eta \approx 3.5\times10^{-3}\,s^{-1}$). The imbalance in the strength of the cyclonic and anticyclonic vorticity anomalies is particularly evident at low-levels, though the vorticity field at mid-levels (the right column in Figure 4.2) indicates a general weakening of the cyclonic anomalies and strengthening of the anticyclonic anomalies with height.

During the merger phase of development, this bias toward cyclonic vorticity anomalies at low-levels overshadowing the anticyclonic anomalies continues and becomes more obvious. Figure 4.3 shows plots of low-level absolute vorticity from the H04 simulation at t = 26h, t = 27h and t = 33h. These plots are representative of the character of the absolute vorticity field during the merger phase of the H04 simulation. It is important to note that the plots in the left column of Figure 4.3 are snapshots of the vorticity field 30 minutes earlier than the plots in the right column allowing the authors to

focus on individual merger events (highlighted by the white circles). A comparison of this plot to the corresponding plot from the pre-conditioning phase (Figure 4.2) reveals a few noteworthy details. Overall, the basic structure of the vorticity field has essentially remained the same. Generally positive vorticity is visible over the whole of the domain with an isolated, nearly contiguous area of elevated cyclonic vorticity in the genesis region punctuated by strong cyclonic and anticyclonic vorticity anomalies. However, we do see evolutionary differences between Figure 4.2 and Figure 4.3 that can be attributed to the tropical cyclogenesis process and, in-particular, to the VHT activity. The number of strong cyclonic vorticity cores ($\eta \geq 3.0\times10^{-3}\,s^{-1}$) now numbers approximately 2 to 3 whereas the number of cores visible in Figure 4.2 was approximately 5 (granted this is somewhat subjective and depends upon the time period analyzed). If we examine the intensity of the cyclonic anomalies in Figure 4.2 and Figure 4.3 we find that the strength of the cyclonic cores in the merger phase of development are comparable to the strength of the cores in the pre-conditioning phase with maximum values near $\eta = 3.5\times10^{-3}\,s^{-1}$. Moreover, if one closely compares Figure 4.2 and Figure 4.3, a change in the character of the vorticity field becomes evident. During the vortex merger phase (Figure 4.3), the areas of cyclonic vorticity become more concentrated in and around the strongest positive anomalies. However, during pre-conditioning the areas of cyclonic vorticity are broader and more evenly distributed over the genesis region with no such "concentration" of vorticity evident.

There is also a noticeable difference in the distribution of the negative vorticity field. While a similar number of anticyclonic cores are present during both phases of Diana's development in the H04 simulation (see Figure 4.2 and Figure 4.3), the cores that are

present during the merger phase are considerably weaker and the aerial coverage of the total negative vorticity field is significantly less than during pre-conditioning. Coupled with this is the additional observation that the strong anticyclonic vorticity anomalies in the merger phase (Figure 4.3) do not punctuate the central broad region of elevated vorticity as they do during pre-conditioning phase (Figure 4.2). It is as if, in the genesis process, the anticyclonic anomalies have been eradicated and the cyclonic anomalies have coalesced to form a broader area of elevated vorticity values (cf. Montgomery and Enagonio 1998; Möller and Montgomery 1999; Enagonio and Montgomery 2001). Thus, from pre-conditioning to merger, the cyclonic cores have increased in size and strength while the anticyclonic cores have weakened. This implies, at least qualitatively, that vorticity values have increased systematically between the two phases of Diana's development in the 3km simulation of H04.

4.3 Diana3 Experiment

4.3.1 Vorticity Field

To determine if indeed the distribution of low-level absolute vorticity has a positive bias, as suggested by visual inspection of the vorticity field for the H04 simulation, we computed area-averaged vertical vorticity ($\bar{\eta}$) over a 3° by 3° averaging box that moved with the storm center. In this case, we define $\bar{\eta}$ for a given pressure level p by:

$$\bar{\eta}(p) = \frac{1}{\mathrm{N}} \sum \eta(i, j, p), \tag{4.1}$$

where the sum is computed over all gridpoints (i, j) that lie within the 3° by 3° averaging

box. In equation (4.1) $\eta = f + \frac{\partial v}{\partial x} - \frac{\partial u}{\partial y}$ is the magnitude of the vertical component of absolute vorticity, where f is the Coriolis parameter, and N is the total number of gridpoints that lie in the averaging box. To compute area-averaged absolute vorticity, we use output data from the Diana3 simulation since comparable statistics were not computed in the H04 study. While this technique is not a strict analysis of the H04 output, it provides additional insight into the genesis of Hurricane Diana as simulated in a configuration of MM5 with dx = 3km, and it helps us to understand the resolution dependencies of the VHT route to tropical cyclogenesis. Since a well-defined circulation center does not emerge until approximately t = 12h, the center location of the averaging box is chosen to be fixed for the first 12 hours of the simulation at 26.7N and 77.6W (this is the approximate center of circulation at t = 12h). After t = 12h the center of the averaging box is located at the center of circulation and, as such, moves with the storm (see Figure 4.4 for the location of the averaging box with regard to the storm center). One further detail was must point out is that the average vorticity values are computed based on data from the 9km grid in the Diana3 simulation. This was done to ensure the area of the averaging box remained constant and the edges of the box did not extend outside of the domain boundaries.

Figure 4.5 is a time-height plot of the profile of area-averaged absolute vorticity from the Diana3 experiment. This plot reveals that area-averaged absolute vorticity is initially positive and remains positive and increasing with time during the first 36 hours of the simulation at all levels in the model atmosphere. While there are a few exceptions to this trend (e.g. at mid to upper-levels during the first 3 hours of the simulation and at mid-levels around 00UTC and 08UTC on 8 Sep), the vorticity in the genesis area

increases dramatically. Maximum average vorticity values in the column are initially on the order of $\bar{\eta} \approx 10 \times 10^{-5} s^{-1}$, and, by t = 36h, maximum values nearly triple to $\bar{\eta} \approx 30 \times 10^{-5} s^{-1}$ with the steepest rate of increase observed from 12UTC 8 Sep and 18UTC 8 Sep below $p \approx$ 500hPa. The increasing nature of the area-averaged absolute vorticity is most prominent at mid to low-levels where a ridge of maximum vorticity emerges near the p = 900hPa level. This ridge develops early in the simulation and is a highly visible feature throughout most of the 36hr period plotted. The dramatic increase in vorticity values near the surface is consistent with the results of H04 and M06 who showed that VHTs in the genesis environment increase the low-level vorticity due to the action of the secondary circulation fluxing mid to low-level angular momentum into the genesis region. We see evidence of this mechanism in Figure 4.5 beginning around t = 6h (18UTC 7 Sep) when convection first erupts and average vorticity values near p = 900hPa begin to increase significantly, presumably due the secondary circulation.

4.3.2 Divergence Field

To assess the impact of secondary circulations on the area-averaged vorticity fields, we also calculated area-averaged divergence values ($\bar{\delta}$) over the same averaging box used in the previous section (Figure 4.4). Similar to the area-averaged vorticity, we define the area-averaged divergence for a given pressure level p by:

$$\bar{\delta}(p) = \frac{1}{N} \sum \delta(i, j, p), \tag{4.2}$$

where the sum is computed over all gridpoints (i, j) that lie within the 3° by 3° averaging

box. In equation (4.2) $\delta = \nabla \cdot \mathbf{u}_h = \frac{\partial u}{\partial x} + \frac{\partial v}{\partial y}$ is the divergence of the horizontal wind, and N is the total number of gridpoints that lie within the averaging box. We may connect the impact of secondary circulations on the evolution of the absolute vorticity by examining the tendency equation of the vertical component of absolute vorticity (Holton 2004):

$$\frac{\partial \eta}{\partial t} = -\mathbf{u}_h \cdot (\nabla_h \eta) - \omega \frac{\partial \eta}{\partial p} - (\nabla \cdot \mathbf{u}_h)\eta - \left(\frac{\partial \omega}{\partial x}\frac{\partial v}{\partial p} - \frac{\partial \omega}{\partial y}\frac{\partial u}{\partial p} \right), \tag{4.3}$$

where we have used the pressure coordinate version to be consistent with the ordinate axis in our area-averaged plots. The third term on the right hand side of equation (4.3) represents the contribution of convergence/stretching to the tendency of the vertical component of absolute vorticity. Equation (4.3) says that, in a rotating environment ($\eta \neq 0$), convergent (divergent) flow results in a local increasing (decreasing) tendency in the absolute vorticity field. Examining our plot of area-averaged divergence for the 9km domain of the Diana3 simulation (Figure 4.6), we find that air in the portion of the atmosphere below $p \approx$ 600hPa is converging into the storm environment over the entire 36 hour period analyzed. This broad convergence is at least partly responsible for the overall increasing trend in the low to mid-level area-averaged absolute vorticity values seen in Figure 4.5. In particular the initial increase of area-averaged vorticity observed at 15UTC 7 Sep is coincident with an initial "burst" of low-level convergence at the same time near the p = 900hPa pressure level. Area-averaged convergence into the region persists at low-levels for the remainder of the period with the maximum convergence values generally observed in the vicinity of the p = 900hPa level, which is where we see the persistent low-level vorticity ridge emerge in Figure 4.5. The convergence becomes particularly strong between 15UTC 8 Sep and 18UTC 8 Sep below $p \approx$ 850hPa. As a

result, we see a distinct response in the area-averaged vorticity plot such that the low-level absolute vorticity experiences its largest rate of increase at this time. Thus, the significant increase of area-averaged low-level absolute vorticity observed for the Diana3 simulation can be explained in large part by the corresponding low to mid-level convergence in the area-averaged divergence profile.

The significantly depressed values of absolute vorticity observed at upper-levels (above $p \approx 400$hPa) can also be explained by the divergence profile. In particular, the upper-level minimum in the absolute vorticity at the beginning of the simulation is likely an artifact of the to the initial convergence maximum observed at this level. The lack of a significant increase in the upper-level area-averaged vorticity, particularly before 12UTC 8 Sep, is at least in part due to strong area-averaged divergence observed at upper-levels of the atmosphere. Though the biggest impact of the upper-level divergence pattern is on the trend in the area-averaged upper-level vorticity: where we see an increasing (decreasing) trend in the area-averaged divergence, the area-averaged vorticity generally decreases (increases).

In addition to helping explain the pattern and tendencies in the area-averaged absolute vorticity field, the area-averaged divergence profile also gives us insight into the convective or stratiform nature of the pre-genesis and genesis processes. Despite the storm's baroclinic origins, the pattern of a low-level convergence maximum near the surface underlying upper-level divergence suggests the environment in the Diana3 simulation strongly resembles a Convective Divergence Profile (CDP, Mapes and Houze 1995, Houze 1997, Tory et al. 2006a and 2006b). Furthermore, the significant increase of vorticity at low to mid-levels is consistent with the Convective Vortex Enhancement

(CVE) mechanism of tropical development discussed in Tory et al. (2006a and 2006b). What is most intriguing is the lack of a stratiform signature in the area-averaged divergence profile since we do not see any hint of low-level divergence in Figure 4.6. This suggests that convective processes and their direct and indirect impacts on the larger scale environment play a significant role in the tropical cyclogenesis process, at least for Diana3 experiment. Whether or not the VHT pathway is a common component of tropical cyclogenesis in most cases is yet to be determined. However, Tory et al. (2006a, 2006b, and 2007) showed that low-level convective processes in general and the CVE mechanism in particular were important for a number of tropical cyclones simulated by the Australian Bureau of Meteorology's Tropical Cyclone Limited Area Prediction System (TC-LAPS). This further suggests the importance of convective and VHT dynamics in the broader tropical cyclogenesis process.

As already discussed, the emergence of relatively high vorticity values in Figure 4.5 is initially observed at low-levels (generally below p = 750hPa) with a lag in the timing of increases observed at mid to upper-levels of the atmosphere and at the surface. These temporal and spatial lags in the increase of vorticity continue until the moment of tropical cyclogenesis.[5] After genesis the vorticity trend below p = 500hPa becomes more vertically uniform and generally independent of height as the warm core vortex deepens. The structure of the area-averaged vorticity at this point in the simulation is controlled more by the presence of the strong vorticity anomaly associated with the warm core cyclone rather than by the action of the VHTs themselves. All of these details are

[5] For purposes of our study, we treat the official naming of the storm by NHC forecasters to be the moment of cyclogenesis. This occurred at 15UTC 8 Sep 84 according to Bosart and Bartlo (1991). Both the Diana1 and Diana3 simulation exhibit evolutions of the vortex that are consistent with this timing of genesis.

consistent with the VHT pathway to tropical cyclogenesis and the expected trend in the vorticity field for low-level vorticity values increasing with time as the convection at the surface builds the tropical vortex (H04; M06; Tory et al. 2006a, 2006b and 2007).

In addition to the trend, the shape and vertical structure of the area-averaged vorticity are also consistent with the VHT route to tropical cyclogenesis. Referring again to the persistent ridge apparent in the low-level area-averaged vorticity field in Figure 4.5, we find that this feature, prior to $t \approx 12$h (00UTC 8 Sep), generally extends from $p \approx$ 900hPa to $p \approx 600$hPa. As the simulation progresses, the vorticity ridge deepens and extends from as low at $p = 950$hPa to as high as $p = 300$hPa during the pre-conditioning phase of development. The structure and evolution of the vorticity ridge is likely the result of the evolving nature of the VHT activity during the simulation prior to genesis. When convection first breaks out, it is not very well developed and the updraft cores are not very deep. The resultant tilting and stretching of vorticity in the updraft thus has limited vertical impact, and, as a result, the vorticity ridge only extends to mid-levels. At later times as the convection deepens with stronger updrafts extending to the tropopause, the impact of the tilting and stretching of vorticity in the VHT cores is felt to a greater depth of the atmosphere. This continues through pre-conditioning until the tropical vortex emerges and begins to control the evolution of the area-averaged vorticity profile.

4.3.3 Skewness of Absolute Vorticity

To help quantify the apparent bias of Diana3 vorticity toward positive values, we computed skewness of the absolute vorticity field on the 9km grid for three levels in the atmosphere (p = 900hPa, 600hPa and 400hPa). For our calculations of skewness, we

used the *MOMENT* function of the Interactive Data Language (IDL) where the skewness at pressure level p is defined by:

$$\text{skewness } (p) = \frac{1}{N}\sum\left(\frac{\eta(i,j,p)-\bar{\eta}(p)}{\sqrt{\text{variance}\,(p)}}\right)^3. \tag{4.4}$$

In equation (4.4) the variance at pressure level p is given by:

$$\text{variance } (p) = \frac{1}{N-1}\sum\left(\eta(i,j,p)-\bar{\eta}(p)\right)^2. \tag{4.5}$$

In equation (4.4) and equation (4.5) the summations are computed over all gridpoints (i,j) within the entire 9km grid (as opposed to the 3° by 3° box use for area-averaged calculations). Additionally, N is the total number of gridpoints in the 9km grid, $\eta(i,j,p)$ is the value of absolute of vorticity at pressure level p for the grid point (i,j), and $\bar{\eta}(p)$ is the average value of absolute vorticity defined by equation (4.1).

Analysis of the plots of skewness (Figure 4.7) suggests that the Diana3 absolute vorticity field has a significant bias toward values exceeding the mean over the entire 9km grid. This observation, coupled with the increasing trend in the area-averaged vorticity field, also suggests that the mean of the distribution should increase in time over the 9km grid. This tendency is consistent at each of the three levels plotted, and skewness values generally increase with time as the mean value increases with time (see Figure 4.5). The exception to this occurs at mid-levels of the atmosphere where a strong increase in skewness observed over the first 18 hours is followed by a moderate decrease (though skewness remains positive). Additionally, skewness is generally largest at lower levels which suggests that the most intense cyclonic anomalies are located near the surface. This is expected given that broad low-level convergence was observed within

the genesis region (Figure 4.6) with local maxima observed generally below the p = 900hPa pressure level. This feature is also consistent with the dipole nature of the vorticity anomalies and their vertical structure observed in the M06 experiments and is in-line with previous discussions of the low and mid-level vorticity structure of the Diana3 simulation in this dissertation.

4.3.4 Moisture Field

We now turn our attention to the evolution of the moisture field. In-line with much of the analysis thus far in this chapter, we will focus mainly on area-averaged moisture values computed over a 3° by 3° averaging box as an indicator of the moisture evolution on the mesoscale. Similar to the computations of area-averaged absolute vorticity and area-averaged divergence, we define area-averaged relative humidity by:

$$\overline{rh}(p) = \frac{1}{\mathrm{N}} \sum rh(i, j, p), \tag{4.6}$$

where the sum is computed over all gridpoints (i, j) that lie within the averaging box.

The averaging box used in this case is identical in size and location to the averaging box used in our discussion of area-averaged vorticity and divergence (see Figure 4.4). Since this aspect of the genesis of Diana was not discussed in the H04 simulation, we will not compare our output to the H04 data. The only other discussions of moisture evolution in Hurricane Diana were provided by Bosart and Bartlo (1991) and Davis and Bosart (2001). In both cases the authors suggested that moistening of the low to mid-levels of the atmosphere was an important component of the cyclogenesis event. Particularly, Davis and Bosart (2001) showed that the formation of Diana occurred in

three distinct phases, an initial episode of convective activity followed by a quiescent period of little deepening and moistening of the atmosphere and ending with a final phase of widespread convection and significant deepening of the emerging cyclone (see Figure 4.13).

A time-height plot of the area-averaged profile of relative humidity ($\overline{rh}$) at all levels of the model atmosphere for the Diana3 simulation is presented in Figure 4.8. This figure indicates that the Diana3 simulation is initially very moist (nearly saturated) at low to mid-levels of the atmosphere. Average relative humidity values exceed 90% between p = 750hPa and p = 900hPa, and this is most likely attributable to the artificial moistening of the initial conditions discussed in Section 2.3.2. This area of high humidity is embedded within a larger depth of moist air from the surface to the $p \approx$ 600mb pressure level where $\overline{rh} \geq 70\%$.

The evolution of the area-averaged relative humidity fields through the end of the pre-conditioning phase (12UTC 8 Sep, t = 24h) shows a general drying trend below the p = 600hPa pressure level. Relative humidity values during this time are reduced by as much as 10-20%, particularly in the layer between p = 800hPa and p = 600hPa. Below p = 800hPa the area-averaged relative humidity decreases slightly but remains moist with $\overline{rh}$ generally in the range $80\% \leq \overline{rh} \leq 90\%$, although isolated values greater than 90% do exist in this layer.

A mid-levels (p = 650hPa to p = 300hPa) a less distinct trend in the moisture field is observed over the first three to six hours of the simulation (up to approximately 18UTC 7 Sep). The layer between p = 650hPa and p = 450hPa experiences moisture increases of up to 10%, while the layer between p = 450hPa and p = 300hPa dries by approximately

the same amount. After 18UTC 7 Sep (t = 6h) the entire mid-level layer between p = 650hPa and p = 300hPa dries by as much as 20% to 30% in concert with the low-level drying trend. A local minimum of mid-level area-averaged relative humidity values emerges at 00UTC 8 Sep (t = 12h) when values fall to less than 40% at the p = 500hP pressure level. After t = 12h through the end of the pre-conditioning phase, most of the "lost" moisture is regained and the middle part of the atmosphere, in general, achieves and maintains area-averaged relative humidity values between 60% and 70%.

The trend at upper levels ($p \leq$ 300hPa) is distinct and is most obvious within the first six hours of the simulation (up through 18UTC 7 Sep). During this time upper level $\overline{rh}$ increases dramatic from initial values as low as 10% to achieve $\overline{rh}$ as high as 70%. This is particularly true at p = 200hPa, but the increase of $\overline{rh}$ occurs at all levels above p = 300hPa throughout the pre-conditioning phase. After t = 6h, the trend in the upper level area-averaged relative humidity field is generally flat in the sense that only modest moisture increases.

During the merger phase of Diana's development, most of the trends that were observed during pre-conditioning persist, except at the lowest levels of the atmosphere. The upper levels ($p \leq$ 300hPa) continue to experience moistening, in an area-averaged sense, until approximately 21UTC 8 Sep (t = 33h) when upper level $\overline{rh}$ values exceed 80%. After t = 33h, a slight decrease in $\overline{rh}$ is observed. And, at mid levels (roughly p = 300hPa to p = 650hPa), the moisture field maintains area-averaged relative humidity between 60% and 70% with no real trend observed. The exception to this occurs in the lowest 100hPa of this layer (roughly p = 500hPa to p = 600hPa) where a distinct increase of 10% to 20% is evident by the end the simulation. This increase in area-averaged

humidity is part of an increase observed at low-levels (approximately p = 600hPa to p = 975hPa) which also experiences $\overline{rh}$ increases of 10% to 20% by the end of the simulation. Furthermore, during the last 6 hours of the simulation, a very moist layer with $\overline{rh} \geq 90\%$ is evident between p = 850hPa and p = 950hPa.

4.4 Diana1 Experiment

4.4.1 Evolution of the Vorticity Field

We now examine details of our 1km simulation of Hurricane Diana, and compare this output to the coarser resolution results discussed above. For our high resolution experiment, the character of the VHT activity as represented by the evolution of the low-level absolute vertical vorticity field is qualitatively different from what was observed in the H04 simulation. Figure 4.9 shows plots of Diana1 absolute vertical vorticity at t = 22h, t = 23h and t = 24h. Though these times are not the same time periods plotted in Figure 4.2, the plots are nonetheless representative of the character of the absolute vorticity field during the pre-conditioning phase of development in the Diana1 experiment. We must also note that there is a slight difference in area of each plot resulting in 23% smaller domain for the H04 simulation than for the Diana1 simulation[6]. This fact notwithstanding, the general nature of the pre-conditioning VHT activity in our 1km simulation is noticeably different than in the H04 simulation, particularly with

[6] The plot box in Figure 4.2 is 438km by 438km while the plot box in Figure 4.9 is 508km by 490km. This results in an area that is about 23% smaller in Figure 4.2 compared to the geographic coverage in Figure 4.9, though the central latitude and longitude of each box are nearly identical.

regard to the finer scale features of each plot. While the H04 simulation exhibits on the order of 5 maxima in the vorticity field at any give time during pre-conditioning (Figure 4.2), as many as 50 maxima are resolved in the low-level absolute vorticity field or the Diana1 experiment over similar time periods (Figure 4.9). Additionally, the horizontal size of each core is noticeably smaller in the Diana1 experiment. However, the strength of the cyclonic cores is similar between the two experiments with maximum values generally in the range $3.5\times10^{-3}s^{-1} \le \eta \le 4.0\times10^{-3}s^{-1}$. For the anticyclonic cores in the Diana1 experiment, the trend toward more cores with smaller spatial scales continues, though it is difficult to compare intensity between the simulations because of the choice of contours. Despite this, a visual comparison of Figure 4.2 and Figure 4.9 suggests that the total field of anticyclonic vorticity is more intense in the Diana1 simulation than in the Diana3 simulation. That is, the negative vorticity cores are more numerous and appear to have a larger impact on the total absolute vorticity field in the Diana1 simulation.

Such a richer structure in the output is not unexpected as the Diana1 simulation employs approximately nine times the number of gridpoints than in the H04 and Diana3 simulations for a given area. While the results of H04 show a limited number of local vorticity maxima/minima, we see a vast array of these structures with no broad area of cyclonic or anticyclonic vorticity. This is in direct contrast to the H04 low-level absolute vorticity plot which reveals a smooth, nearly contiguous area of elevated vorticity associated with the frontal boundary and only a few isolated negative cores punctuating this region. A similar frontal structure is not as obvious in the Diana1 vorticity plots. While a region of generally higher cyclonic vorticity values is visible in Figure 4.9

oriented ESE to WNW and associated with nearly all of the strong cyclonic vorticity cores, this area of elevated vorticity is neither smooth nor continuous. Furthermore, the number of cyclonic cores is balanced by a nearly equal number of strong anticyclonic vorticity cores. As a result, it is not visually obvious whether the Diana1 9km grid has a positive or negative value of area-averaged absolute vorticity. Neither does the vorticity field in our 1km simulation exhibit the overall smoothness of texture observed in the H04 simulation. This is particularly true in the regions of the domain removed from the central genesis area/frontal zone. In the H04 output, there exists a very smooth area of weakly positive vorticity values both north and south of the frontal zone with only minimal, if any, negative vorticity cores in this part of the domain. However, in the Diana1 data, these weakly positive vorticity regions are punctuated by a multitude of weakly negative vorticity cores.

Further inspection of the differences between Figure 4.2 and Figure 4.9 reveals additional details that are of importance. Along with the more textured appearance of the low-level absolute vorticity field in our Diana1 simulation, we also see many more likely merger events than in the H04 results. While we only resolve one consolidation of vorticity in Figure 4.2 (H04) during the 3 hour period plotted, the Diana1 results suggest that as many as 10-20 mergers/consolidations occur over a similar time period. Despite this enhanced merger activity, a central vortex does not form at this stage in the development process. The mergers events create larger local maxima, in general, but a single dominant maximum in absolute vorticity does not emerge during the period plotted. This is consistent with the pre-conditioning phase of the development "priming" the atmosphere for the tropical cyclogenesis that is to follow. As suggested by H04 and

M06, the VHTs are not acting in a cooperative manner during this phase of Diana's development. The result of the individual mergers that occur are slightly stronger cores that persist for time periods that are comparable to the life cycle of the original vorticity anomalies themselves. This characteristic was also observed during the preconditioning phase in the H04 simulation.

During the merger phase of development ($t \approx$ 24h to $t \approx$ 36h), many of the differences noted between the Diana3 and Diana1 simulations persist. Figure 4.10 is a plot of the evolution of low-level absolute vorticity during the merger phase of Diana1 experiment from t = 25h to t = 32h. Whereas plots in Figure 4.3 are 30min apart (left to right), plots in Figure 4.10 are 1hr apart (left to right) with time periods of the plots similar to those in Figure 4.3. Despite the change in temporal differencing in each figure, we may compare the qualitative details of the two simulations without loss of generality because: 1) the typical life cycle of an individual VHT is on the order of 1 hour, 2) the consecutive plots in both figures cover time periods of 1 hour or less, 3) the timing of the vortex merger phase is approximately the same in each experiment and 4) similar time periods are plotted for each experiment.

In contrast to the 3km results (Figure 4.2 and Figure 4.3), only a slight systematic increase in the low-level absolute vorticity field is observed in the Diana1 experiment between the pre-conditioning and merger phases (Figure 4.9 and Figure 4.10, respectively). The number of cyclonic cores and the size of those cores is approximately the same with magnitudes that are comparable to the cyclonic anomaly magnitudes during pre-conditioning. The exception to this appears to be with the emergence of the strong central vortex after t = 29h. Typical maximum vorticity values in Diana1 VHT

cores lie generally in the range $3.5\times10^{-3}s^{-1} \le \eta \le 4.0\times10^{-3}s^{-1}$. As during pre-conditioning, these values are more intense than the typical maximum vorticity values observed in the H04 simulation. If we analyze the Diana1 anticyclonic anomalies in Figure 4.10, we see generally the same number and strength of anticyclonic cores relative to the pre-conditioning phase. And, we continue to see significantly more negative vorticity cores of smaller spatial scales than what was observed in the H04 simulation.

Having already noted the differences in number, size, and strength of the vorticity anomalies, we now compare the horizontal distribution of low-level absolute vorticity between the two simulations. In the H04 simulation, a large, nearly contiguous, area of elevated cyclonic values oriented SW through NE was routinely observed in the data, particularly during pre-conditioning (Figure 4.2 and Figure 4.3). While this region diminished in aerial extent over time, it served as a ready source of elevated low-level vorticity for the emerging central vortex. However, a similar structure is noticeably absent from the low-level absolute vorticity data in our 1km data. In the early period of the Diana1 vortex merger phase (top row of Figure 4.10) most of the cyclonic vorticity anomalies are generally located ESE to WNW through the domain center. However, unlike H04, this region of generally positive vorticity is patchy and contains most of the negative vorticity cores as well. Furthermore, as the vortex merger phase progresses and the tropical cyclone becomes well defined, many of the vorticity anomalies (both cyclonic and anticyclonic) are eradicated from the cyclone center. This results in a vortical environment around the emerging storm that is not as broad as in the H04 simulation. As a result, the low-level cyclonic vorticity in the Diana1 experiment is more highly concentrated in the immediate vicinity of the storm center relative to the

horizontal distribution of the low-level vorticity in the H04 study (and the Diana3 experiment, not shown). This is the result of two complimentary processes that occur quite visibly in the Diana1 experiment: (1) the central vortex grows both in size and in strength and axisymmetrizes several smaller scale cyclonic anomalies into the storm center and (2) the anticyclonic vorticity anomalies near the central vortex are completely annihilated by this axisymmetrization process. As such, a "moat" of relatively weak vorticity values develops within about 100km of the emerging storm, and vorticity values in the immediate vicinity of the central vortex fall off quite rapidly (over a much shorter distance than in the 3km simulation). This gives the appearance of an isolated strong anomaly in the low-level absolute vorticity field. No such similar feature was observed in the H04 simulation as the vorticity in the immediate vicinity of the central vortex appears as an extension of vorticity in the core.

4.4.2 Area-Averaged Vorticity

Because of the size and general intensity of the anticyclonic vorticity field in the Diana1 simulation, it is unclear by visual inspection of Figure 4.9 whether or not the average value of absolute vorticity in the genesis region has increased or is even cyclonically skewed as H04 and M06 suggest should be the case (and as was the case in our Diana3 results). More than likely, the absolute vorticity field has at least maintained the cyclonic bias observed in the initial conditions (see Figure 3.3), but this not visually apparent either. To determine if the aggregate vorticity field has at least maintained its initial cyclonic bias and possibly increased due to the action of the VHTs, we calculated area-averaged absolute vorticity ($\overline{\eta}$) over a 3° by 3° box located within the genesis area

(see Section 4.3.1 for a description of the methodology used). Since a well-defined circulation center does not emerge until approximately t = 24h, the location of the center of the box is chosen to be fixed for the first 24 hours of the simulation at 28.6N and 77.5W (this is the approximate center of circulation at t = 24h). After t = 24h the center of the averaging box is located at the center of circulation and, as such, moves with the storm (see Figure 4.11 for a depiction of the averaging box). The reader will note that this is different from the Diana3 simulation in which we fixed the central location of the box until t = 12h. The reason the box is fixed until t = 24h in our Diana1 experiment is to be consistent with our previous analysis technique which held the box fixed until a clear circulation center formed in the surface wind and sea-level pressure fields. Since the circulation center did not emerge until later in the Diana1 simulation than in the Diana3 simulation, the averaging box is held fixed in the Diana1 simulation for a longer period of time.

Figure 4.12 is a plot of the evolution of $\overline{\eta}$ at three pressure levels in the atmosphere (p = 925hPa, p = 700hPa, and p = 500hPa). This plot shows a few interesting details that must be noted. First, the curve in Figure 4.12 indicates the area-averaged vorticity is always cyclonic which suggests the vorticity over the averaging box has indeed maintained a positive bias. Second, the trend in the area-averaged absolute vorticity field is such that the values are generally increasing with time, particularly at the lowest levels (p = 925hPa and p = 700hPa). The exception to this occurs at p = 500hPa where the area-averaged absolute vorticity loses roughly 25% of its value between 07UTC 7 Sep and 13UTC 7 Sep (t = 19h and t = 25h) before again experiencing an increasing trend. Nonetheless, the trend over the whole simulation is such that the area-averaged vorticity

nearly doubles at all levels of the atmosphere by the end of the simulation. These two observations ($\bar{\eta}$ positively skewed and increasing with time) were suggested by both H04 and M06, but M06 was the first to explain the underlying physical mechanism and make the direct connection to VHT dynamics. The M06 results showed that absolute vorticity dipoles created by the VHT convective cores displayed a distinct bias toward the cyclonic lobe such that the area of positive vorticity was larger and more intense than the vorticity associated with the anticyclonic lobe. This bias resulted in a positive contribution to the absolute vorticity field over the course of the M06 simulation. Our results here further validate these M06 results, especially at low-levels, and are consistent with the area-averaged vorticity profiles computed for the Diana3 simulation (Figure 4.5). Since the outbreak of convection is the major activity taking place in the genesis area during this period, one must conclude that the increase in vorticity is largely due to the VHT activity, directly or indirectly. M06 suggested a system scale increase in cyclonic vorticity was indeed a direct result of VHT anomalies and associated updraft cores that tended to strengthen the cyclonic vortices over anticyclonic vortices (in addition to the system scale spin-up due to the mean radial fluxes of mean absolute vorticity and the effects of broad-scale upper-level divergence, which we'll discuss later).

The last observation of Figure 4.12 we'd like to note pertains to the three distinct phases of development evident in the low level absolute vorticity plot (p = 925hPa). We may delineate these phases by visual inspection of the slope of the curve, or equivalently the time rate of change of circulation. Using the change in the slope of the curve as a guide, we see a relatively quiet or flat initial period of activity (approximately 12UTC 7 Sep to 00UTC 8 Sep), followed by rapidly increasing average vorticity values

(approximately 00UTC 8 Sep to 12UTC 8 Sep), with another quiet or flat period thereafter (approximately 12UTC 8 Sep to 00UTC 9 Sep). This three phase development process was very similar to the evolution of the vortex in the DB01 study (see Figure 4.13). Dynamically, these changes in the slope of the curve are associated with an initialization/model spin-up phase, a second period we refer to as a pre-conditioning or vortical generation phase and a merger/consolidation phase, respectively. All three of these phases can be tied directly to the VHT activity taking place at the time. The first phase, model initialization/spin-up, is characterized by the initiation of convection in the field. During this early phase, the convection is neither widespread nor deep enough to have a noticeable impact on the secondary circulation and resultant flux of angular momentum into the genesis area. As a result the response of the area-averaged absolute vorticity is flat with no appreciable change in the low-level average absolute vorticity. By the second phase, pre-conditioning, the convection has deepened and become widespread such that a strong secondary circulation has developed with convergence into the averaging box at low to mid-levels and divergence at upper-levels (see Figure 4.16). As a result, $\overline{\eta}$ increases dramatically with time. During the final phase of development, the merger/consolidation phase, the low-level area-averaged absolute vorticity values have increased, but only slightly so, as the VHT dynamics become more associated with consolidation of vorticity through mergers of existing anomalies rather than the generation of new vorticity anomalies. The reader will note that the largest increase of $\overline{\eta}$ during the merger phase occurs at the p = 500hPa pressure level (approximately 50% increase from t = 24h to t = 36h). The reason for this rapid change is due to the timing of a nearly equal decrease that occurred at the end of the pre-conditioning phase. If one

examines the change in area-averaged vorticity at the p = 500hPa pressure from model initialization to the end of the simulation, the total increase is quite similar to what was observed at the other levels of the atmosphere. However, Figure 4.12 does suggest that the largest increases of $\overline{\eta}$ in the Diana1 simulation occurred at low to mid-levels of the atmosphere (in terms of percentage change).

To get a more complete picture of the absolute vorticity tendency at all levels in the atmosphere, we computed time-height plots of area-averaged vorticity values for the Diana1 experiment (Figure 4.14). Comparing this figure versus the corresponding figure for the Diana3 simulation (Figure 4.5), we find that the increase of $\overline{\eta}$ is systematically larger in the Diana3 simulation. According to Figure 4.14 the maximum value of area-averaged vorticity in the column for the Diana1 simulation increased by approximately 90% over the course of the simulation (initial $\overline{\eta}_{\max} \approx 10\times10^{-5}\,\mathrm{s}^{-1}$ compared to final $\overline{\eta}_{\max} \approx 19\times10^{-5}\,\mathrm{s}^{-1}$). The corresponding increase of maximum area-averaged vorticity for the Diana3 simulation is approximately 210% over the same time period (initial $\overline{\eta}_{\max} \approx 10\times10^{-5}\,\mathrm{s}^{-1}$ compared to final $\overline{\eta}_{\max} \approx 31\times10^{-5}\,\mathrm{s}^{-1}$). Furthermore, the maximum increase for the Diana1 simulation occurs slightly higher in the atmosphere at $p \approx$ 650hPa compared to $p \approx$ 850hPa for the Diana3 case. Incidentally, this is consistent with the M06 study in which a mid-level spin-up was observed prior to the development of the surface cyclone.

4.4.3 Skewness of Absolute Vorticity

These differences in the evolution of the area-averaged vorticity for each simulation

are echoed in calculations of skewness of the absolute vorticity field. In Figure 4.7 we saw that the vorticity field during the Diana3 experiment was positively skewed at all levels, and the skewness generally increased with time and decreased with height. This suggested that strong cyclonic vorticity anomalies dominated the entire column (though they were strongest at low-levels) and became stronger as the simulation proceeded. Contrast this with Figure 4.15 which shows skewness values for the Diana1 simulation. This plot reveals a similar vertical and temporal structure with positive vorticity anomalies generally increasing in time and decreasing with height (relative to the mean field). However, there are two significant differences that distinguish the character of the evolution of absolute vorticity in the Diana1 experiment. First, although both simulations generally have positively skewed vorticity distributions, the magnitudes of the skewness values are considerably weaker in the Diana1 simulation compared to the Diana3 simulation. This suggests that the anomalies present in the Diana1 experiment are generally weaker relative to the mean field of vorticity with a larger contribution from anticyclonic anomalies (this is consistent with the plots of absolute vorticity analyzed thus far). The second major difference is related to the first but must be pointed out in its own right. The skewness values at all levels in the Diana3 simulation are greater than zero during the almost the entire simulation, except for a few isolated incidents within the first 9 hours. This suggests the Diana3 experiment is consistently dominated by cyclonic anomalies at all levels. However, for the Diana1 simulation, upper-level skewness (p = 400hPa) varies significantly between positive and negative values with a mean near zero, particularly during the merger phase. This suggests the upper-levels in the Diana1 simulation are occasionally dominated by anticyclonic vorticity anomalies. This

difference, along with other differences noted regarding the structure and distribution of the absolute vorticity field between the simulations, implies that the Diana1 simulation is able to represent more VHT generated anticyclonic vorticity anomalies than the Diana3 simulation. And, in particular, the Diana1 simulation is simulating a disproportionately larger number of anticyclonic cores at upper levels of the atmosphere than near the surface. It is intriguing that the local and system scale processes in our high resolution case are able to overcome the adverse influence of anticyclonic vorticity in the column and still generate a warm core vortex. The processes that enable this to take place are examined more closely in Chapter 5.

4.4.4 Divergence Field

We now examine the time evolution of the area-average divergence profile ($\overline{\delta}$) to augment the analysis of the area-averaged absolute vorticity field above. The averaging box used for this calculation is the same as the box used to compute area-averaged-absolute vorticity (see Figure 4.11), and the methodology used is described in Section 4.3.2. The Diana1 area-averaged divergence profile (Figure 4.16) indicates very weak low-level convergence during most of the spin-up/initialization phase of the simulation (up through approximately 18UTC to 21UTC 7 Sep, t = 6h to t = 9h). In fact, the zero line in Figure 4.16 is oriented such that the first 3 to 6 hours of the simulation are nearly non-divergent in an area-averaged sense; this results in a flat response in the area-averaged absolute vorticity field through most of the depth of the atmosphere (Figure 4.14). It is only during the last 3 hours of model initialization (21UTC 7 Sep to 00UTC 8 Sep, t = 9h to t = 12h) that we see a significant amount of low and mid-level convergence

into the genesis region. Because of this, it may be more appropriate to refer to the time period between 21UTC 7 Sep and 00UTC 8 Sep as the beginning of the pre-conditioning phase rather than the end of the spin-up/initialization phase of development in the Diana1 simulation. Regardless, the structure of the $\overline{\delta}$ profile suggests the early stages in the simulated development of Hurricane Diana are characterized by significant convective activity as indicated by the convergence at the surface between 21UTC 7 Sep and 03UTC 8 Sep. The mid-level convergence maxima at 00UTC 8 Sep also suggests a potential stratiform component to the precipitation, but this is not a pure Stratiform Divergence Profile (SDP, respectively, Houze 1995, Mapes and Houze 1997, Tory et al. 2006a and 2006b) since significant convergence exists from the surface up through $p \approx 350$hPa. The noteworthy convergence near the surface suggests that early stage convective activity also has a significant role in the formation of Hurricane Diana. In fact, the vertical structure of the Diana1 divergence profile suggests a superposition of convective and stratiform precipitation modes is active at this time implying the importance of both in the genesis process. It is also noteworthy that a similar SDP type signature was not observed in the Diana3 simulation, which more closely resembled a divergence-over-convergence convective profile throughout the simulation (see Figure 4.6). This suggests the stratiform mode is more fully resolved in our Diana1 experiment.

Figure 4.16 also provides evidence of the two stage cyclogenesis process espoused by H04 and M06. Our area-averaged divergence profile shows two primary convective episodes: one during the pre-conditioning phase from approximately 21UTC 7 Sep to 03UTC 8 Sep (t = 9h to t =15h) when the convection is neither widespread nor very deep, followed by a second convective episode with deeper and more widespread convection

from approximately 06UTC 8 Sep to 18UTC 8 Sep (t = 18h to t = 30h). This is in-line with the area-averaged vorticity profiles which indicate a similar episodic evolution of the convective activity. It is also consistent with DB01 who showed the genesis of Diana underwent three primary phases (in order): an early period (up through t = 34h) of significant convective activity and baroclinic/barotropic growth resulting from latent heat release, a quiescent period lasting approximately 10 hours in which the convection was significantly reduced with little deepening of the emerging tropical cyclone, and a final episode of intense convection and rapid deepening of the storm (beginning at approximately t = 44h, see Figure 4.13).

The evolution of the divergence field associated with this three stage process can help to explain trends in the area-averaged absolute vorticity field discussed in Section 4.4.2. The location of the upper-level minimum and mid-level maximum in $\overline{\eta}$ near 03UTC 8 Sep corresponds quite nicely with the upper-level divergence and mid-level convergence maxima present at roughly the same time in Figure 4.16, respectively (though there is a three to six hour lag between appearance of the $\overline{\delta}$ extrema and the $\overline{\eta}$ extrema). Additionally, the near-surface convergence also produces as positive response in the low-level area-averaged absolute vorticity field with values increasing rapidly as the low-level convergence develops. A close comparison between Figure 4.16 and Figure 4.14 show generally good agreement between areas of convergence (divergence) and increasing (decreasing) values of area-averaged absolute vorticity, particularly up through the beginning of the merger phase of development.

4.4.5 Moisture Field

We now turn our attention to the evolution of the area-averaged relative humidity ($\overline{rh}$) field observed in the Diana1 simulation. The averaging box used for these calculations is identical to that used to compute area-averaged absolute vorticity and divergence (see Figure 4.11). See Section 4.3.4 for a description of the methodology used to compute $\overline{rh}$. The plot of area-averaged relative humidity at all levels of the Diana1 model atmosphere is presented in Figure 4.17. Comparing this plot to the Diana3 area-averaged relative humidity plot in Figure 4.8, we see similar trends, particularly below the p = 600hPa pressure level. Both simulations are initially very moist at low to mid-levels with the Diana1 simulation showing initial moisture up through a greater depth than in the Diana3 run. This is the case despite the artificial moistening of the initial conditions for the Diana3 simulation (see Section 2.3.2). The biggest difference in the initial conditions occurs between p = 300hPa and p = 500hPa where the Diana1 moisture field exhibits a local maxima of $\overline{rh}$ exceeding 80%. The corresponding levels in the Diana3 simulation indicate initial values between 60% and 70% in this layer. Generally speaking, initial $\overline{rh}$ in the layer between p = 650hPa and p = 300hPa is roughly 20% greater in the Diana1 experiment than in the Diana3 experiment.

Beyond these differences in the initial moisture, the evolution of $\overline{rh}$ through the beginning of the pre-conditioning phase (00UTC 8 Sep) is similar. In both cases, the low to mid-levels below p = 400hPa experience a drying trend whereby relative humidity values are reduced by as much as 30%. But this drying tendency is most pronounced near the p = 500hPa pressure level. How the dry air is entrained into the mid-levels, though, is distinctly different between the two simulations. In the Diana3 experiment (Figure 4.8), the emergence of the mid-level moisture minima appears disconnected from

the moisture trends at other levels as if this dry layer is due to horizontal advection of air from outside the averaging box. This is in contrast to the dry layer that emerges in the Diana1 experiment (Figure 4.17) in which air appears to descend from the upper levels presumably due to large scale subsidence. A closer examination of Figure 4.17 reveals that the tendency at p = 500hPa is also consistent with horizontal advection of dry air. This suggests that both horizontal entrainment of dry air and large scale subsidence are likely at play in the Diana1 simulation. Thus, while both simulation generate a moisture minima at 00UTC 8 Sep (t = 12h) at about the same level in the atmosphere, the Diana1 experiment appears to resolve large scale subsidence that did not appear in the Diana3 data.

The second major difference between the Diana1 and Diana3 simulations is in the mid to upper-levels of the atmosphere between 00UTC and 06UTC 8 Sep. During this time, there is a distinct moistening of the column in the 1km simulation that does not occur in the 3km simulation. Relative humidity values above p = 650hPa in the Diana1 results are greater than 80% up through p = 200hPa. The same layer in the Diana3 simulation has maximum relative humidity values less than 70% during this time. This column moistening in the Diana1 simulation is coincident with an initial low and mid-level convergence maximum in the area-averaged divergence fields (Figure 4.16), suggesting a burst of deep convective activity that is able to efficiently transport moisture upward. While the lower levels of the atmosphere in the Diana3 simulation experience convergence, such a strong convergence maximum at mid to lower levels is noticeably absent in the Diana3 area-averaged divergence profile (Figure 4.6).

After 06UTC 8 Sep and through the end of the pre-conditioning phase, the area-

averaged relative humidity takes on a similar evolution in both numerical experiments. Both the Diana1 and Diana3 runs show a trend toward increasing values of low to mid-level relative humidity (below p = 600hPa) with a maximum greater than 90% observed around 09UTC 8 Sep. For both simulations this maximum occurs at approximately the same time as the start of an increasing trend in low-level convergence (see Figure 4.6 and Figure 4.16) suggesting a second burst of convective activity in both simulations. At the upper-levels of both model in a layer roughly between p = 300hPa and p = 100hPa, the similarities continue in the sense that both models exhibit persistent moisture with relative humidity greater than 70%. However, the trends in this layer are out of phase in each simulation. Relative humidity profiles suggest upper-level moisture in the Diana1 simulation (between $p \approx$ 150hPa and $p \approx$ 250hPa) is decreasing as a function of time, while upper-level moisture in the Diana3 simulation is increasing (both these trends are valid after 06UTC 8 Sep). At mid-levels of the atmosphere between p = 600hPa and p = 300hPa, both models exhibit $\overline{rh}$ generally less than 70%. But the trend in the Diana1 simulation is toward drying conditions, while the Diana3 $\overline{rh}$ values remain relatively constant between 60% and 70%.

During the merger phase these trends continue. In both simulations the low-levels continue to humidify through t = 36h with $\overline{rh}$ values greater than 90%. At mid-levels, both simulations are relatively dry, but the tendencies in each case are noticeable different. Area-averaged relative humidity in the Diana3 experiment exhibits no appreciable change through the entire merger phase and maintains $\overline{rh}$ generally between 60% and 70%. This directly contrasts the Diana1 results, which show significant drying at mid-levels over the last 12 to 15 hours such that $\overline{rh}$ fall to as low as 40% by t = 36h.

At upper-levels, while both models have a local maximum of relative humidity, the Diana3 simulation experiences a moistening trend that results in an area-averaged relative humidity value greater than 80% compared to a 70% to 80% in the Diana1 simulation.

What is most intriguing is the mid-level dry tongue that emerges in the area-averaged relatively humidity field of both simulations. In an attempt to determine the source of the dry air in the Diana1 experiment, we computed back trajectories on the p = 450hPa surface over a 20 hour period ending at 20UTC 8 Sep 84 (t = 12h to t = 32h). We chose this pressure surface since the area-averaged relative humidity minimum observed at the end of the Diana1 simulation is centered at approximately p = 450hPa (Figure 4.17). Figure 4.18a shows that most of the dry air in the genesis region originated from two locations: 1) over the eastern seaboard, or 2) over the Florida peninsula. Both these locations were initially dry with relative humidity less than 50% at p = 500hPa (see Figure 3.12a). As the simulation progressed and a mid-level cyclone developed east of the Florida peninsula (see Figure 3.5), the wind field advected this dry air into the genesis region creating a dry slot over the Bahamas by t = 12UTC 8 Sep (t = 24h, Figure 3.12c and Figure 4.18c). By 00UTC 8 Sep (t = 36h), this dry slot had wrapped around the emerging mid-level cyclone such that relatively moist air (rh generally 60% to 80%) existed over the cyclone center and toward the south and southwest. Areas to the west, north, and east of the cyclone were significantly drier (rh < 50%, Figure 3.12d and Figure 4.18d). As a result of the dry air advection into the genesis region, $\overline{rh}$ in the Diana1 experiment fell to less than 40% by t = 36h. The fact that this is a consistent feature in both simulations (though more obvious in the Diana1 simulation) suggests that system scale mid-level moistening is not a necessary condition for the genesis of Hurricane

Diana. In fact despite the detrimental affects of the mid-level dry air, the genesis process is able to proceed, presumably due to the action of the convective cores and their aggregate effects on the larger scale vortex.

4.5 Summary and Analyses of Mesoscale Results

Based on the above analysis, it has become clear that the general nature of VHT pathway to tropical cyclogenesis proposed by H04 and M06 does indeed have a dependence on resolution in terms of the resolvability of smaller scale features (as least as far as the development of Hurricane Diana is concerned). The VHT associated vortical structures that emerged in our Diana1 simulation were decidedly more textured than what was observed in H04 simulation. Our 1km simulation had nearly an order of magnitude increase in the number of vorticity anomalies (cyclonic and anticyclonic) and merger events compared to H04. Furthermore, the basic structure of the low-level vorticity field was significantly different with anticyclonic cores permeating the entire field in the Diana1 compared to the more continuous nature of the data in the H04 case. This was particularly true during the vortex merger phase in which the anticyclonic vorticity anomalies so clearly evident in the high resolution run were nearly absent in the H04 simulation.

More important to the study at hand is the question of whether or not the change in resolution resulted in a fundamental change in the underlying physics associated with the VHT pathway to tropical cyclogenesis. In our high resolution simulation, we found the basic physics of the VHT activity during both the pre-conditioning and vortex merger phase remained essentially the same compared to the coarser resolution runs of H04 and

M06. In both coarse and fine resolution experiments, diabatically generated vorticity anomalies develop and are associated with deep convective updraft cores. In the pre-conditioning phase, these vortical hot towers permeate the entire genesis area and act in a non-cooperative manner rather than collaborating with each other to create a long-lived master or central vortex. While mergers events do occur during this phase, the end result of these mergers are slightly larger vortices of compare life spans to the original pre-merger vortices. During the vortex merger phase, the VHTs begin to "work together" in the sense that disparate vorticity anomalies begin to axisymmetrize to create a master vortex, and the self-sustaining tropical cyclone is born. In both simulations this merger process occurs first in the region of the domain with the most intense convection. In the H04 simulation, we see a very broad area of elevated cyclonic vorticity values in the immediate vicinity of the emerging vortex core, while the high resolution run shows a slightly different view as nearly all the vorticity anomalies within 100km of the vortex center become axisymmetrized in the central core. However, the action of the VHT activity in each simulation is such that area-averaged low-level absolute vorticity values increase during the model evolution as vorticity dipoles develop which are biased toward larger and more intense cyclonic lobes (compared to the anticyclonic lobes). All of these features were observed quite clearly in both the fine and coarse resolution simulations with an evolution that did not appear to be resolution dependent. While visual inspection of the coarse resolution results showed this aspect of the VHT pathway quite clearly, we had to analyze area-averaged vorticity values (i.e., net circulation) to confirm this result in the high resolution simulation. This again points to the more textured and more highly varied fine scale structure in the high resolution results. Thus, while the fine scale

features associated with the VHTs and the corresponding low-level vorticity field are significantly different between the two simulations, the basic physics appear largely unchanged as resolution increases. This suggests that the two phase tropical cyclogenesis paradigm proposed by H04 does not have a distinct resolution dependence at these scales, at least as far as the development of Hurricane Diana is concerned.

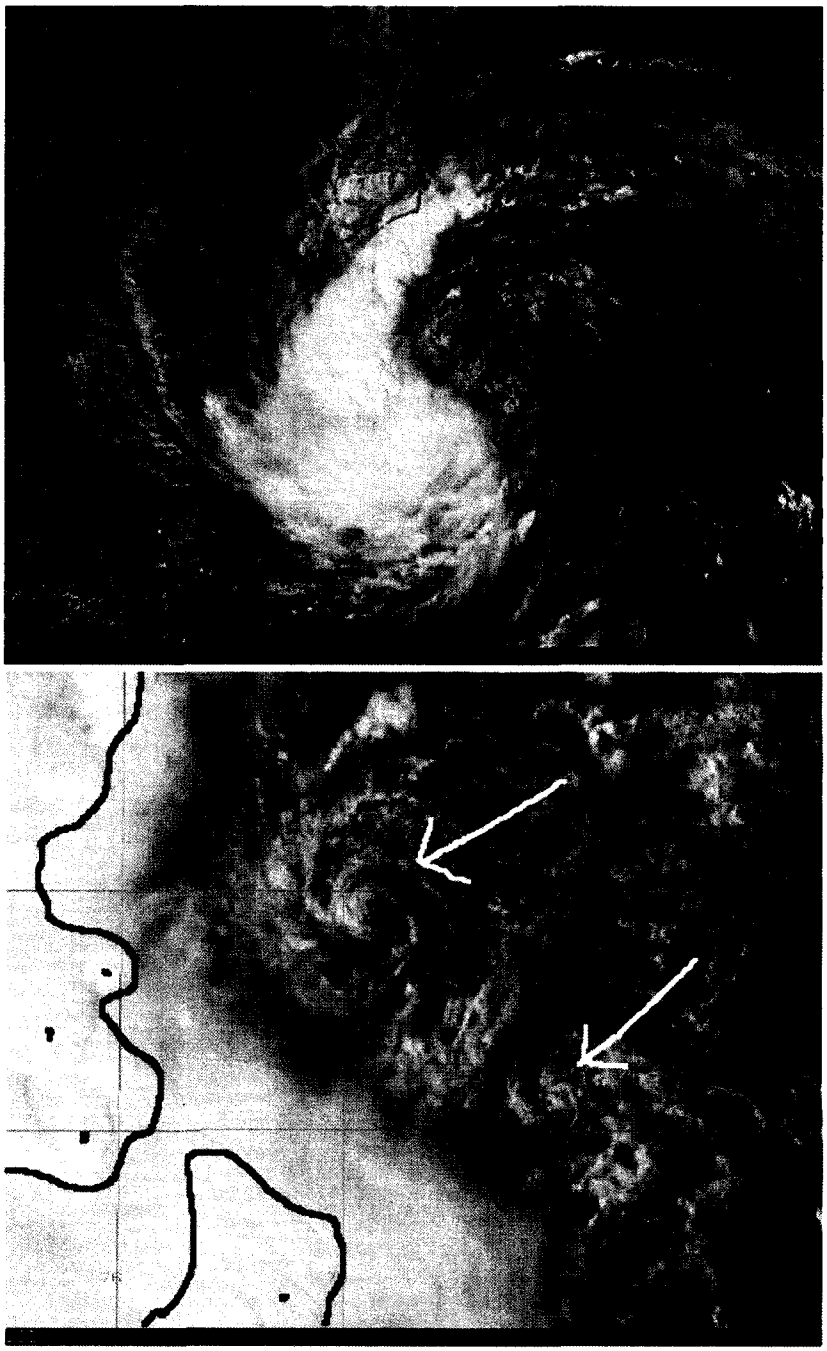

Figure 4.1. Satellite image of Tropical Storm Gustav at 1925UTC 9 Sep 2002. The bottom image is a close up view of a portion of the top image to focus in on the small scale features in the cloud-field. Note that the storm is sheared from the northeast revealing apparent low-level vortices that are presumably rotating remnants of VHTs (taken from Figure 3 of H04).

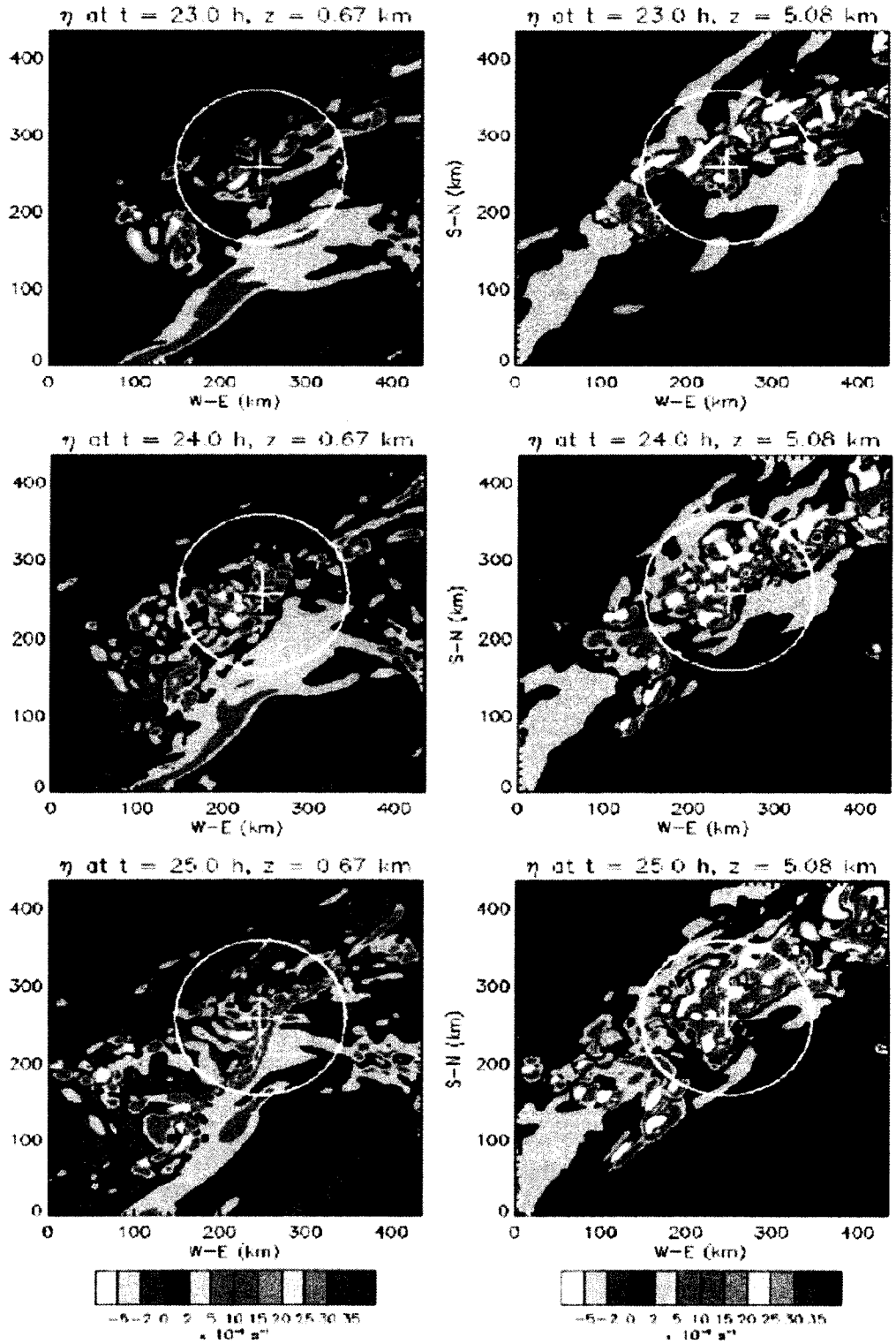

Figure 4.2. Absolute vorticity field at z = 0.67km (left column) and z = 5.08km (right column) during the pre-conditioning phase of development in the H04 simulation. Time periods from top to bottom are 11UTC 8 Sep 84 (t = 23h), 12UTC 8 Sep 84 (t =24h) and 13UTC 8 Sep 84 (t = 25h), respectively (taken from Figure 7 of H04).

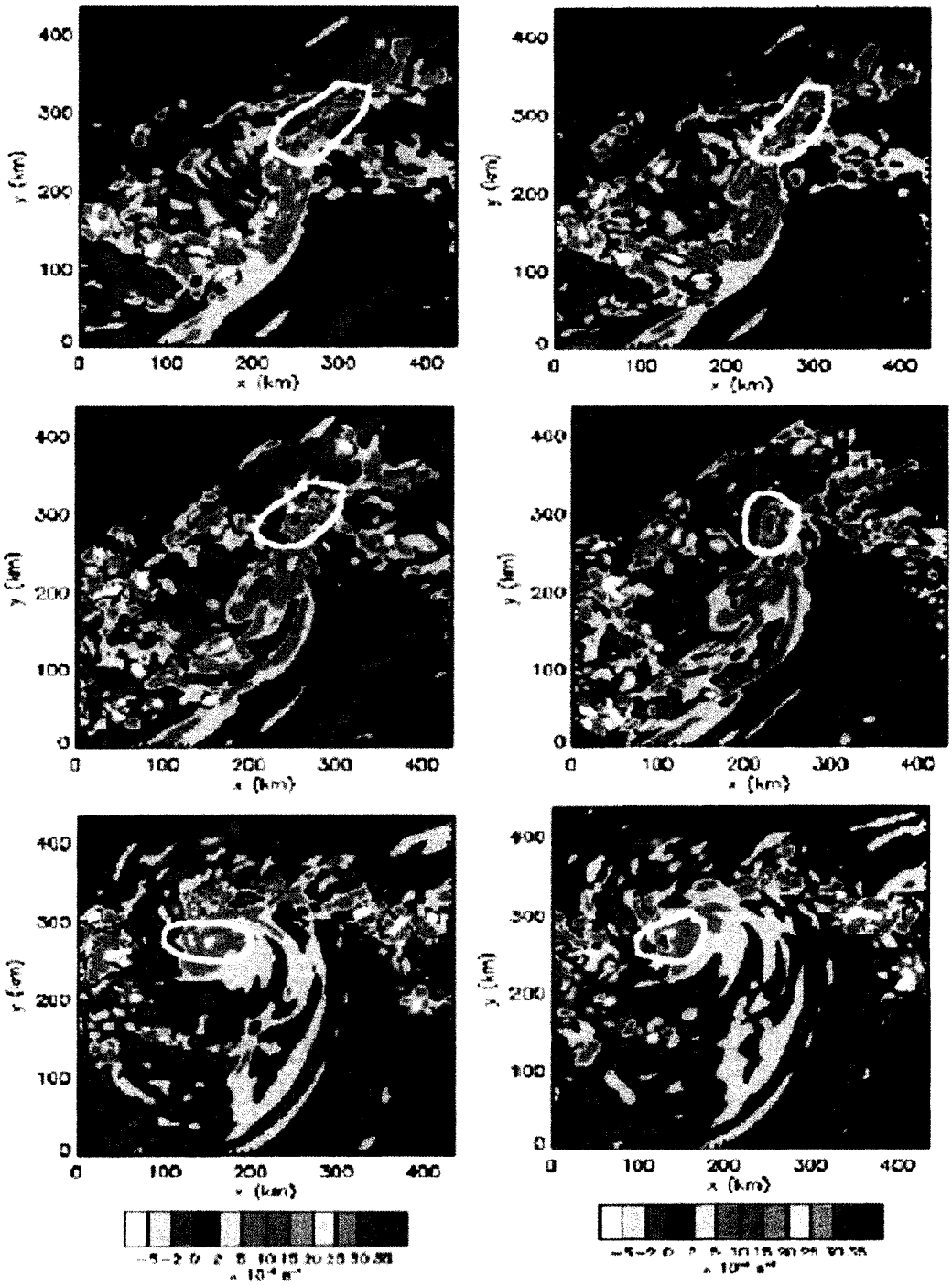

Figure 4.3. Absolute vorticity field at z=0.67km during the merger phase of development in the H04 simulation. Time periods for each row from top to bottom are temporally centered on 14UTC 8 Sep 84 (t = 26h), 15UTC 8 Sep 84 (t = 27h) and 21UTC 8 Sep 84 (t =33h) respectively. The image in the left column of each row corresponds to a time period 30 minutes before the time of the image in the right column of each row (taken from Figure 10 of H04).

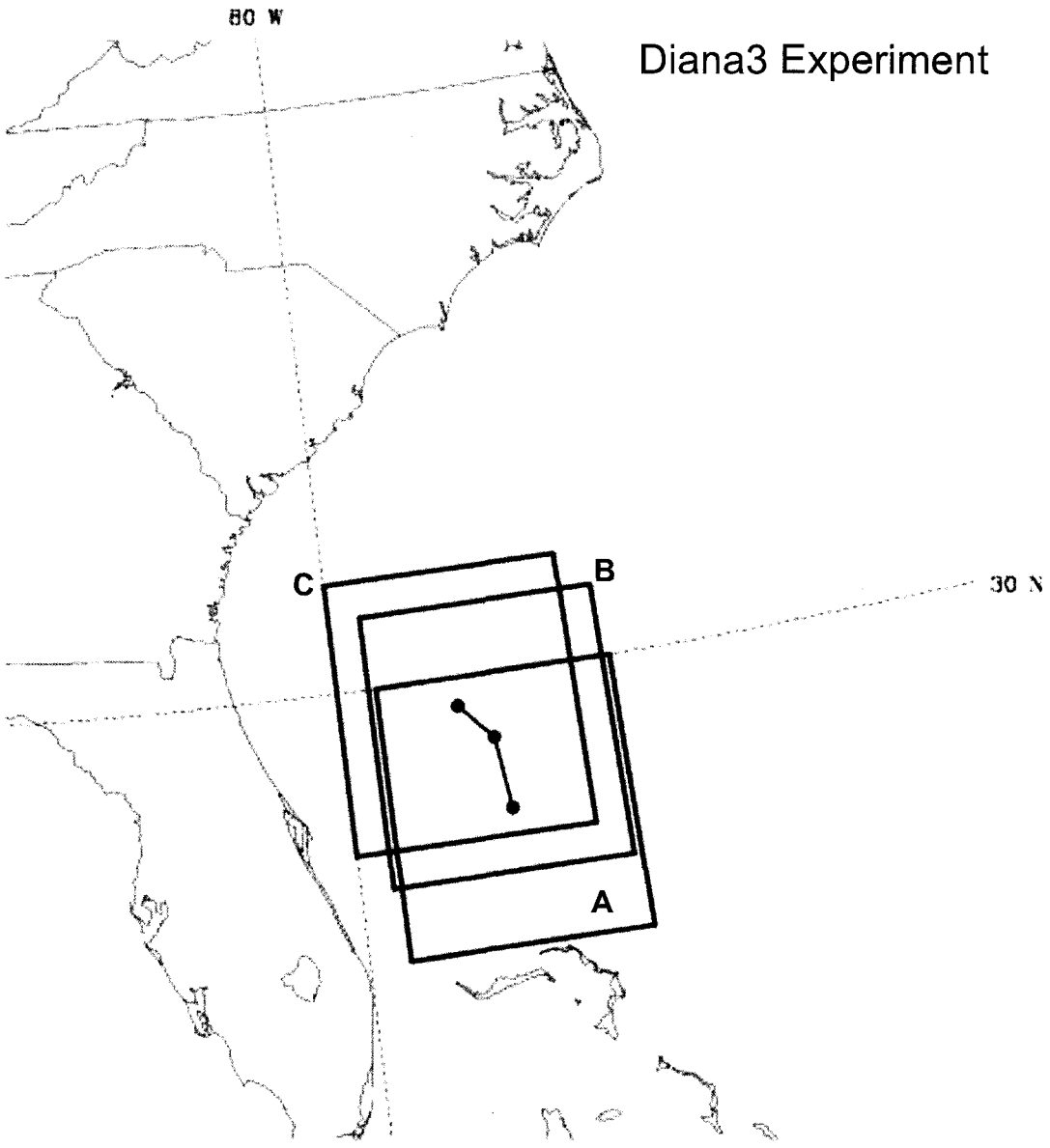

Figure 4.4. Depiction of 3° by 3° box over which area-averaged vorticity was computed relative to the geographic coverage of the 9km grid in the Diana3 simulation. Dots represents the center of Diana's circulation as observed in the Diana3 output data at (A) t = 24h, (B) t = 30h, and (C) t =36h. The location of the box centered on A is fixed for the first 24 hours of the model evolution until a circulation center becomes evident. After t = 24h the center of the averaging box moves with the cyclone center. The boxes centered on the location labeled B and C are snapshots of the moving box at t = 30h and t = 36h, respectively.

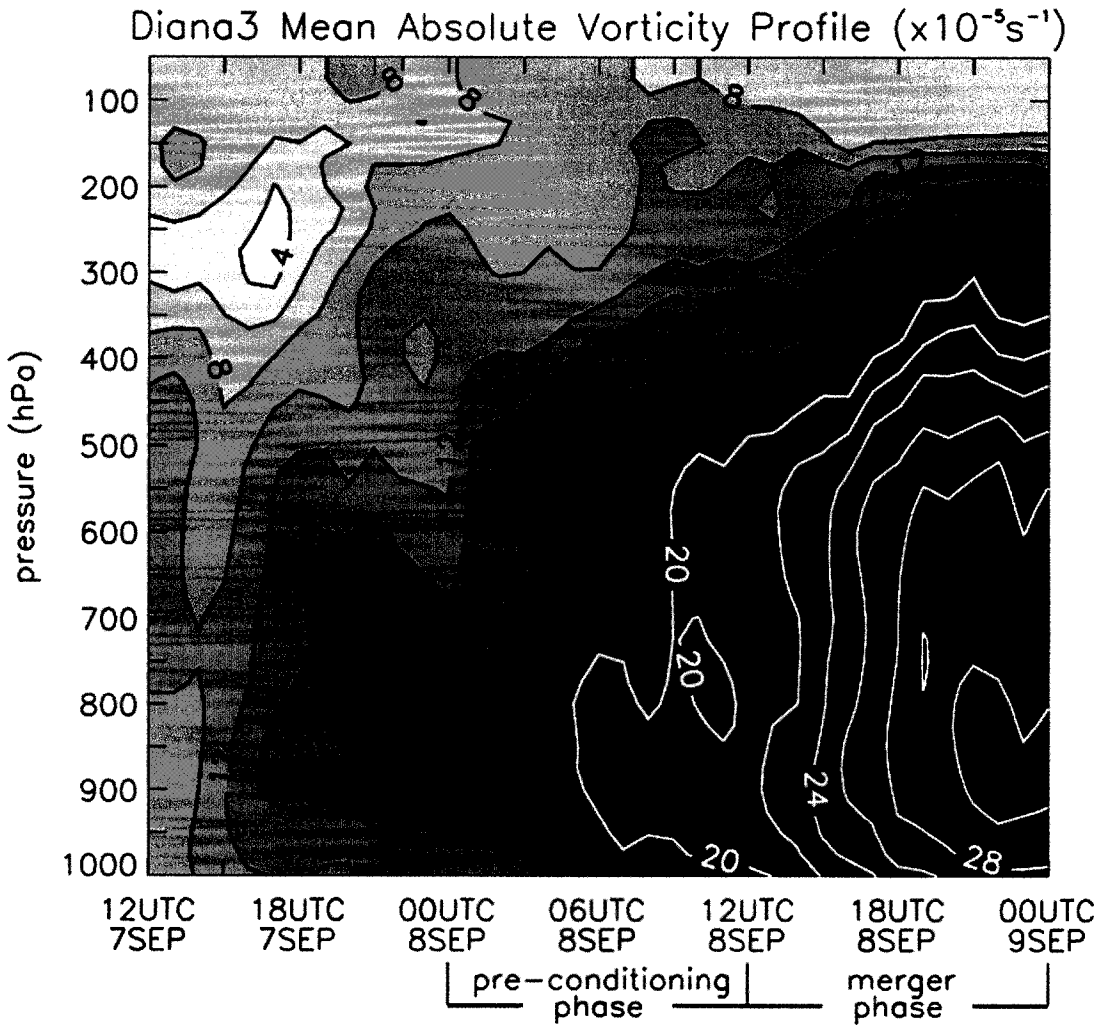

Figure 4.5. Time-height plot of profile of area-averaged vorticity for the 9km grid of the Diana3 simulation. Values plotted are area-averaged absolute vorticity at a given level over the 3° by 3 ° averaging box depicted in Figure 4.4. Contours are every $2.0\times10^{-5}\,s^{-1}$.

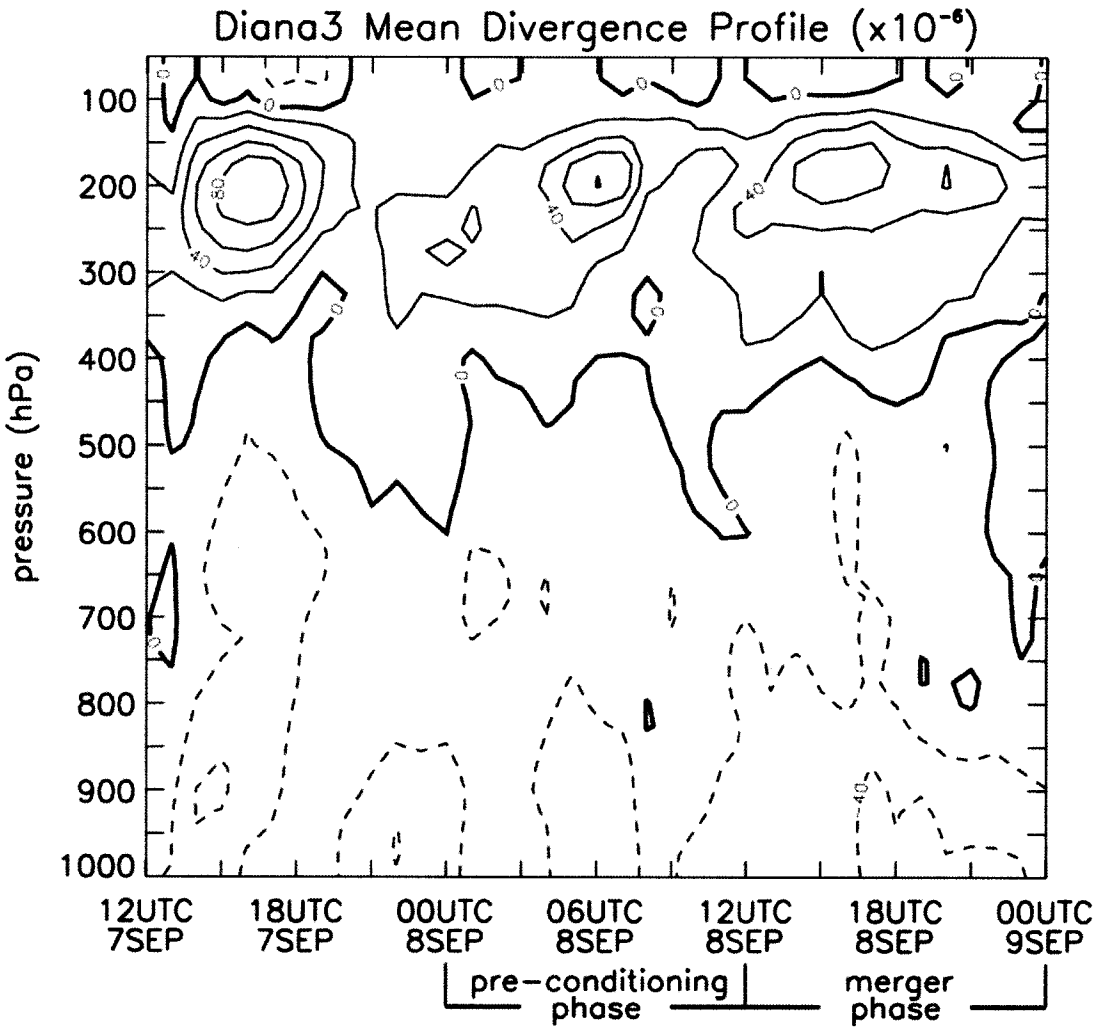

Figure 4.6. Time-height plot of profile of area-averaged divergence for the 9km grid of the Diana3 simulation. Values plotted are area-averaged divergence at a given level over the 3° by 3° averaging box depicted in Figure 4.4. Contours are every $20\times10^{-6}\,s^{-1}$. Negative contours are dashed.

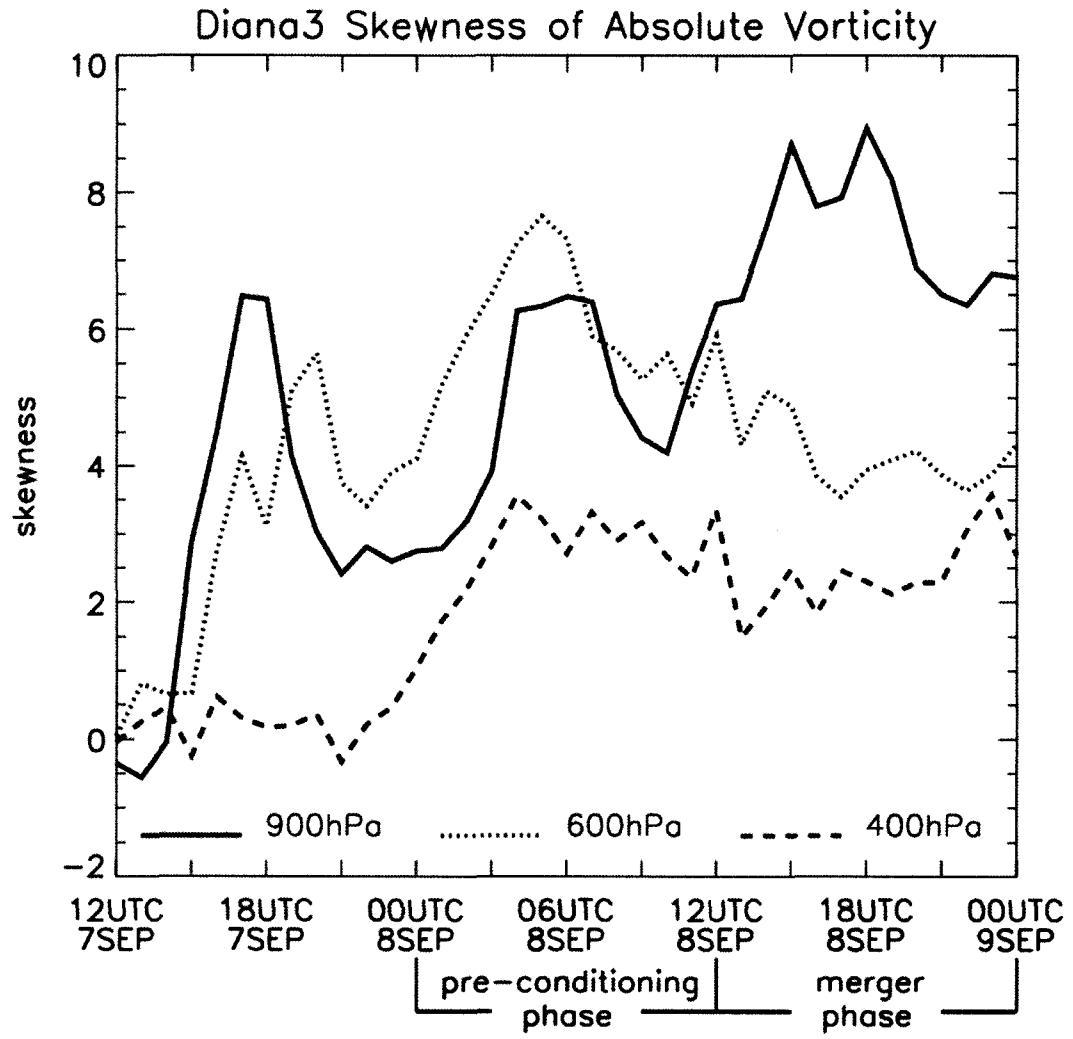

Figure 4.7. Skewness of the absolute vorticity field for entire 9km grid of the Diana3 simulation. Statistics are computed at p = 900hPa, 600hPa and 400hPa pressure surfaces.

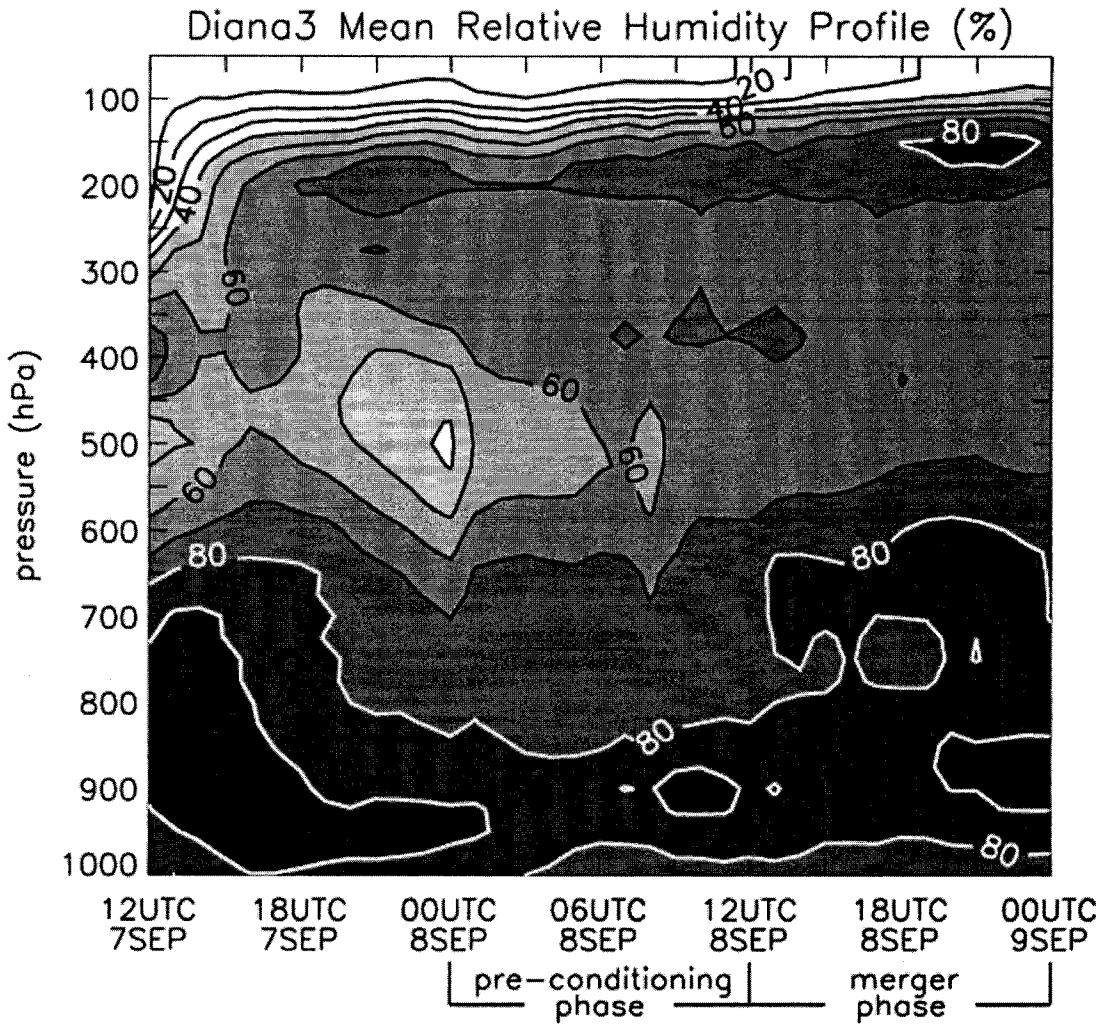

Figure 4.8. Time-height plot of profile of area-averaged relative humidity for the 9km grid of the Diana3 simulation. Values plotted are area-averaged relative humidity at a given level over the 3° by 3° averaging box depicted in Figure 4.4. Contours are every 10% RH. Values greater than 50% are shaded. White contours indicate relative humidity values greater than or equal to 80%.

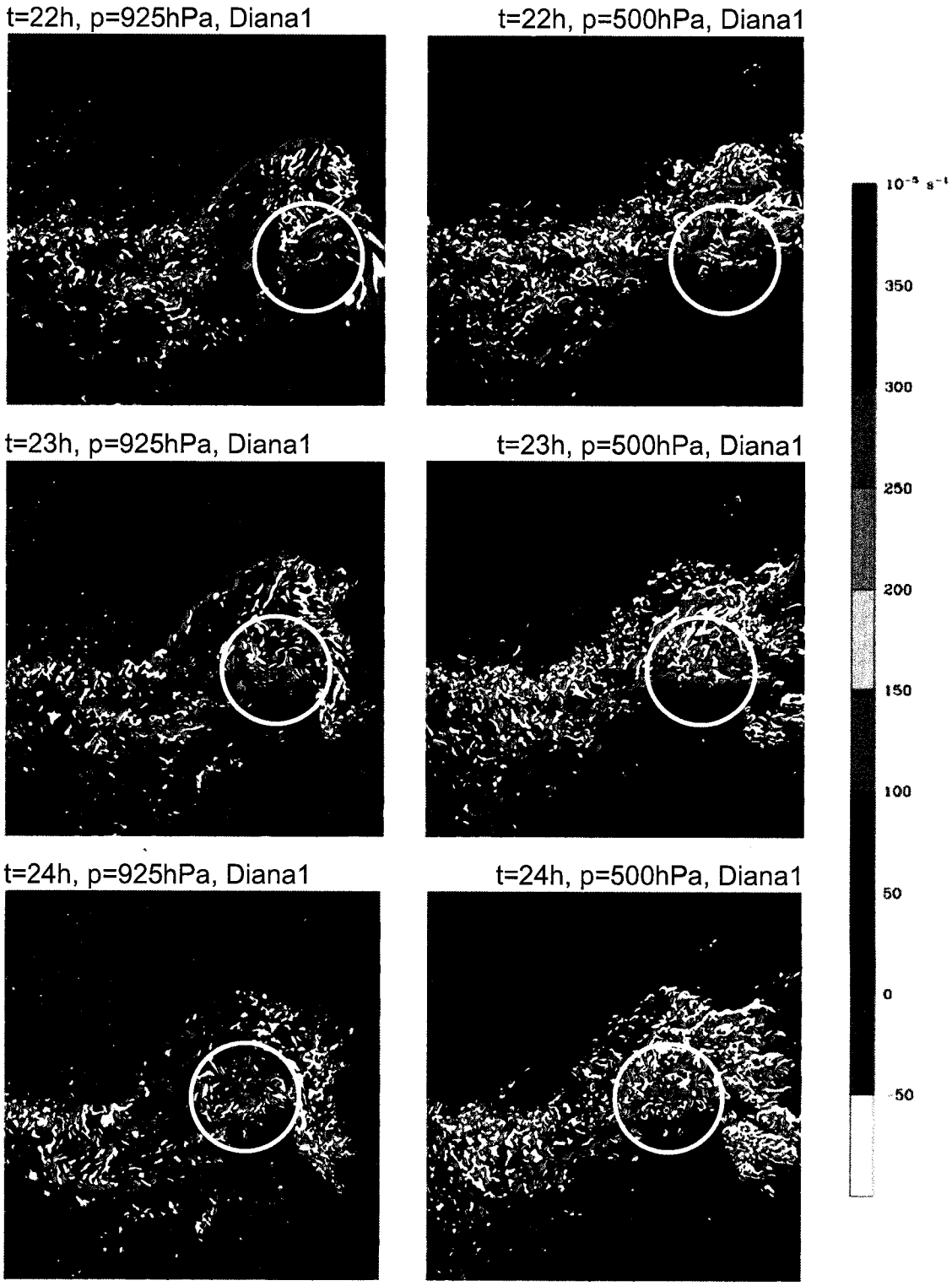

Figure 4.9. Absolute vorticity field at p = 925hPa (left column) and p = 500hPa (right column) during the pre-conditioning phase of development on the 1km grid of the Diana1 simulation. The yellow circle highlights a series of mergers. Shading is approximately the same as in Figure 4.2.

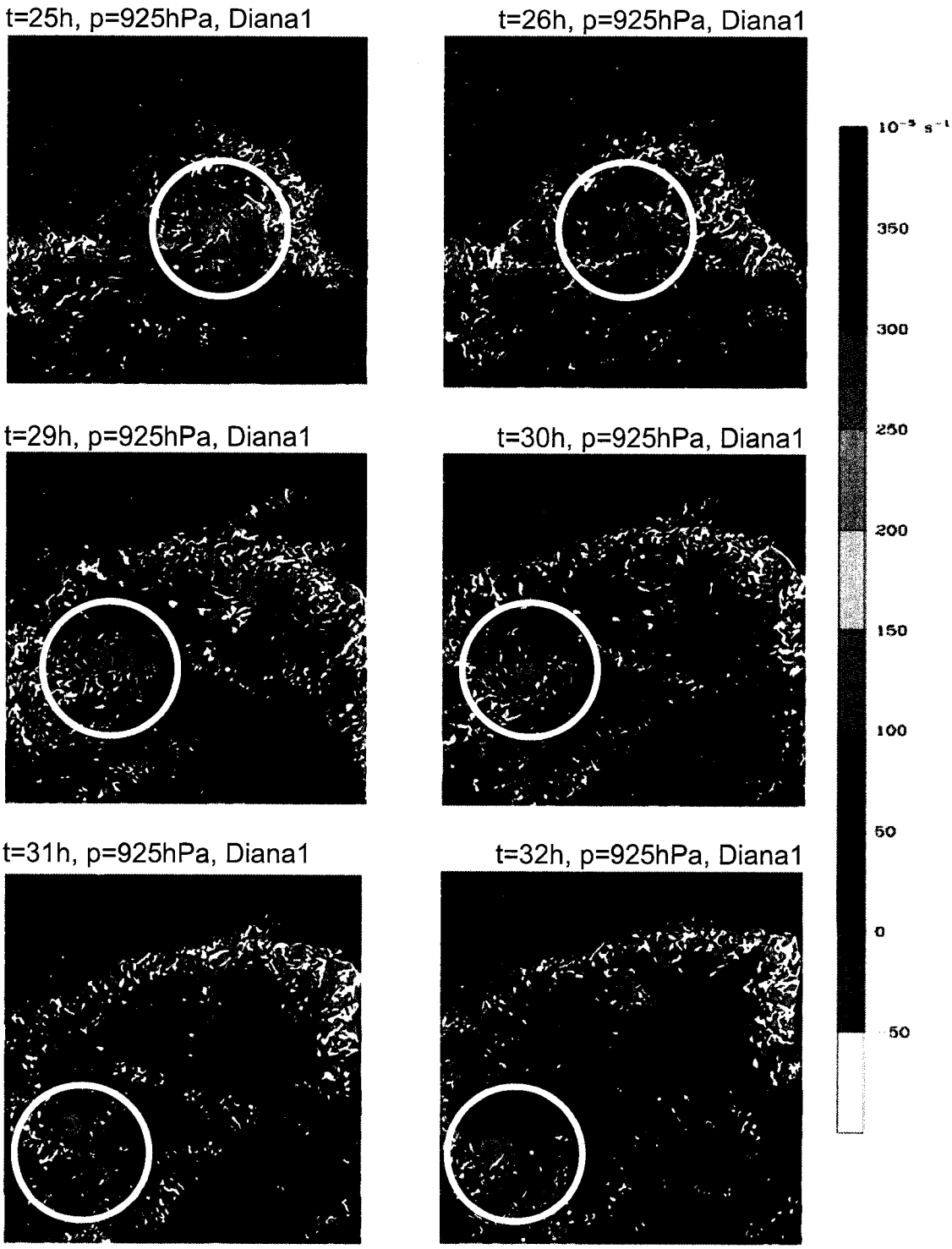

Figure 4.10. Absolute vorticity field at p=925hPa during the merger phase of development on the 1km grid of the Diana1 simulation. Contours are the same as in Figure 4.9.

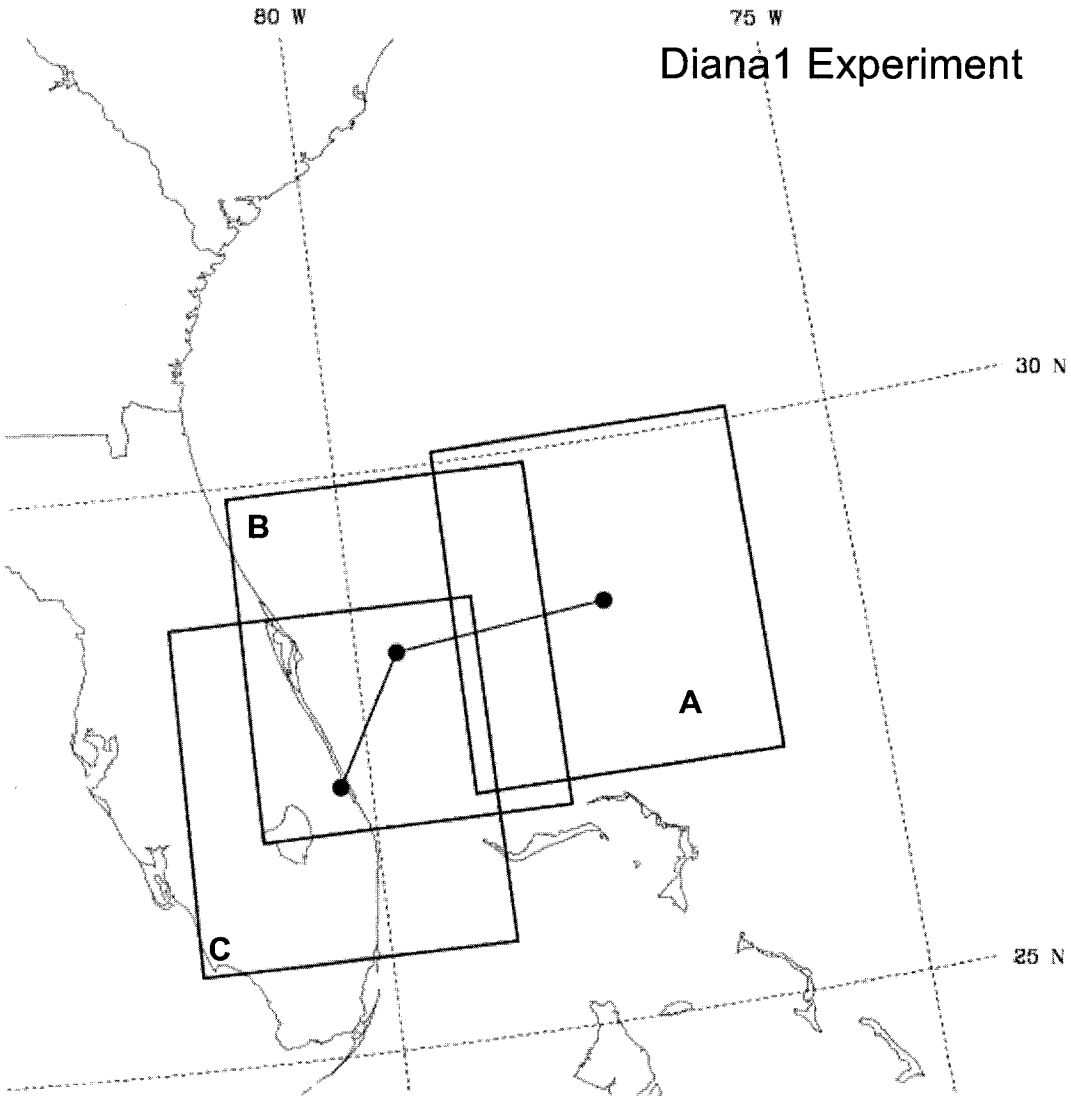

Figure 4.11. Depiction of 3° by 3° box over which area-averaged vorticity and layer averaged relative humidity are computed relative to the geographic covered of our Diana1 3km grid. Dots represent the location of Diana's circulation center as observed in our model output at t = 24h (A), t = 30h (B) and t = 36h (C). The location of the box centered on A is fixed for the first 24 hours of the model evolution until a circulation center becomes evident. After t = 24h the center of the averaging box moves with the cyclone center. The boxes centered on the locations labeled B and C are snapshots of this moving box at t = 30h and t =36h, respectively.

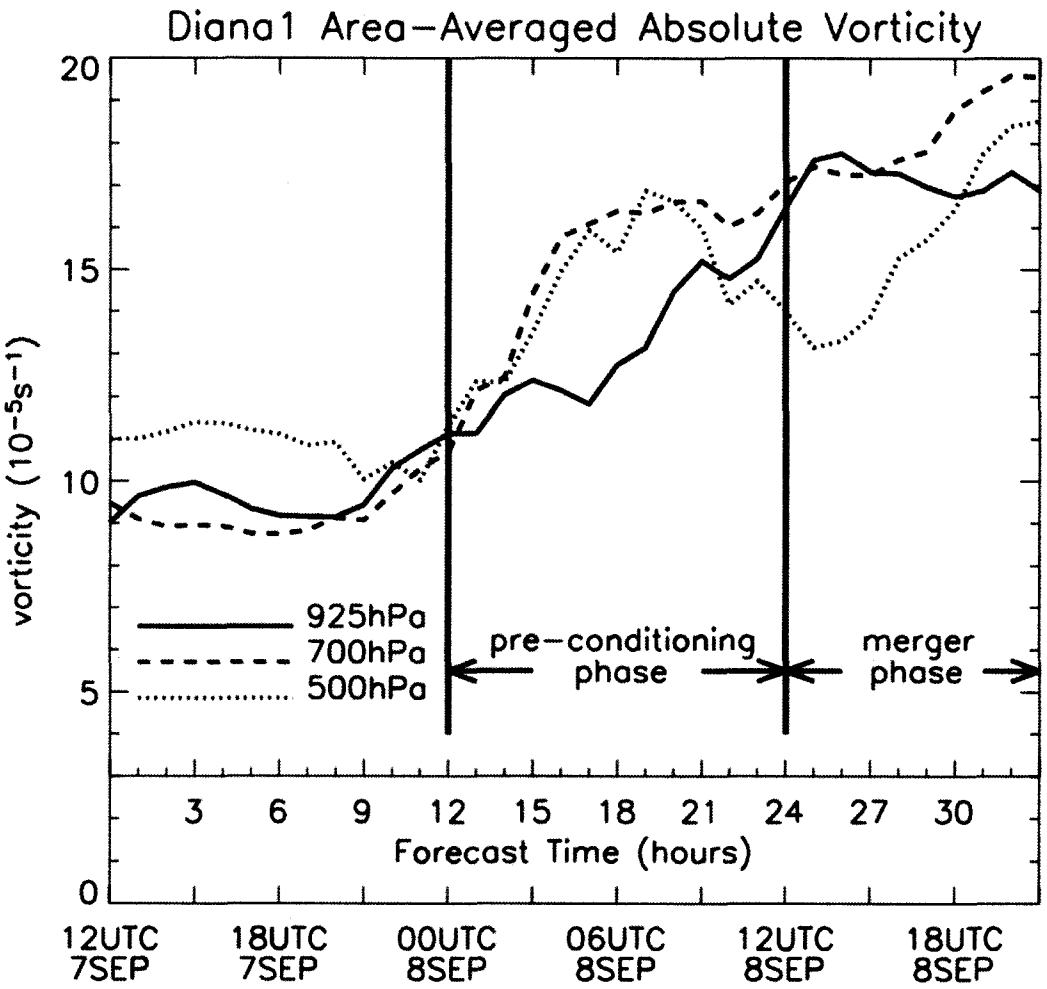

Figure 4.12. Plot of area-averaged low-level absolute vorticity (p = 925hPa, 700hPa, and 500hPa) over a 3° by 3° box located in the genesis area. Calculations are based on output data from our 3km grid of the Diana1 simulation. For the first 24 hours, the box is fixed at the center of circulation that emerges at t = 24h. For each time period thereafter, the center of the box is located at the storm's center and moves with the storm (see Figure 4.11 for the relative size and location of the averaging box).

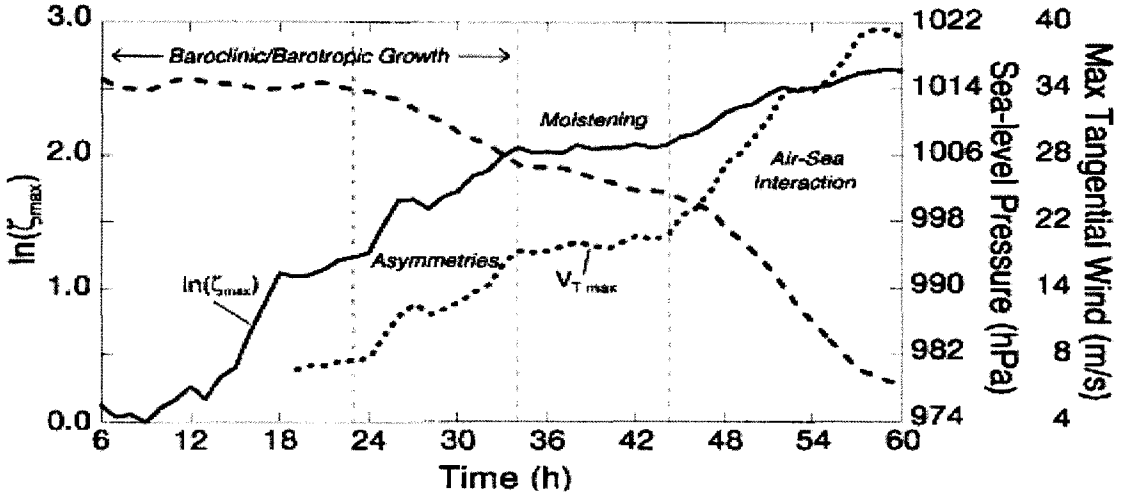

Figure 4.13. Evolution of the natural log of maximum relative vorticity, maximum tangential winds, and minimum sea-level pressure from the DB01 simulation of Hurricane Diana. The relative vorticity is computed in the lowest model level (about 40m AGL), averaged over an 81km by 81km grid box and then scaled by 10^4. The plot shows three phases of development: an initial episode of convective activity until approximately $t = 34$h, an ensuing quiescent phase lasting approximately 10 hours, and a final period of convective activity after approximately $t = 44$h. The model output time indicated on the x-axis is consistent with the time periods in all of our simulations and runs from 18UTC 7 Sep through 00UTC 10 Sep 84 (taken from Figure 12 of Davis and Bosart 2001).

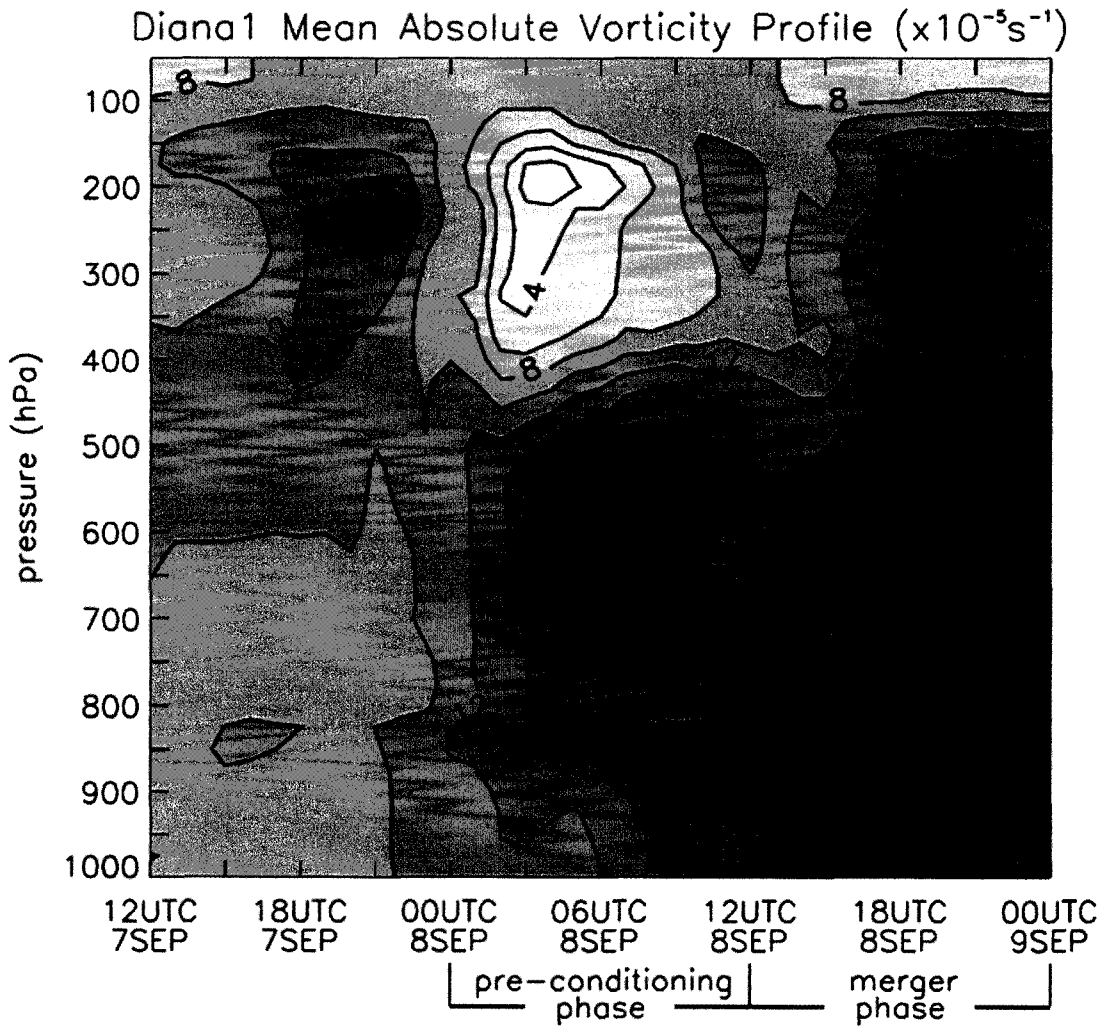

Figure 4.14. Time-height plot of profile of area-averaged vorticity for the 3km grid of the Diana1 simulation. Values plotted are area-averaged absolute vorticity at a given level over the 3° by 3 ° averaging box depicted in Figure 4.11. Contours are every $2.0\times10^{-5}s^{-1}$.

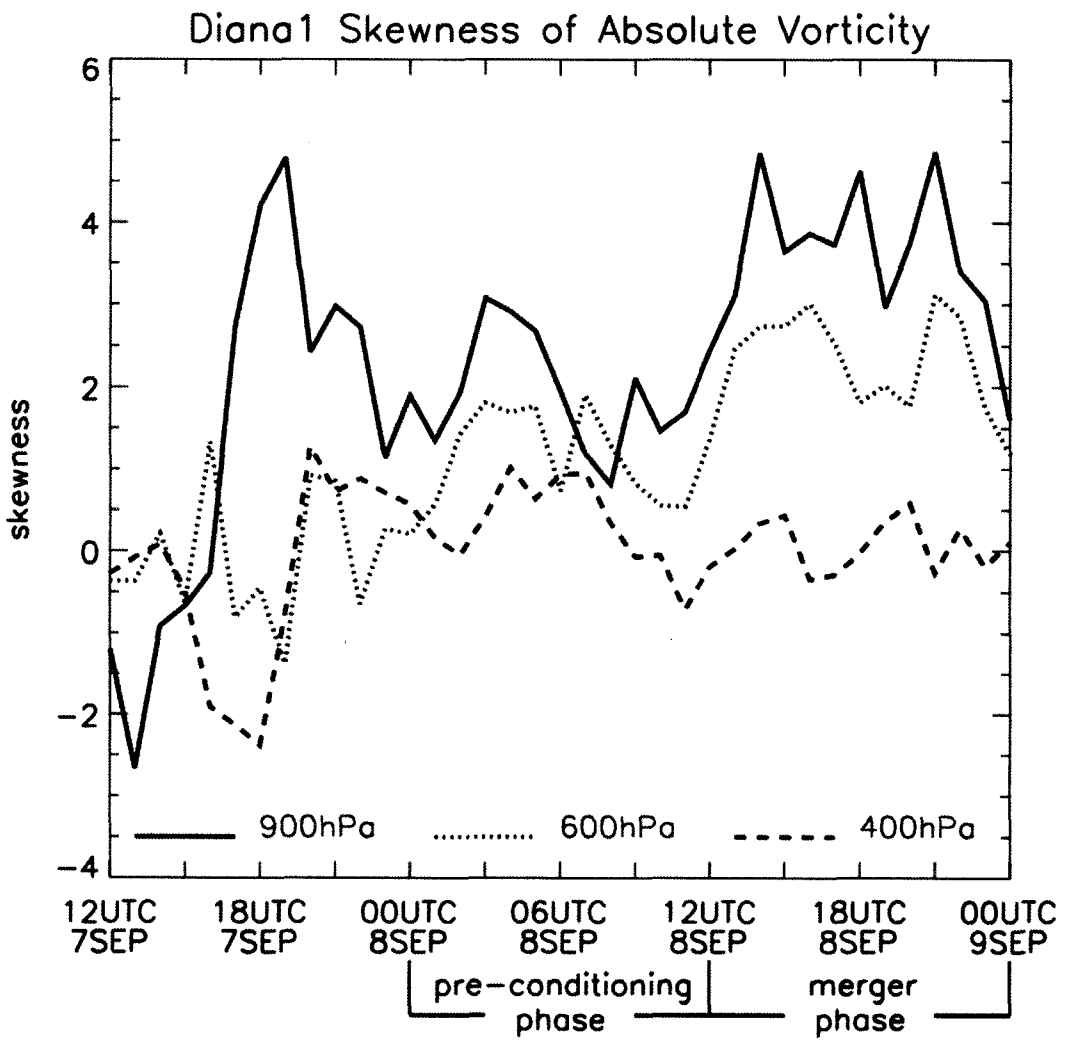

Figure 4.15. Skewness of the absolute vorticity field for entire 3km grid of the Diana1 simulation. Statistics are computed at p = 900hPa, 600hPa and 400hPa. Note the change in the vertical scale compared to Figure 4.7.

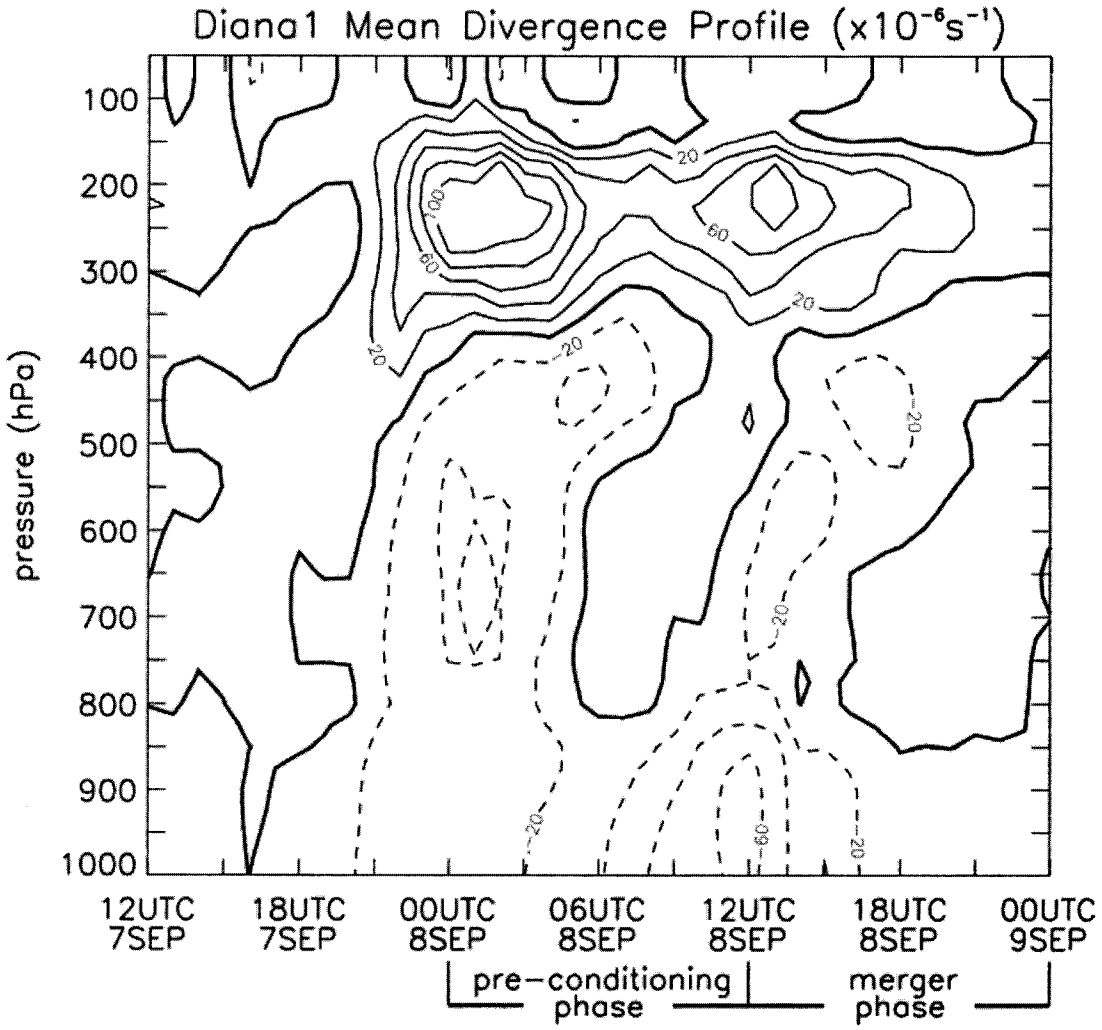

Figure 4.16. Time-height plot of profile of area-averaged divergence for the 3km grid of the Diana1 simulation. Values plotted are area-averaged divergence at a given level over the 3° by 3° degree averaging box depicted in Figure 4.11. Contours are every $20\times10^{-6}s^{-1}$. Negative contours are dashed.

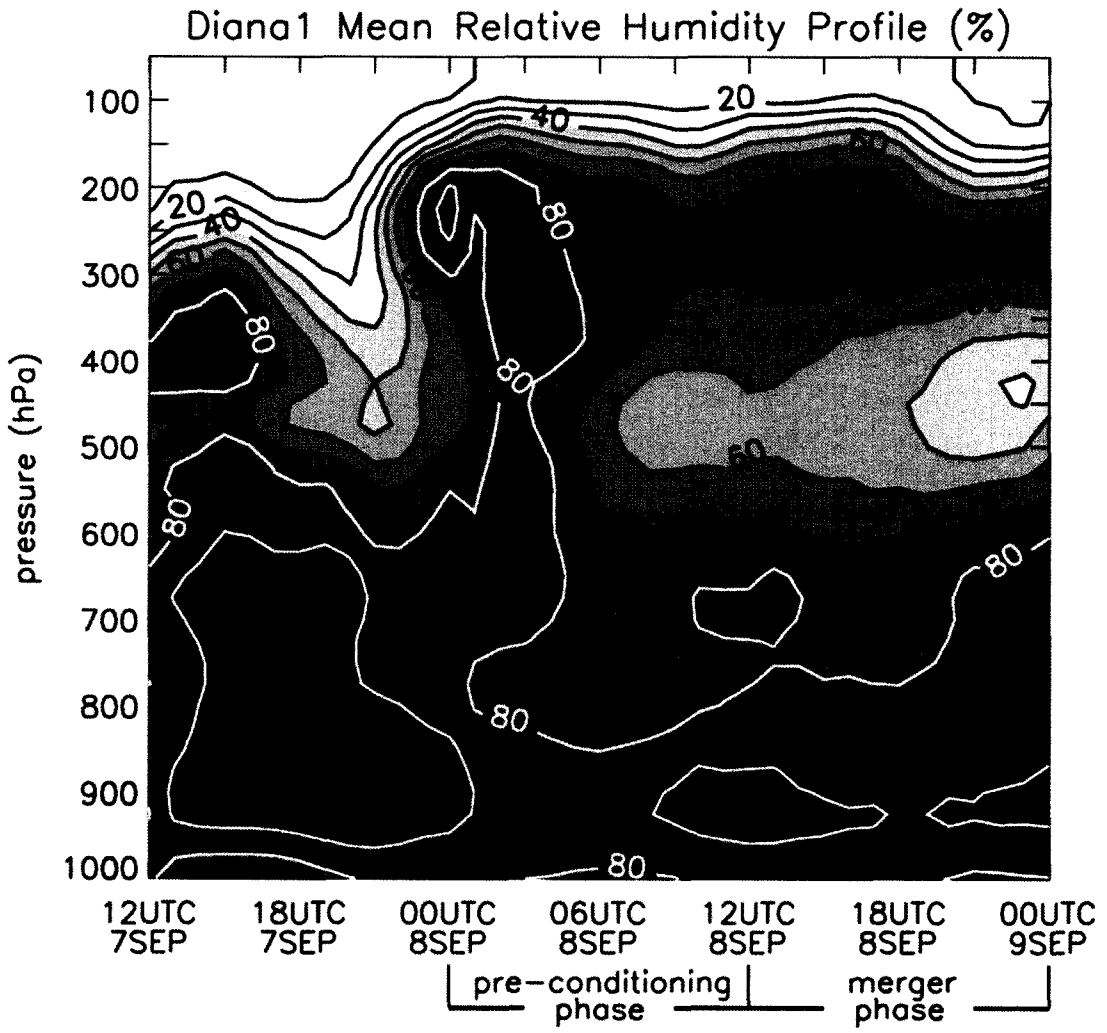

Figure 4.17. Time-height plot of profile of area-averaged relative humidity for the 3km grid of the Diana1 simulation. Values plotted are area-averaged relative humidity at a given level over the 3° by 3° averaging box depicted in Figure 4.11. Contours are every 10% RH. Values greater than 50% are shaded. White contours indicate relative humidity values greater than or equal to 80%.

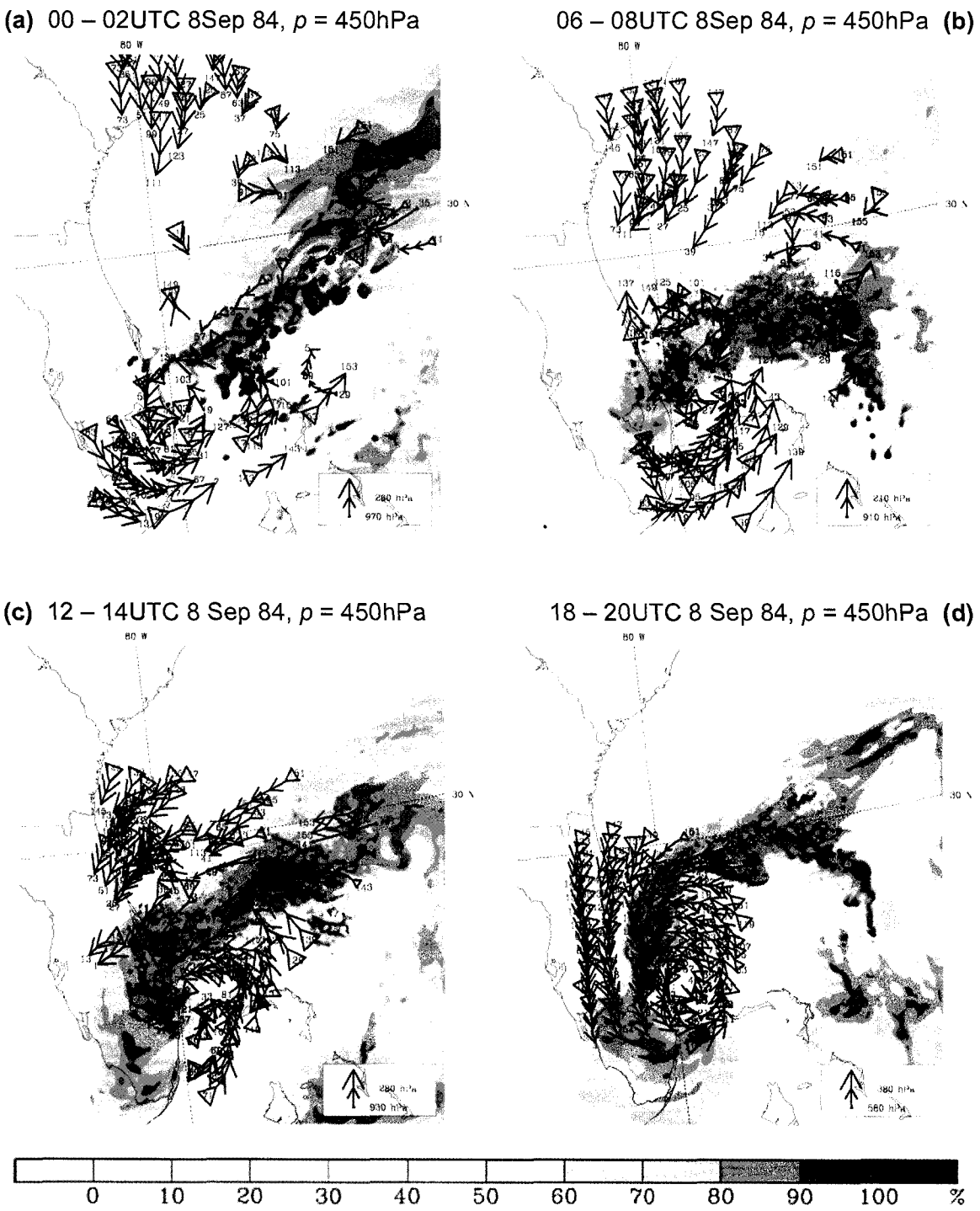

Figure 4.18. Back-trajectory analysis and evolution of relative humidity on the 3km grid in the Diana1 experiment. Relative humidity on the p = 450hPa pressure level is plotted at (a) 00UTC 8 Sep 84 (t = 12h), (b) 06UTC 8 Sep 84 (t = 18h), (c) 12UTC 8 Sep 84 (t = 24h) and (d) 18UTC 8 Sep 84 (t = 30h). Approximately 80 back-trajectories at p = 450hPa were calculated over a 20 hour period from 00UTC 8 Sep 84 – 20UTC 8 Sep 84 (t = 12h to t = 32h). Each panel displays positions of these back-trajectories over a 2 hour period ending at the valid time of the relative humidity field.

Chapter 5

CHARACTERISTICS AND EVOLUTION OF VORTICAL HOT TOWERS

5.1 Introduction

Continuing our progression toward finer scales, we now analyze the convective scale characteristics of the Diana1 simulation. While much of this dissertation so far has focused on documenting the resolution dependence of the VHT route to tropical cyclogenesis, the primary goal of this chapter is to build on previous research and provide a more complete picture of VHT characteristics and the impact of the VHTs on the tropical cyclogenesis process in this high resolution simulation. To be sure, we must still compare our high resolution VHT scale observations to the previous work of H04 and M06. But, the purpose of this comparison will be to gain further insight into the extensive VHT behavior at these finer scales and the impact of the VHTs on the system scale vortex. In the upcoming sections, we focus primarily on data from the 1km grid of our Diana1 simulation. To distinguish scale dependent aspects of the simulation, we compare our results to the 3km results of H04 and the 2km results of M06.

Unlike the rest of this dissertation, the analysis in this chapter is not broken down by developmental phase. That is, we have not segregated our analysis into a pre-

conditioning phase and a merger phase. The reason for this is primarily because, in the course of examining multiple individual VHTs, we found the small-scale characteristics appear largely similar regardless of which phase of development the VHTs emerged. Consequently, we investigate a single, representative VHT that emerged in a time period between the pre-conditioning and merger phases of Diana's development. This vortical hot tower is generally representative of the VHT activity occurring during both phases of development of Hurricane Diana.

5.2 Kinematics

In this section the reader will note that the color contouring in the many of the figures has been modified compared to Chapter 4, particularly for the plots of absolute vorticity. This was done for two reasons: 1) to allow an easier visual identification of the positive and negative vorticity cores and 2) to ensure a more accurate depiction of the relative strength of the negative vorticity anomalies.

5.2.1 Absolute Vorticity Field

In examining the VHT scale characteristics of the model evolution, we first investigate general characteristics of the vorticity anomalies to include typical magnitude and horizontal and vertical distribution of vorticity in the cores. Figure 5.1 depicts low-level absolute vorticity (p = 925hPa) at t = 21h 10min from the 1km grid of the Diana1 simulation. This vorticity field is plotted just prior to the time period of the data in Figure 4.9 and can be used to identify the low-level vortical component of VHT cores. A proxy

for the convective component of the VHTs is presented in Figure 5.2, which shows upward vertical motion at p = 500hPa observed at the same time in this simulation. This pressure level was chosen following the H04 study which indicated maximum updraft velocities in VHT cores were generally observed at a height of z = 5km, and, as such, provides a first order approximation to the location of the *deep* updraft cores. It is evident from this figure that many of the intense cyclonic vorticity anomalies in Figure 5.1 ($\eta \geq 3.0\times10^{-3}\,s^{-1}$) approximately coincide with regions of strong upward vertical motion ($w \geq 3\text{ms}^{-1}$) indicated by the bold contours in Figure 5.2. However, it should be noted that the localized mid-level maxima in the vertical velocity field do not necessarily have a direct correlation to the low-level maxima in the absolute vorticity field since many of the cores are likely tilted because of vertical shear in the environment. Nonetheless, it is broadly true that the regions with strong cyclonic vorticity anomalies also contain strong upward motion cores. This relationship between areas with strong vorticity anomalies and strong vertical velocity cores suggests a connection between the two fields as the M06 theory predicts (and as verified to a certain extent by H04).

Figure 5.3 and Figure 5.4 are close-up views of the low and mid-level absolute vorticity and mid-level vertical velocity fields, respectively, observed at t = 21h 10min in the Diana1 simulation. The relative size and location of the plot window is indicated by the boxes drawn near the bottom of Figure 5.1 and Figure 5.2 (both boxes are identical in size and relative location within the larger domain). This particular plot area was chosen because it contained data representative of the VHT activity occurring throughout the domain at this time and because the individual VHT was isolated from other VHTs, limiting the influence by neighboring structures. Cross-sections through the VHT

complex along the lines indicated in Figure 5.3 and Figure 5.4 highlight the vertical structure of the particular VHT event (both lines are in the same relative position within the domain). The orientation of the cross-section was chosen to intersect both the main updraft core (at mid-levels) and the low-level maximum vorticity anomalies. Both cross-sectional plots are presented in Figure 5.5.

We begin by focusing on the low and mid-level absolute vorticity fields (Figure 5.3). The strength of the maximum low-level positive vorticity anomaly associated with the VHT core is between $3.6\times10^{-3}\,s^{-1}$ and $4.0\times10^{-3}\,s^{-1}$ (compared to $3.0\times10^{-3}\,s^{-1}$ in the H04 simulation) with an ambient value between zero and $4.0\times10^{-4}\,s^{-1}$; this is at least an order of magnitude difference between the anomaly and the background value in the immediate vicinity of the VHT. However, the contouring in Figure 5.3 is not sufficient to determine the magnitude of the background value of absolute vorticity with any degree of certainty. To gain some perspective on the background field, we return to Figure 3.3, a plot of the initial field of low-level absolute vorticity with much finer contour intervals at $\Delta\eta = 7.5\times10^{-5}\,s^{-1}$. From this plot, we see the initial background value of absolute vorticity is in the range $7.5\times10^{-5}\,s^{-1} \le \eta \le 15\times10^{-5}\,s^{-1}$. While this tells us nothing specifically with regard to the snapshot of low-level absolute vorticity in Figure 5.3, it does indicate that the magnitude of the cyclonic vorticity anomaly in question is generally 50 times greater (one to two orders of magnitude larger) than the *initial* low-level absolute vorticity values observed in the genesis region. This finding is consistent among the remaining VHT cyclonic vorticity anomalies and suggests, in general, that the VHT generated cyclonic vorticity cores have central magnitudes 50 times greater than the background vorticity field. Such a distribution of low-level absolute vorticity is broadly

consistent with the results of M06, who showed that the typical magnitude of VHT generated cyclonic vorticity cores was generally one to two orders of magnitude greater than the local background flow.

What is notably different from the two previous studies is the relative strength of the VHT generated negative vorticity anomalies as low levels. In both H04 and M06 the anticyclonic lobe of the typical VHT vorticity dipole is significantly weaker than the corresponding cyclonic lobe (see Figure 4.3 and Figure 5.6 in this dissertation for figures reproduced from H04 and M06, respectively). Data from the H04 and M06 studies suggests that the VHT associated negative vorticity anomalies have absolute magnitudes generally one-third of the magnitude of their corresponding positive anomalies ($\sim -1.0\times10^{-3}\,s^{-1}$ compared to $\sim 3.0\times10^{-3}\,s^{-1}$). However, data from our high resolution Diana1 simulation suggests a different distribution of vorticity. Figure 5.3b shows that the low-level anticyclonic vorticity core associated with our isolated VHT has a magnitude of approximately $-3.0\times10^{-3}\,s^{-1}$, generally 70% to 80% of the magnitude of the cyclonic anomaly (3.6 to $4.0\times10^{-3}\,s^{-1}$), much stronger than previous VHT studies suggested. This becomes even more evident when one examines the cross-section through this vorticity couplet (Figure 5.5)[7]. The cross-section provides further evidence that the cyclonic and anticyclonic lobes have similar strengths, and it shows that the lobes of the vorticity dipole have comparable magnitudes at more than just the lowest model layer.

[7] While these results are dependent upon the orientation of the cross section, we examined several cross sections through this particular VHT complex, and many others, and found the above mentioned results to vary only slightly with regard to orientation of the cross section.

The cross section also displays an additional feature first suggested and observed in the M06 study, the change in polarity of the vorticity dipole with height. The vertical structure of the VHT generated vorticity couplet is such that, at upper-levels, an anticyclonic anomaly overlies the near surface positive vorticity core and a strong cyclonic anomaly (also at upper-levels) overlies the negative vorticity lobe of the near surface dipole. As suggested by M06, this feature is the result of opposite signed MCV-generated horizontal vorticity tubes (above and below the MCV) being tilted into the vertical and subsequently stretched by the deep convection (illustrated in Figure 10 of M06). What is different in our simulation compared to the M06 results, however, is not the existence of the opposite phase dipoles at lower/upper-levels but, rather, the relative strength of the individual anomalies at upper-levels. In the Diana1 experiment the upper-level ($z \approx 6$km) anticyclonic anomaly appears larger in size and nearly equal in magnitude relative to the upper-level cyclonic anomaly (the strength of the positive anomaly at $z \approx$ 6km is approximately $\eta = 3.2\times10^{-3}\,\mathrm{s}^{-1}$ while the negative anomaly has a value near $\eta = -3.2\times10^{-3}\,\mathrm{s}^{-1}$). Such a feature was not observed in the M06 simulation, or the H04 simulation for that matter. In both previous studies, the magnitude of the anticyclonic lobes was weaker by a factor of 2 to 3 with horizontal scales comparable to the cyclonic lobes. This was particularly true in the idealized study of M06 who explicitly noted this difference in the cyclonic and anticyclonic lobes of the vorticity dipoles observed in the simulation (see Figure 5.6).

5.2.2 Vertical Velocity Field

We now turn our attention to the characteristics of the vertical velocity field

associated with the emerging VHTs. Figure 5.2 is a plot of the mid-level vertical velocity field (p = 500hPa) on the 1km grid at t = 21hr 10min. As mentioned above, this pressure level was chosen because the H04 modeling study indicated the maximum upward vertical velocity observed in VHTs was generally in the middle troposphere near z = 5km altitude. Here we have chosen a standard pressure level of p = 500hPa to illustrate typical vertical velocity data. In Figure 5.2 we observe approximately 100 deep convective cores present in the domain. As was done in Section 5.2.1, let us focus on just one representative updraft core.

Figure 5.4 is a close-up view of the mid-level vertical velocity field in the vicinity of the vorticity core examined previously. To ensure consistency with the above data and analysis, this plot has the same geographic coverage and is plotted at the same output time as Figure 5.3. Also plotted in Figure 5.5b is a vertical velocity cross section through the center of the updraft along the northwest-southeast oriented line drawn in Figure 5.3 and Figure 5.4. Contour levels in both plots are ± 1, 2, 3, 4, 8, and 16ms^{-1}, with the bold contour demarcating the 3ms^{-1} updraft region. This is consistent with the analysis of H04 who used a vertical velocity of 3ms^{-1} as the threshold upward motion value for defining an updraft core. Negative contours in each plot are dashed. Both plots (Figure 5.4 and Figure 5.5b) indicate a VHT convective updraft core having a maximum horizontal width of approximately 6km based on the width of the 3ms^{-1} contour. The width of the updraft is largest at lower levels (near z = 4km) and decreases with height through the model atmosphere with a plume-like appearance. The height of the convective core is near z = 12km as defined by the 3ms^{-1} contour. Additionally, the maximum updraft velocity in the center of the core (the heavy black dot along the cross-section in Figure 5.4) is

approximately 17ms^{-1} at approximately 10km altitude (see Figure 5.7). The shape of the vertical velocity profile in the updraft core (Figure 5.7) is similar to the shape of climatological latent heating profiles associated with strongly stratiform precipitation created by Schumacher et al. (2004, hereafter S04) from radar observed Tropical Rainfall Measuring Mission precipitation. In particular, Figure 3 of S04 shows a latent heating profile based on a linear combination of 70% stratiform and 30% convective rain fractions. The result is a latent heating profile that closely resembles the vertical motion profile in our example VHT. While this *might* suggest this particular VHT is associated with stratiform precipitation, we believe this strengthens our argument that the area-averaged divergence in Section 4.4.4 is, at times, a superposition of convective and stratiform precipitation modes. The noteworthy convergence below p = 800hPa in the area-averaged divergence profile at t = 09 UTC 8 Sep (Figure 4.16) indicates that low level convection is a significant mode of precipitation at this time in the simulation, in an area averaged sense. Our example VHT likely has a significant convective component as well.

These results, specifically the size and strength of our example updraft core, are consistent with the analysis of M06 whose 2km simulation produced VHTs with diameters ranging from 5 to 20km and instantaneous maximum vertical velocities between 20 and 35ms^{-1} at altitudes between 9 and 12km. The strength of the updraft in this VHT is also consistent with the 3km results of H04 results in which the observed maximum vertical velocities were approximately 15ms^{-1} near z = 6km altitude. However, the width of updraft in our example VHT is smaller than the typical VHT observed in H04. The H04 simulation produced updraft cores typically 10km in diameter, nearly

66% larger than our example VHT. This is not unexpected given that our Diana1 experiment contained nearly an order of magnitude increase in the number of gridpoints for a given area relative to the H04 simulation.

5.2.3 CFAD Analysis

It must be noted that the analysis presented above is for a single updraft core and is not necessarily consistent across the board with all of our simulated VHTs. To help quantify the structure of the vertical velocity field for the entire population of convective updrafts, we utilize a statistical tool known as a contoured frequency by altitude diagram (CFAD) first introduced by Yuter and Houze (1995). CFAD plots allow us to present a contoured two-dimensional view of the vertical velocities in the simulation and provide critical information about the distribution of updraft and downdraft velocities. Each grid point observation of upward motion is placed into an appropriate bin of width $0.5ms^{-1}$. That is, we analyze the entire field of w at a given output time in our simulation and count the number of observation that fall within a certain range (e.g., $0.5ms^{-1}$ to $1.0ms^{-1}$, $1.0ms^{-1}$ to $1.5ms^{-1}$, $1.5ms^{-1}$ to $2.0ms^{-1}$, and so on). Once this binning algorithm is complete at all horizontal and vertical gridpoints, we count the total number of observations and determine a frequency of occurrence for each range (or bin) of values. The resultant frequencies can then be plotted two-dimensionally with the bin values on the x-axis and an appropriate height coordinate on the y-axis to give us a view of the "spread" of the observed vertical velocities at a given output time.

In our particular case we further constrained the CFAD calculations to be performed over a 3° by 3° box centered over the emerging tropical cyclone. This was the same

averaging box used in Chapter 4 to compute area-averaged absolute vorticity, divergence, and relative humidity profiles for the Diana1 simulation (see Figure 4.11). The results of this analysis method are presented in Figure 5.8 at various output times during the model evolution on our 1km grid. Aside from the fact that approximately 90% of all the observed vertical velocity values during any observation period fall in the range $-3\text{ms}^{-1} \leq w \leq 3\text{ms}^{-1}$, Figure 5.8 shows that the field of vertical velocity within 1.5° of the emerging cyclone center is strongly skewed toward positive values (consistent with the skewness plots in Figure 4.15). Furthermore, this distribution shows that the strongest of the convective updraft cores have vertical velocities that fall in the 15ms^{-1} to 30ms^{-1} range. These values are much stronger than what was observed by Jorgensen et al. (1985, hereafter J85) in their observational study of vertical motion in mature hurricanes (they observed maximum vertical motions generally between 5ms^{-1} and 10 ms^{-1}). Our maximum updrafts are on the order of 30ms^{-1} at approximately p=300hPa, while J85 observed maximum values of only 17ms^{-1} at approximately p=500hPa. The reasons for this apparent discrepancy are varied, but it is likely that the data in our simulation is at a much greater resolution that the aircraft data cited in J85. Additionally, we observe the strongest vertical velocities during the genesis phase rather than during Diana's mature/intensifying phase. The J85 study focused exclusively on mature storms and was not able to observe updrafts during genesis. Finally, their flight data only covered altitudes up to approximately z=6km while our maximum vertical motion is observed roughly between 7km< z <10km. Thus, it is possible the storms in the J85 study may have had updrafts stronger than 17ms^{-1} either earlier in their evolution, at higher altitudes or on spatial scales that were not fully resolved by the aircraft instruments.

Recall that our 1km grid consists of roughly 500 by 500 horizontal gridpoints with 36 vertical levels; this covers a geographical area of approximately 5° by 5° in terms of latitude and longitude. Our CFAD analysis technique covers a 3° by 3° box giving us approximately 3.2 million total grid point values sampled. Thus, the smallest contour interval (0.001% - 0.01%, the purple shading), which generally includes values of w between $15ms^{-1}$ to $30ms^{-1}$ in Figure 5.8, contains as many as 300 grid point observations of vertical velocity greater than $15ms^{-1}$. If we assume a threshold value of $15ms^{-1}$ is indicative of deep convection associated with VHT activity, this observation corresponds approximately well with our estimate of nearly 100 updraft cores visible in Figure 5.2. Thus, it is likely, based on the general correspondence between our analysis of Figure 5.5b and Figure 5.8, that the maximum updraft velocity in many of our VHT cores is within the range $15ms^{-1} \leq w \leq 30ms^{-1}$. This is consistent with what was observed in the M06 study and slightly stronger than the typical maximum updraft velocity observed in the H04 study. Further analysis of Figure 5.8 suggests that the maximum velocities in our updraft cores are observed at mid to upper-levels of the atmosphere, generally between $p = 400hPa$ and $p = 250hPa$ (roughly $7km \leq z \leq 10km$). This is also generally consistent with the M06 and H04 studies (see H04, Section 3a., and M06, Section 5a), though the typical altitude of the maximum VHT updraft in the H04 study was on the lower end of the range at approximately $z = 7km$. As a consistency test of the CFAD analysis, we also interrogated approximately 20 separate convective cores in our Diana1 simulation at various times during the pre-conditioning and merger phases. In general, we found the maximum width of the $3ms^{-1}$ contour was in the 6-10km range with maximum vertical velocities approximately $16\text{-}25ms^{-1}$ at altitudes between 8 and 10km.

It is worth noting that the highest observed value was approximately $40ms^{-1}$ near an altitude of 10km, which is somewhat larger than the maximum instantaneous updraft velocities observed in either of the previous two VHT studies. It is also worth noting that updrafts greater than $20ms^{-1}$ are not uncommon in our simulation, especially early in the pre-conditioning phase when the convection was strongest and deepest (see Figure 5.8a).

Figure 5.8 also gives us valuable information regarding how this vertical velocity distribution changes over the course of the simulation. From this plot sequence, we see that the maximum updraft velocities are always greater in magnitude than the downdrafts. This is evidenced by the strong bias in the data toward positive values and by the relative location of the contours for the highest observation frequencies. Additionally, the contours nearest zero (i.e., the yellow, orange and red contours) are biased toward negative values implying that there is a much larger proportion of weak vertical velocities that correspond to downdrafts than those that correspond to updrafts. What is more interesting is the evolution of the CFAD plots over the course of the simulation. Figure 5.8 clearly shows that strength of the entire vertical velocity field (updrafts and downdrafts) weakens over the course of our Diana1 numerical experiment. During pre-conditioning phase (t = 12h to t = 24h), the vertical motion field is rather robust with maximum values of w between $25ms^{-1}$ and $35ms^{-1}$ at approximately the p = 400hPa pressure. As the simulation progresses and a central vortex emerges, the vertical velocity field weakens across the board as both the updraft and downdraft cores become significantly tempered. Maximum vertical velocities at the end of the simulation (t = 36h) are between $10ms^{-1}$ and $15ms^{-1}$. Additionally, the level of maximum upward motion by t = 36h has fallen to approximately the p = 500hPa pressure level. These two

observations combined suggest the genesis region contains a greater number of convective cores that are deeper in the early parts of the simulation (i.e. toward the beginning of the pre-conditioning phase) than later in the simulation. Particularly, analysis of Figure 5.8 shows that the convective activity during pre-conditioning (t = 12h to t = 24h) is stronger and more widespread than during the merger phase (t = 24h to t = 36h) in the Diana1 simulation. Since our averaging box follows the emerging storm center, this is consistent with our observations of the merger phase in Chapter 4 which suggest the developing vortex becomes strong enough to shear nearby vorticity anomalies and subsume in the core forming a "moat" around the storm center generally devoid of strong updrafts/downdrafts (cf. Rozoff et al. 2006).

5.2.4 Analysis of Environmental Shear

The question then becomes, why the difference in the basic structure of our VHTs compared to VHTs in previous studies, specifically with regard the intensity of the updraft cores. Aside from more subtle differences that result from our simulation being based on environmental data, the major distinction between our simulation and the M06 simulation is that fact that we have significant environmental vertical shear. The M06 simulation was initialized with a MCV-like vortex maximized at 4km altitude. While this resulted in vertical shear above and below the MCV, there was no deep environmental shear on geographic scales larger than the initial MCV. The maximum tangential wind speed in M06 MCV was initially 6.6ms^{-1} with approximately 3.5ms^{-1} surface winds. Thus, the maximum shear value realized from the surface to z = 4km was approximately 3ms^{-1}, was axisymmetric in nature and was located at the radius of the MCV maximum

winds (r = 70km). By contrast, the environmental conditions in our Diana1 simulation indicate much larger shear values that extend through a greater depth of the atmosphere due largely to the presence of a significant mid/upper-level trough in our initial conditions. Initial shear values over the genesis region in the Diana1 simulation were approximately 12ms^{-1} over a depth of 9km (see Figure 5.9), though the shear was weaker over the Florida peninsula (8ms^{-1} over 9km depth) than northeast of the Bahamas (20ms^{-1} over 9km depth).

The impact of larger shear on the vertical motion field in the Diana1 simulation is likely adversely affecting the evolution of the storm. This is well documented in the literature as many studies have shown that strong vertical shear over a tropical cyclone (i.e. ≥12ms^{-1} generally between the 850hPa and 200hPa pressure levels) can stunt the genesis process and weaken the intensification of mature storms (i.e. Zehr 1992; Gray 1968; DeMaria 1996; Frank and Ritchie 2001). In our high resolution Diana1 simulation, the environmental shear over the genesis region is generally greater than the 12ms^{-1} threshold suggesting that we should see generally suppressed convective activity and a weaker storm evolution (this is shown to a certain degree in Chapter 4 in which we show that the storm simulation in Diana3 was more intense that the storm in the Diana1 simulation).

5.2.5 Effect of Environmental Shear on Storm Evolution

One of the most intriguing aspects of the Diana1 simulation is the fact that genesis was able to occur despite the significant environmental shear and its expected adverse affect on the vertical motion field. To better understand how genesis was able to come

about, we examine the evolution of the convective cores in conjunction with the evolution of shear magnitudes in the Diana1 simulation. Figure 5.9 is a plot of vertical shear magnitude (surface to z = 9km) observed on the 3km grid of our numerical simulation at various output times. Overlaid each of the plots in this figure is the w = 3ms^{-1} contour of vertical velocity at p = 500hPa. As was done previously in this dissertation, we use w = 3ms^{-1} contour as an approximate indicator of where VHTs are likely developing. Figure 5.9a indicates the magnitude of shear initially over the genesis area was generally in the range from 8ms^{-1} to 20ms^{-1} with the strongest shear values observed on the eastern side of the domain just north of the Bahamas. The first convective bursts in the genesis area are initiated in the vicinity of the higher shear values and are generally located under the "shear ridge" on the eastern side of the domain (see also Figure 3.11). As the convection develops, it erodes away the shear causing it to become significantly reduced (Montgomery and Farrell 1993, Davis and Bosart 2003). As evidenced by the vertical velocity contours, the deep convection that emerges is generally co-located within regions of reduced shear values (4ms^{-1} of less). Considering that the initial shear in the convecting region was as high as 20ms^{-1}, the co-location of the updraft cores and the area of reduced shear suggest that the convection is playing an important role in annihilating the shear. As the vertical shear is reduced, more convective activity takes place which tends to reduce the shear even further. This suggests a positive feedback mechanism whereby the action of the deep convection moderates the shear over a small area allowing more deep convection which reduces shear values over an even larger area allowing more widespread convective activity, and so on. The end result is a fairly large area of reduced shear values (i.e., Figure 5.9d) over which further convective

activity is not significantly limited by the shear and which is more favorable to tropical storm formation. It is also interesting to note that the most intense convective regions are generally located where the strongest shear gradients exist, albeit on the down-gradient side within regions of generally reduced shear. This characteristic of the convection is most easily observed in Figure 5.9b in which almost all of the white contours are oriented along two lines. The convective cores along the more southeasterly line are nearly all in areas of relatively weak shear (lighter gray areas) in the immediate vicinity of "pockets" of high shear values (the dark-gray areas). This further suggests that the convective activity is acting to reduce the shear values.

5.3 Thermodynamics

Thus far we have focused on the kinematic structure of the towers and their local and system scale effects in the genesis of Hurricane Diana. In this section, we examine certain thermodynamic aspects of the VHTs, and, more specifically, the structure and evolution of the moisture field within our example VHT. Figure 5.11 is a cross section of the relative humidity field at t = 21h 10min along the same line as previous cross-sections discussed in this chapter (see Figure 5.3 and Figure 5.4 for the orientation of the cross). Comparing Figure 5.11 and Figure 5.5b, we find that the largest increase of moisture in the column is in the core of the updraft. This is the direct result of the vertical motion transporting moisture upward from the surface. The fact that this updraft core is able to resist the adverse affects of the environmental shear is likely due to the strong rotational component in the core. Consistent with the results of Reasor et al. (2004), the anomalously high vorticity in the VHT likely stiffens the updraft and helps it to act like a

containment vessel allowing for nearly undilute ascent through the top of the model atmosphere. This acts to limit dry entrainment and allows significant moistening of the column by the VHT.

The tendency to moisten the atmospheric column is further evidenced by examining the vertical sounding in the core of the VHT. Figure 5.12 is a plot of Skew-T/Log P diagrams computed in the center of the updraft (at the location of the black dot in Figure 5.4). To show the evolution of the moisture variables over the typical lifespan of a VHT, the thermodynamic diagrams in Figure 5.12 are calculated 77min apart (Figure 5.12a is valid at t = 20h, and Figure 5.12b is valid at t = 21h 10min). The sounding in Figure 5.12a shows environmental conditions just prior to the onset of deep convection. This figure indicates the existence of a moist layer from the surface to approximately p = 900hPa (dew point depression less than 2°C) underneath a saturated layer between p = 900hPa and p = 700hPa. Above this saturated layer, the atmosphere dries slightly while maintaining a high moisture content, up through approximately p = 500hPa. Between p = 500hPa and p = 250hPa there exists a significant and deep dry layer.

Over the course of the next 77 minutes in the simulation, deep convection develops in association with the emergence of our subject VHT. The vertical motion strengthens and a significant positive vorticity anomaly develops. Recent theoretical arguments suggest that these actions combine to limit the entrainment of dry air and, by extension, promote moistening of the column (Reasor et al. 2004). At the end of this period, we see saturated to super-saturated conditions up through the troposphere. The exception to this occurs from the surface up to p = 700mb where slightly drier conditions exist producing a shallow, relatively dry layer near the surface (dew point depression less than 2°C).

The reader will note that moistening of the mid and upper-levels was not the general rule of thumb observed over the genesis region in the area-averaged plots of relative humidity (Figure 4.17). While there is a significant area-averaged column moistening around 00UTC 8 Sep (t = 12h), the timing of the cross section we've been examining so far in this chapter is nine hours later in the simulation during a period of significant mid-level drying in the area-averaged relative humidity plots due to advection of dry air from outside the averaging box. This suggests for this simulated storm that the local scale tendency toward column moistening is directly opposed by the larger system scale drying process occurring at mid-levels during the Diana1 simulation. It also indicates that the local scale moisture processes may be just as important, if not more important, than the effects of larger scale moisture tendencies on the genesis of Diana. This suggests that, for more general tropical cyclogenesis events, local scale moisture effects cannot be neglected in lieu of system scale processes. While we do not disagree that system scale moistening of the mid-levels of the atmosphere likely has a positive effect on the genesis process and can quickly accelerate activity that ultimately leads to a tropical cyclogenesis event, it is apparent from our simulations that, given the right environmental conditions, local scale moistening can be more important and can help to overcome large scale drying that would be expected to suppress a genesis event.

5.4 Merger Activity

There remains one major aspect of the genesis process which we must specifically address, the merger of multiple smaller scale VHTs to form the vortex that ultimately became Hurricane Diana. Figure 5.14 is a close-up view of the low-level absolute

vorticity field (p = 925hPa) during the merger phase of Diana's development from 1130UTC 8 Sep to 14UTC 8 Sep (t = 23h 30min to t = 26h). We specifically chose this time period and region shown to capture the VHT scale evolution of the vorticity field immediately preceding the formation of the storm. This sequence of plots shows quite clearly the low-level merger of several cyclonic vorticity anomalies to form the central vortex. And what is most striking is the degree to which the emerging central vortex merges with and essentially annihilates multiple vorticity anomalies as is propagates from east to west. In Figure 5.14a the initial low-level vorticity field shows a complex of three relatively strong cyclonic vorticity anomalies located just to the right of the domain center (highlighted by the black circle) with on the order of ten to twenty additional vorticity anomalies located just to the west of this area (approximately half of these are negative anomalies and half are positive anomalies). Over the course of the next 90 minutes, the three original cyclonic vortices merge with each other and also with a fourth cyclonic vorticity anomaly to form a strong central vortex. This vortex begins to take on the appearance of a tropical system (see Figure 5.15 for radial plots of mean tangential wind during the simulation) with bands of elevated cyclonic vorticity spiraling into the center of the emerging vortex, particularly south and west of the storm center (see Figure 5.14d). Over the next hour, the central vortex continues to propagate toward the west and merges with additional cyclonic anomalies such that, by the end of the period plotted, the vorticity field to the west of the storm center is nearly devoid of strong positive and negative anomalies. This is the beginning of the vorticity moat that eventually develops in the domain (see Section 4.4.1). After the initial merger of the main anomalies around t = 24h 30min (Figure 5.14c), a band of elevated cyclonic vorticity develops and is

advected around the vortex center by the resultant wind field. Embedded within this vorticity band are several smaller-scale cyclonic vorticity anomalies which merge with neighboring cyclonic anomalies. The resultant vorticity cores become elongated by the developing wind field and take on a spiraling appearance into the storm center. The merger activity of these small-scale features coupled with the system scale mergers that form the central vortex annihilate and axisymmetrize much of the initial field of anomalous cyclonic vorticity. This action is occurring most obviously to the south and west of the vortex center, but robust merger activity is evident over a significant portion of the domain. Thus, while one may tend to focus on the merger of the largest anomalies to form the central vortex that eventually develops into Hurricane Diana, merger activity is taking place on many smaller scales within the domain. And while the largest scale merger arguably have the biggest impact on the tropical cyclogenesis process, the smaller scale mergers affect features like spiral bands and, consequently, also influence the evolution of the total field of low-level absolute vorticity.

We must also note an additional qualitative aspect of the merger activity that becomes evident when one examines animations of the low level vorticity field. These animations suggest the likelihood of merger of two adjacent vorticity anomalies is generally dependent upon the strength of the anomalies themselves. That is, in our animations we see a tendency for stronger anomalies to merge before weaker ones. This is seen to a certain degree in Figure 5.14, but the temporal resolution of the plots does not lend itself well to this type of analysis. We were able to confirm this visually over the course of the entire simulation but did not have the opportunity to quantitatively verify this feature of the merger activity.

5.5 Summary of VHT-Scale Analyses

In this chapter, we investigated the general characteristics of vortical hot towers observed in a high resolution simulation examining the formation of Hurricane Diana. We found that many characteristics of the VHTs resolved in our Diana1 simulation agree qualitatively with coarser resolution simulations of H04 and M06. Particularly, the strength of the maximum vertical velocity in each core, the observed altitude of this maximum and the strength of the cyclonic low-level absolute vorticity were generally consistent among each simulation. Other characteristics, like horizontal size of the VHT updraft core and the number of VHTs resolved within the domain, were similar, but they showed a dependence on grid resolution that was predictable. That is, the higher resolution simulation resolved more VHTs within the domain, and these VHTs had horizontal dimensions that were generally smaller than the VHTs resolved in the coarser resolution runs. The diameter of the VHT updrafts in our Diana1 simulation (based on the w = 3ms^{-1} contour) was approximately half the diameter of the updraft cores generated in the H04 simulation (6km versus 10km, respectively). What the author did not expect was the differences in the structure of the absolute vorticity field, particularly the magnitude of the anticyclonic vorticity anomalies. We found that the Diana1 simulation produced a field of negative vorticity that was much larger than what was observed in the H04 and M06 runs. Additionally, the negative vorticity cores produced in the Diana1 simulation were much stronger than those produced in the coarser resolution runs with central values nearly three times as strong as the H04 and M06 negative vorticity anomalies.

Other characteristics examined include the moisture field in a representative VHT core which showed that the atmospheric column on the VHT scale was significantly moistened by the updraft core. This opposed the larger-scale mid-level tendencies noted in Chapter 4 and suggested the importance of VHT-scale processes in determining the relative humidity values in mid-levels of the atmosphere. Lastly, we examined low-level absolute vorticity associated with a prominent merger event that was observed around the time that Tropical Storm Diana was named. The scale of this merger and other obvious smaller scale mergers in the domain suggested that merger activity was ubiquitous and important in the genesis of Diana.

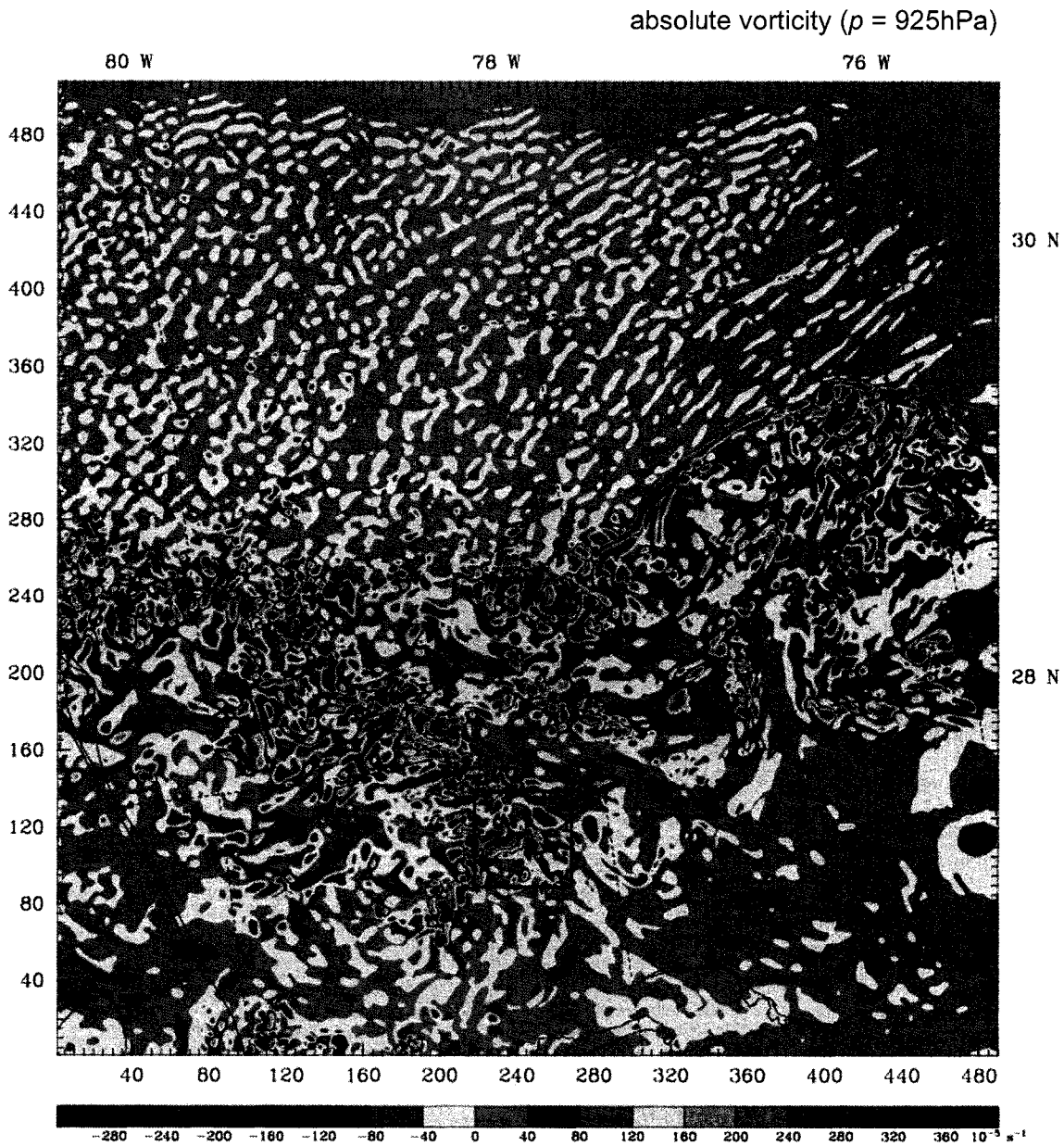

Figure 5.1. Plot of low-level absolute vorticity (p = 925hPa) at t = 21h 10min from the 1km grid. Note the slight change in the color contouring from previous absolute vorticity plots to highlight more of the smaller scale features. Tick marks on the bottom and left are gridpoints in units of kilometers.

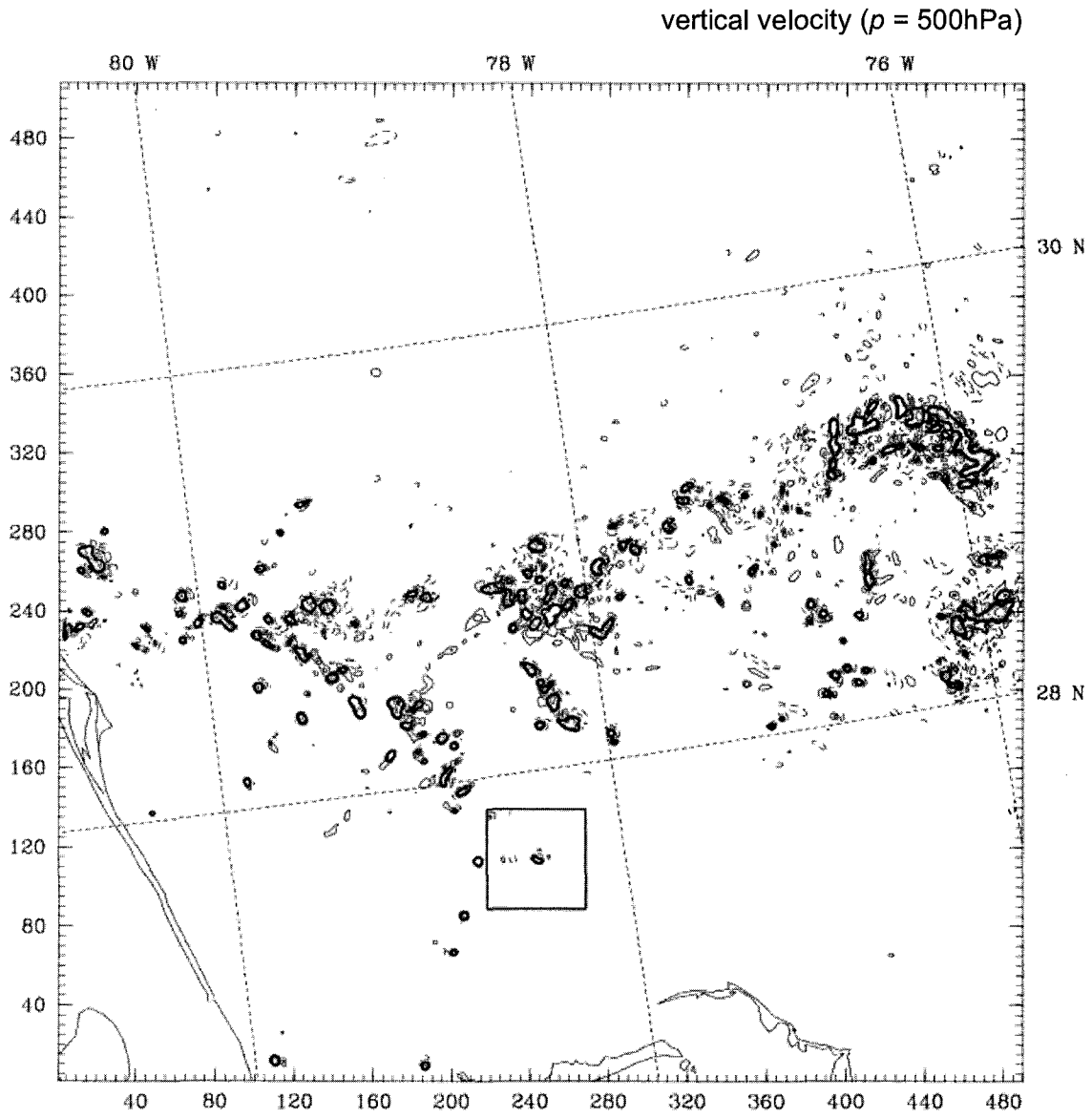

Figure 5.2. Plot of mid-level vertical velocity (p = 500hPa) at t = 21h 10min from the 1km grid. Contours are at +/- 1, 2, 3, 4, 8, and 16 ms^{-1}. The $3ms^{-1}$ contour is the heavy black line. The zero contour is omitted. Tick marks on the bottom and left are gridpoints in units of kilometers.

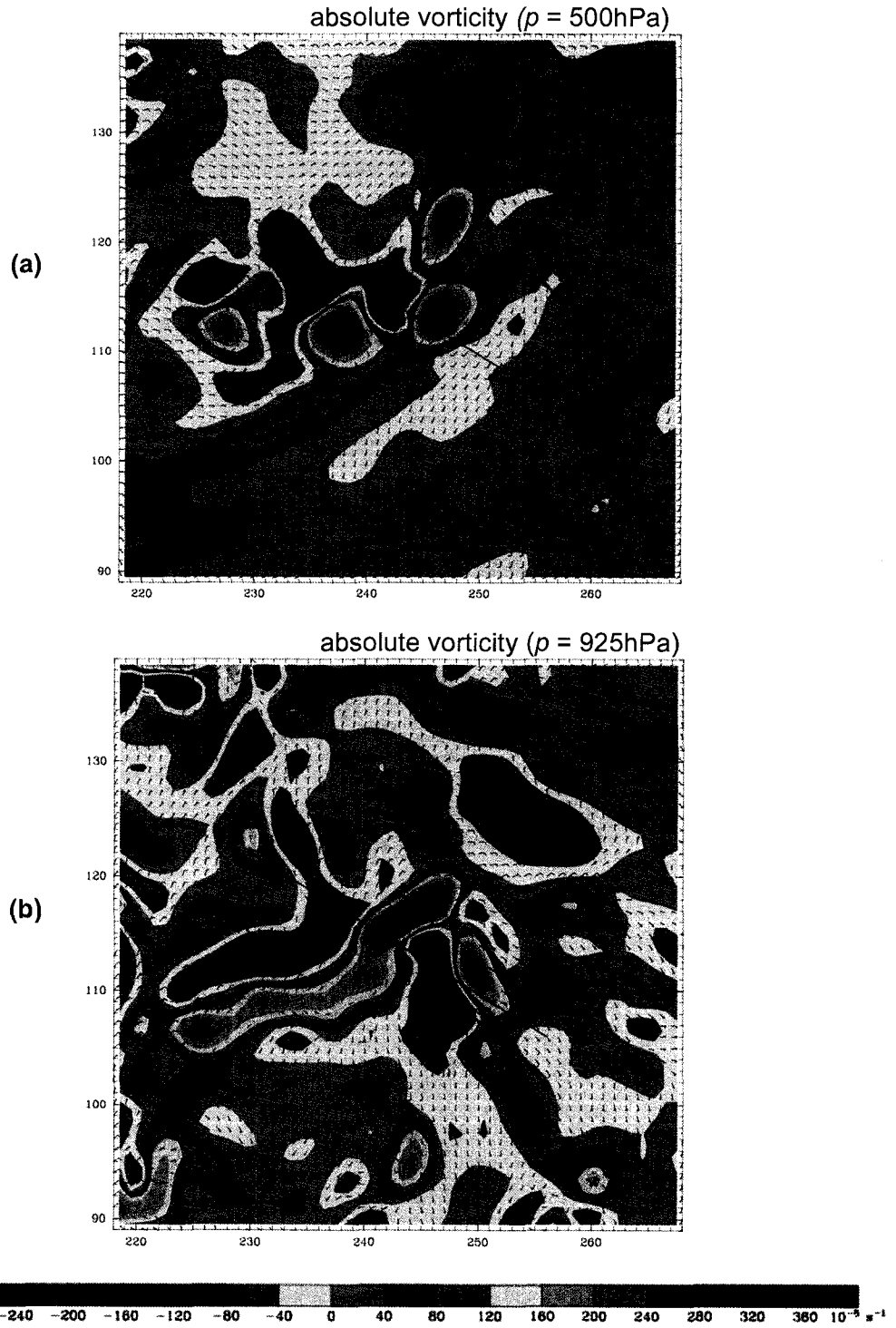

Figure 5.3. Close-up view of horizontal winds and absolute vorticity at (a) p = 500hPa and (b) p = 925hPa at t = 21h 10min into the simulation. Region of close up view is from the south central part of the 1km grid as indicated by the black box in Figure 5.1. Color contouring for absolute vorticity is the same as in Figure 5.1. Each full wind barb indicates a windspeed of 5ms^{-1}. Wind barbs are displayed on a grid with 1km horizontal grid spacing. Tick marks on the bottom and left are gridpoints in units of kilometers.

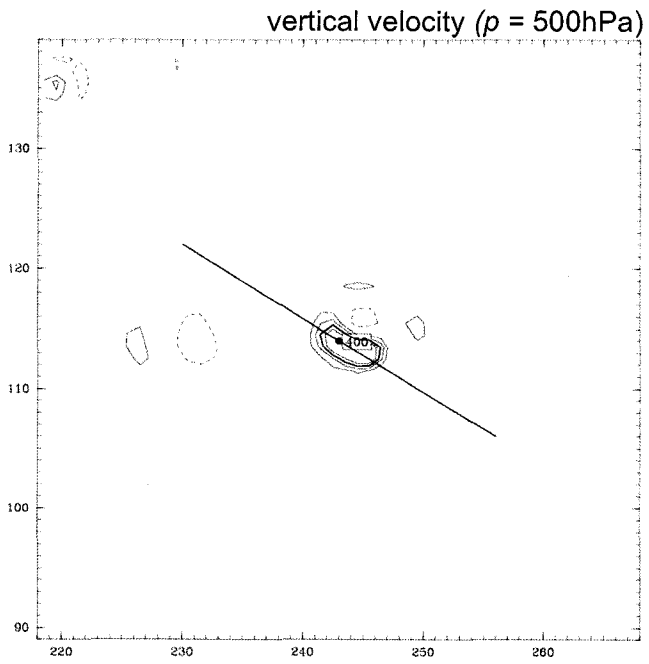

Figure 5.4. Close-up view of mid-level vertical velocity (p = 500hPa) at t = 21h 10min. Region of close-up view is from the south central part of the 1km grid as indicated by the black box in Figure 5.2. Contours are at +/- 1, 2, 3, 4, 8, and 16 ms^{-1}. The $3ms^{-1}$ contour is the heavy black line. The zero contour is omitted. Tick marks on the bottom and left are gridpoints in units of kilometers.

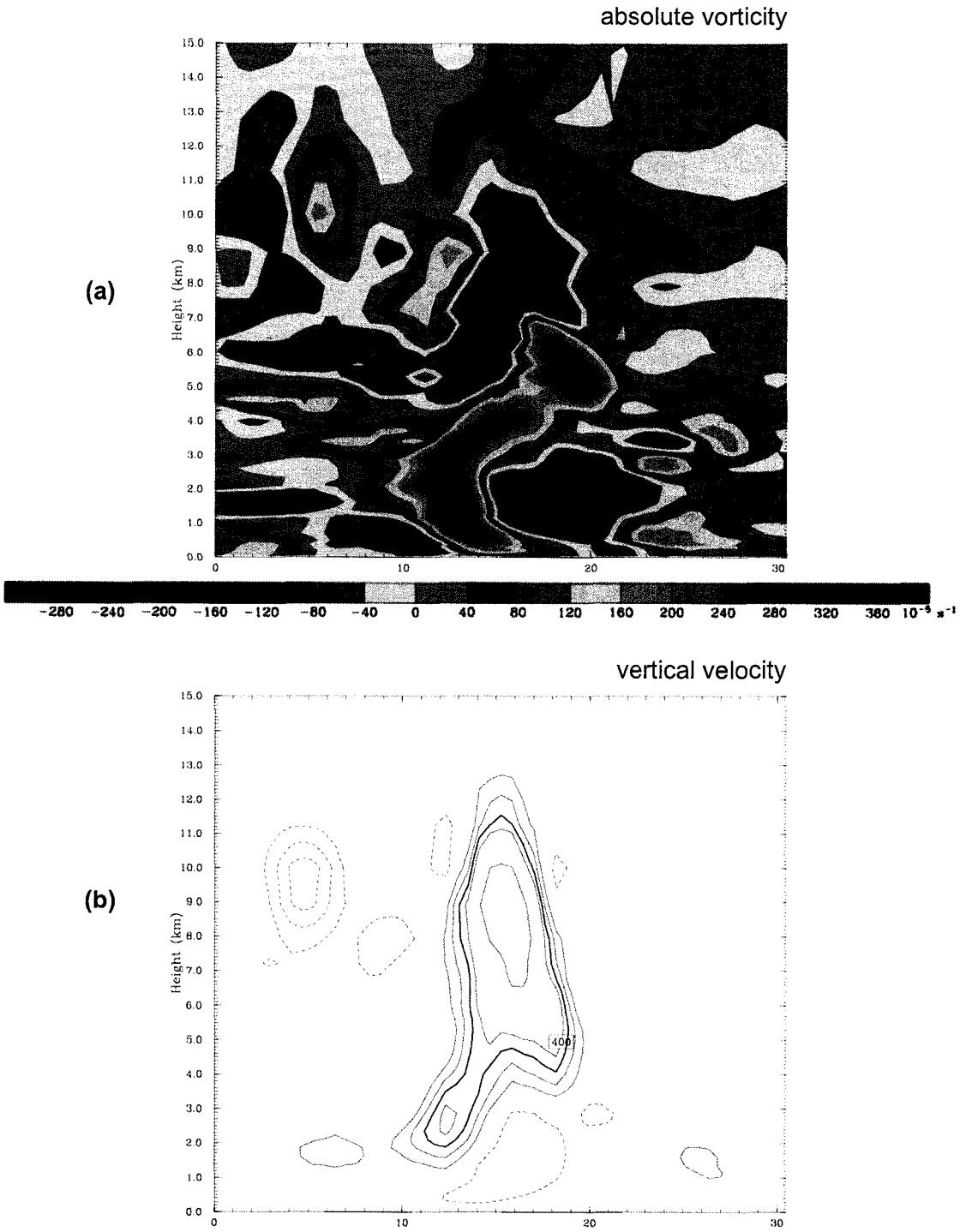

Figure 5.5. Cross sections of (a) absolute vorticity and (b) vertical velocity along the line indicated in both Figure 5.3 and Figure 5.4. Color contouring for absolute vorticity is the same as in Figure 5.3. Contours for vertical velocity are +/- 1, 2, 3, 4, 8, and 16 ms^{-1}. The $3ms^{-1}$ contour is the heavy black line. The zero contour is omitted. Height and distance (km) are as indicated along the *y* and *x* axes, respectively.

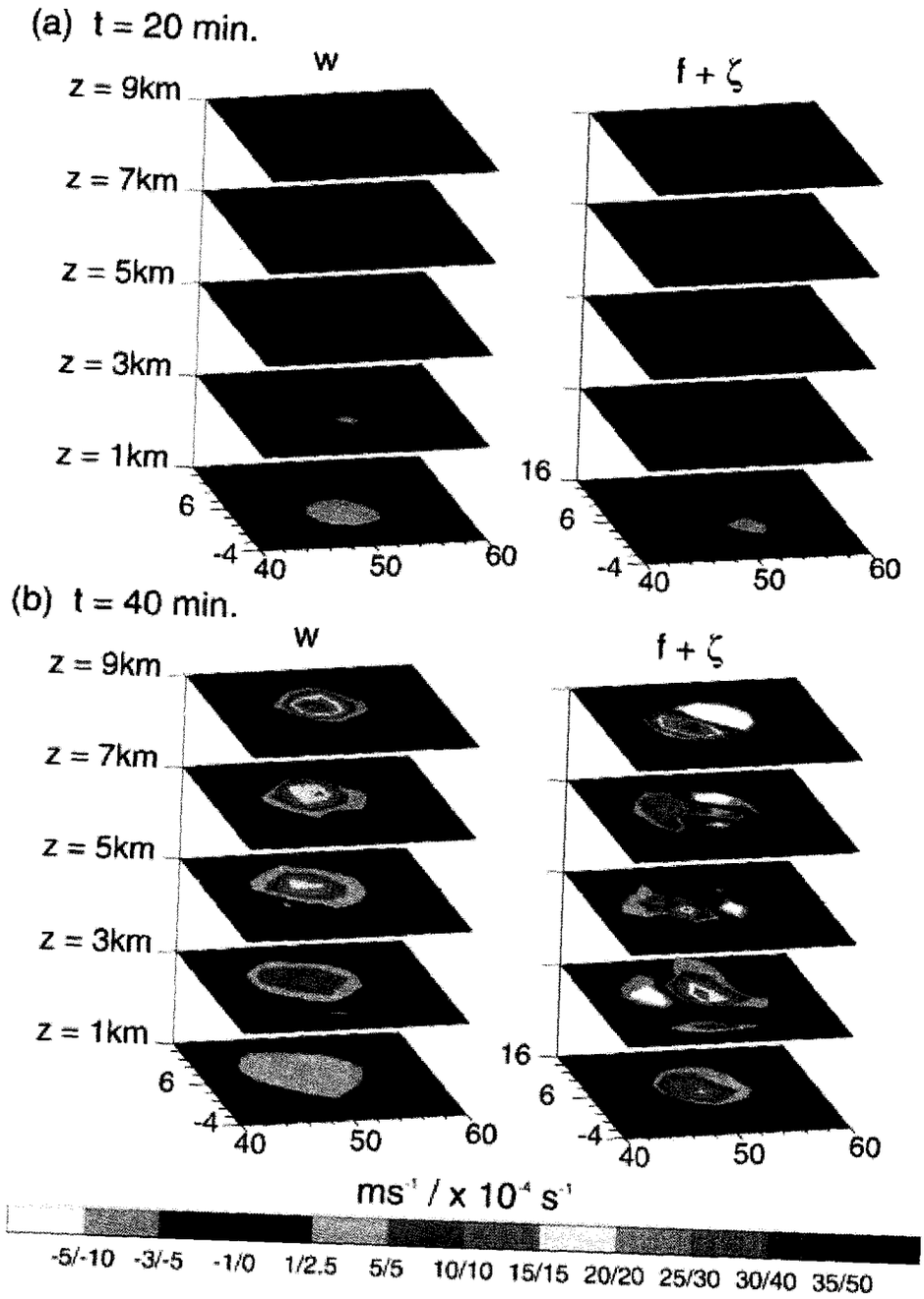

Figure 5.6. Plot of vertical motion and absolute vorticity at (a) t = 20min and (b) t = 40min in the M06 simulation. Taken from Figure 9 of M06.

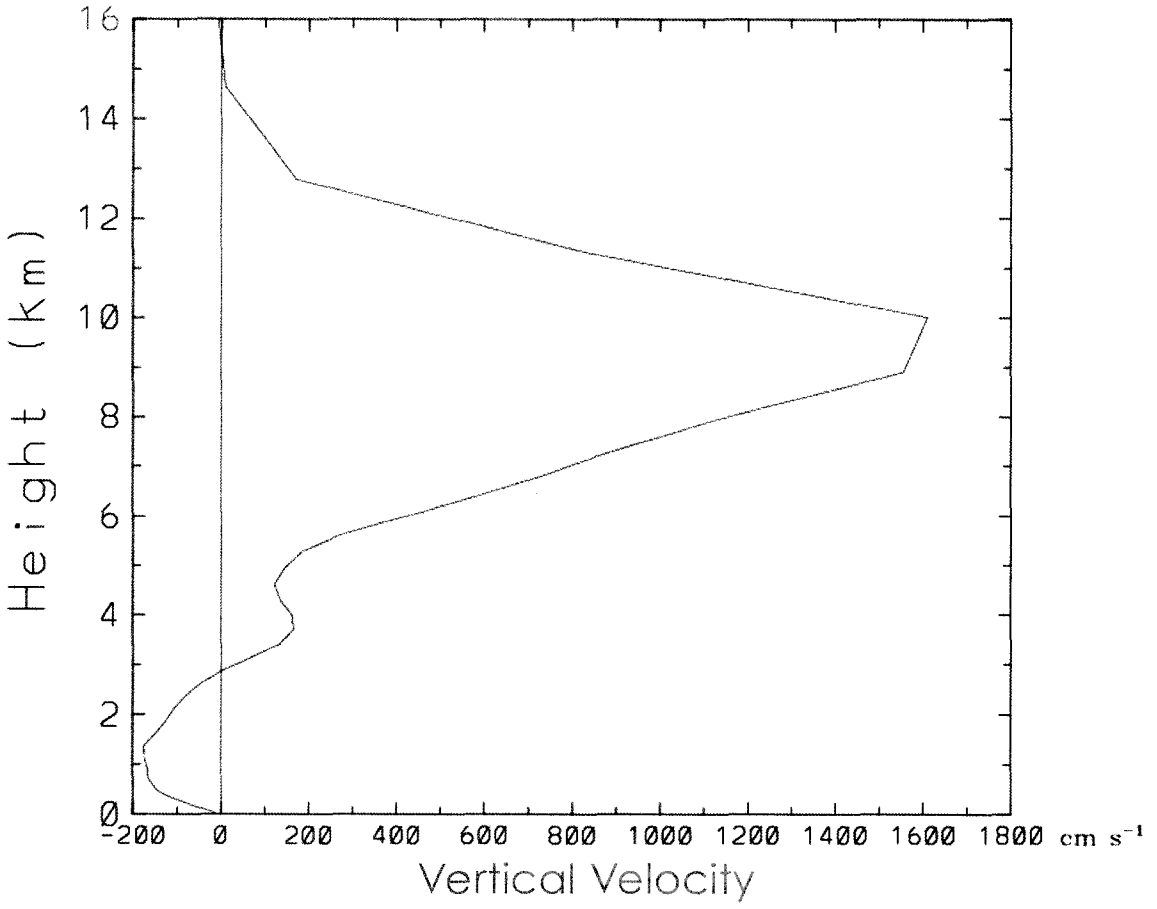

Figure 5.7. Profile of vertical velocity as a function of height in the center of the updraft core highlighted in Figure 5.4. Location of the vertical profile is indicated by the heavy black dot in the center of the updraft core.

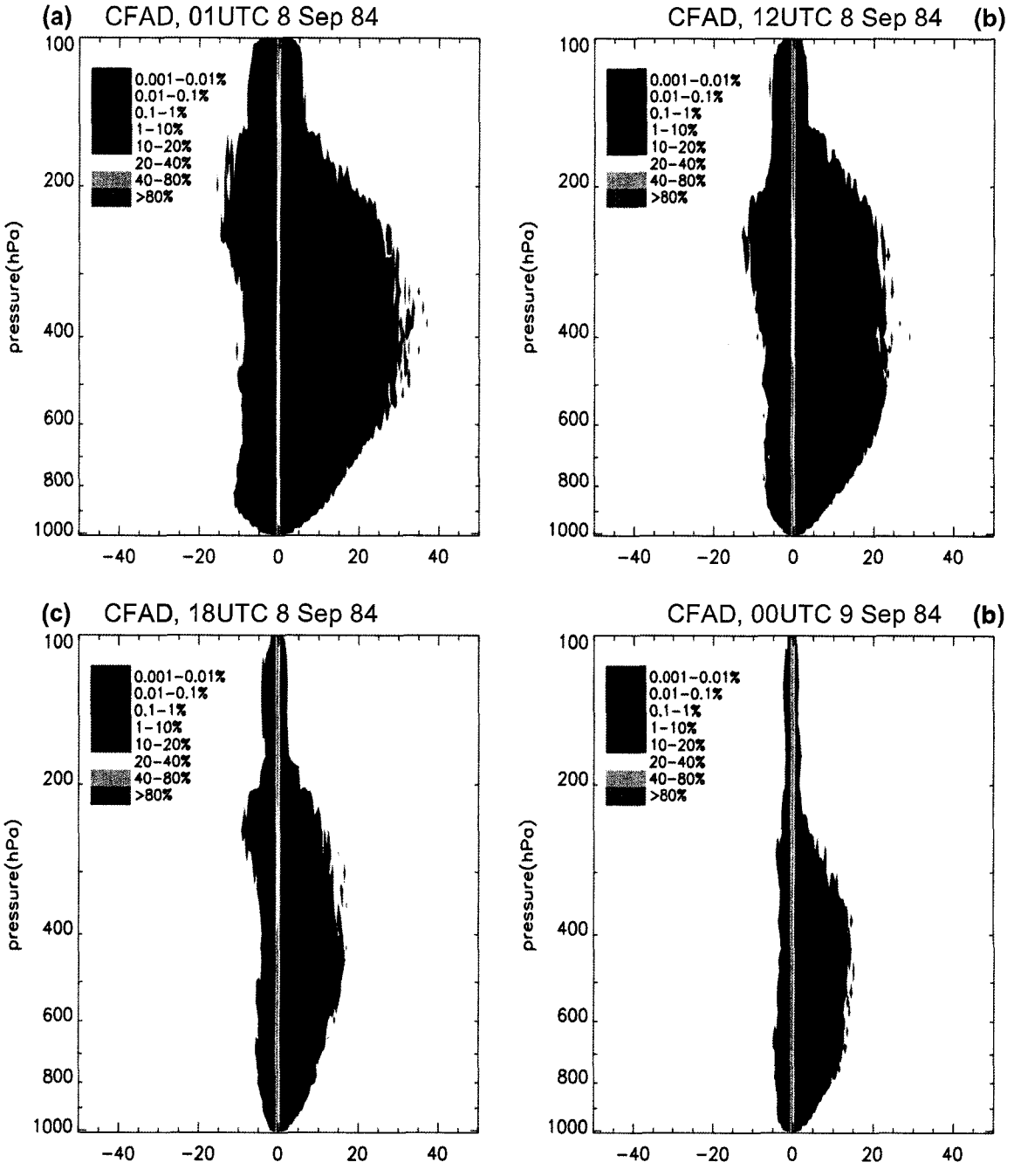

Figure 5.8. Contoured frequency by altitude diagrams (CFADs) of vertical velocity values observed (a) t = 13h (01UTC 8 Sep 84), (b) t = 24h (12UTC 8 Sep 84), (c) t = 30h (18UTC 8 Sep 84) and (d) t = 36h (00UTC 9 Sep 84) on our 1km grid. Filled color contours indicate the frequency of occurrence of a specified value of vertical velocity (see legend for contour values). Observations are taken over a 3° by 3° box located in the genesis area. See Figure 4.11 for a depiction of the averaging box.

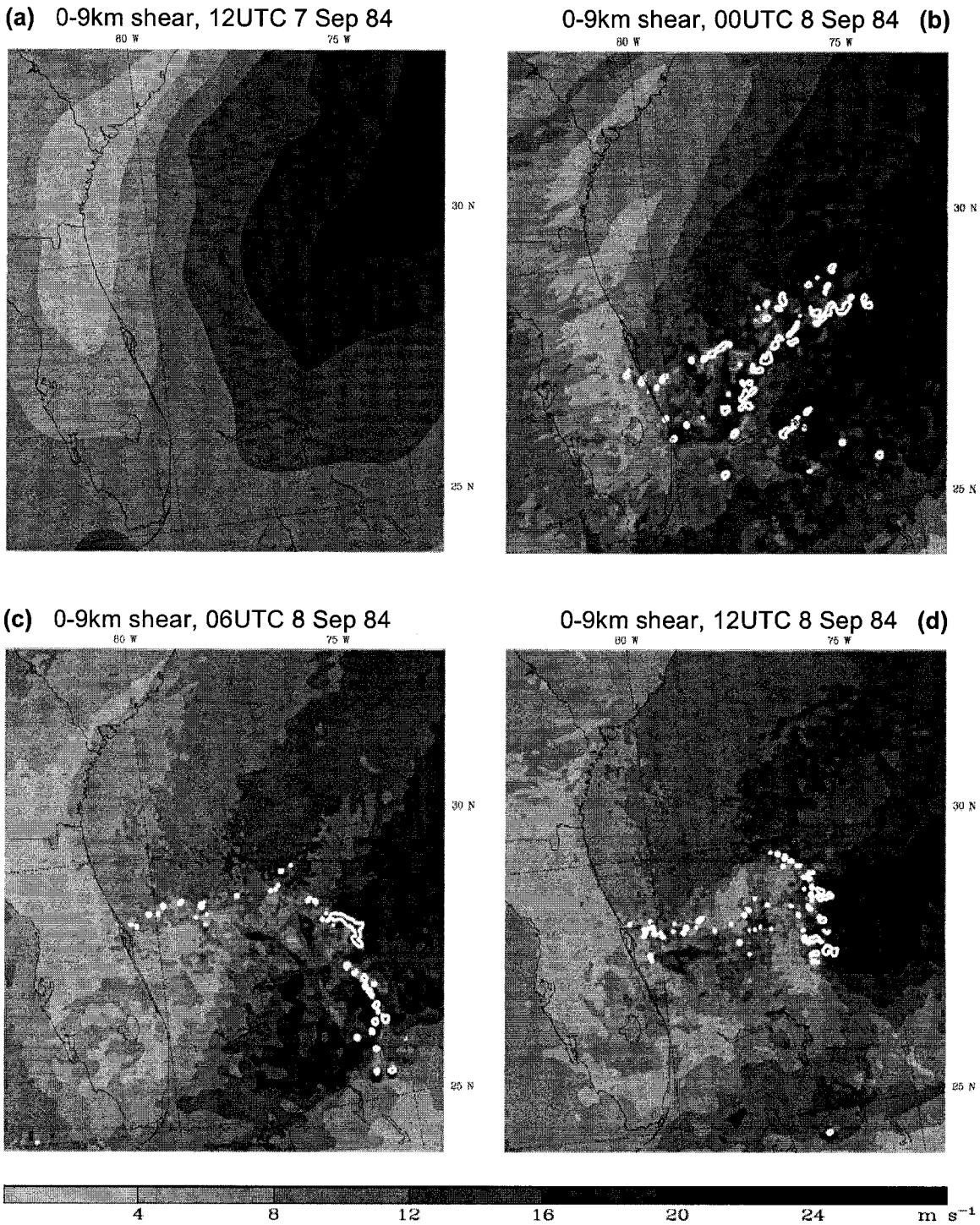

Figure 5.9. Plot of surface to z = 9km shear values (magnitude only) at (a) 12UTC 7 Sep 84 (t = 0h), (b) 00UTC 8 Sep 84 (t = 12h), (c) 06UTC 8 Sep 84 (t = 18h) and (d) 12UTC 8 Sep 84 (t = 24h) on the 3km grid. Color contours are every 4ms^{-1} over the 9km depth. White contours overlaid the filled contours indicate areas with upward vertical motion values at least 3ms^{-1}.

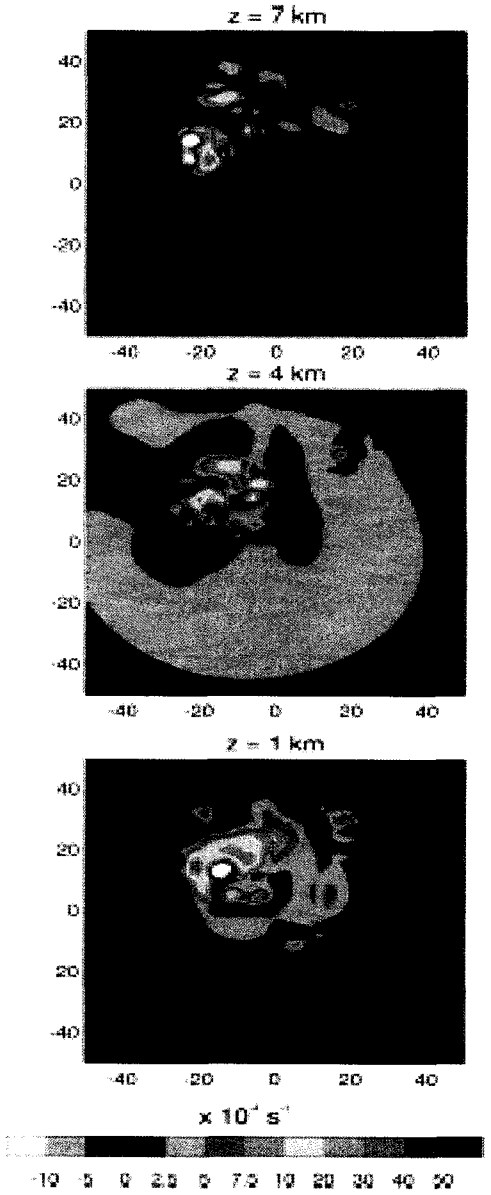

Figure 5.10. Absolute vorticity field at t = 7h in the M06 control simulation. Contours are in units of $10^{-4}s^{-1}$. Axes are in kilometers. Taken from Figure 3 of M06.

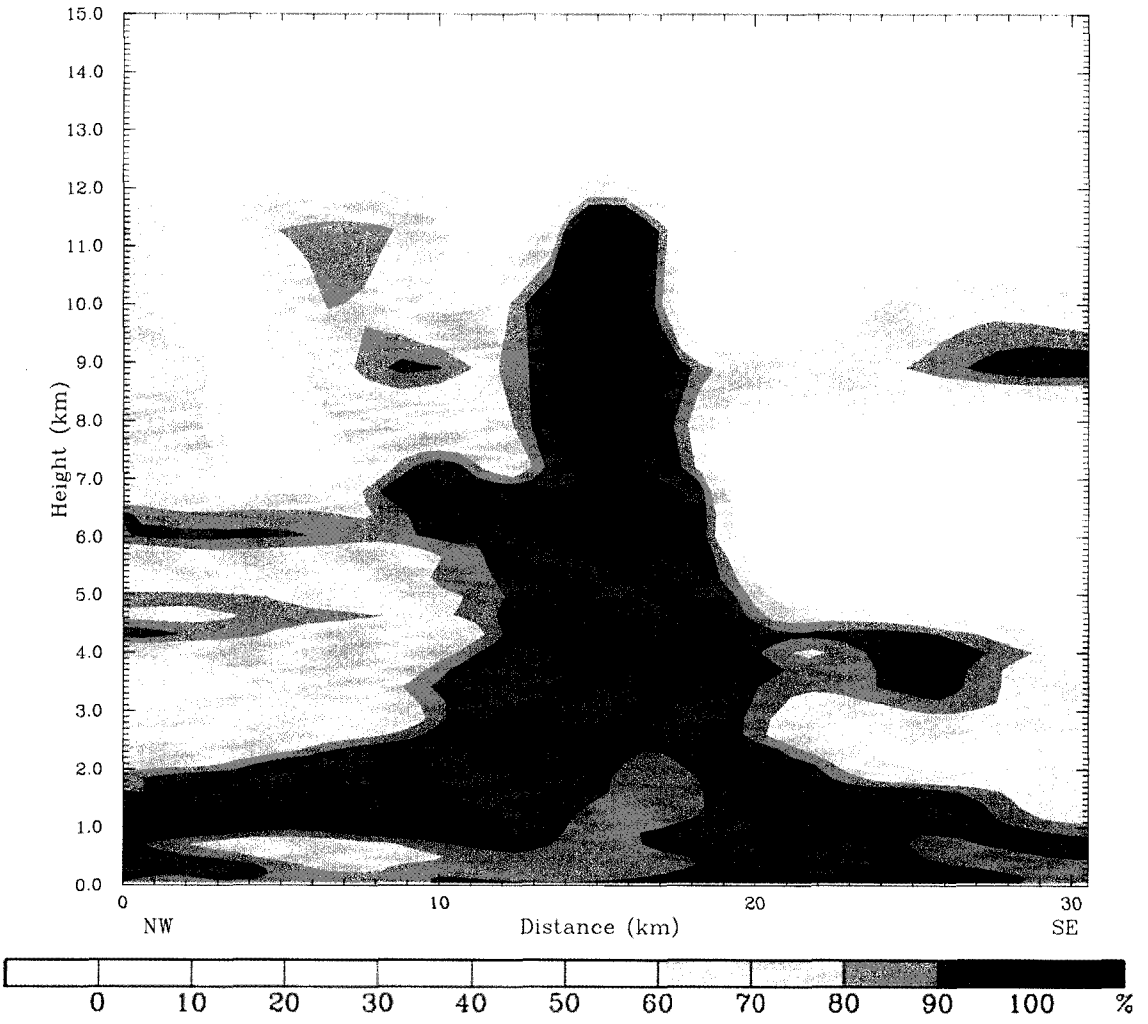

Figure 5.11. Cross section of relative humidity along the line indicated in both Figure 5.3 and Figure 5.4. Colored contours are every 10% beginning at 50%. Supersaturated areas, if the exist, are very dark gray. Height and distance (km) are as indicated along the y and x axes, respectively.

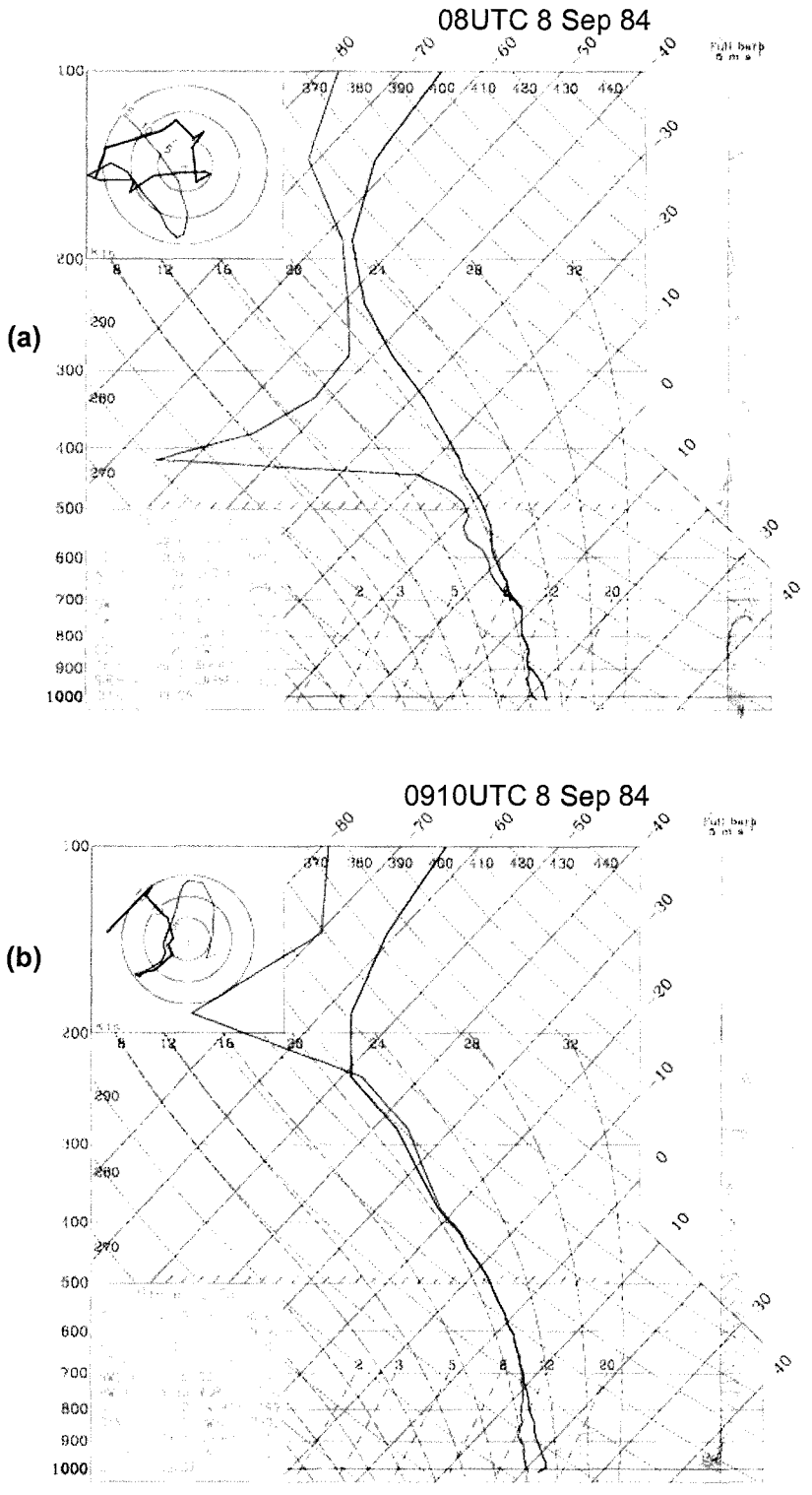

Figure 5.12. Skew-T/Log P diagram in the center of the updraft core highlighted in Figure 5.4 at (a) t = 20h (08UTC 8 Sep 84) and (b) t = 21h 10min (0910UTC 8 Sep 84). Location of the vertical profile is indicated by the heavy black dot in the center of the updraft core. Each full wind barb represents a wind speed of 5ms^{-1}.

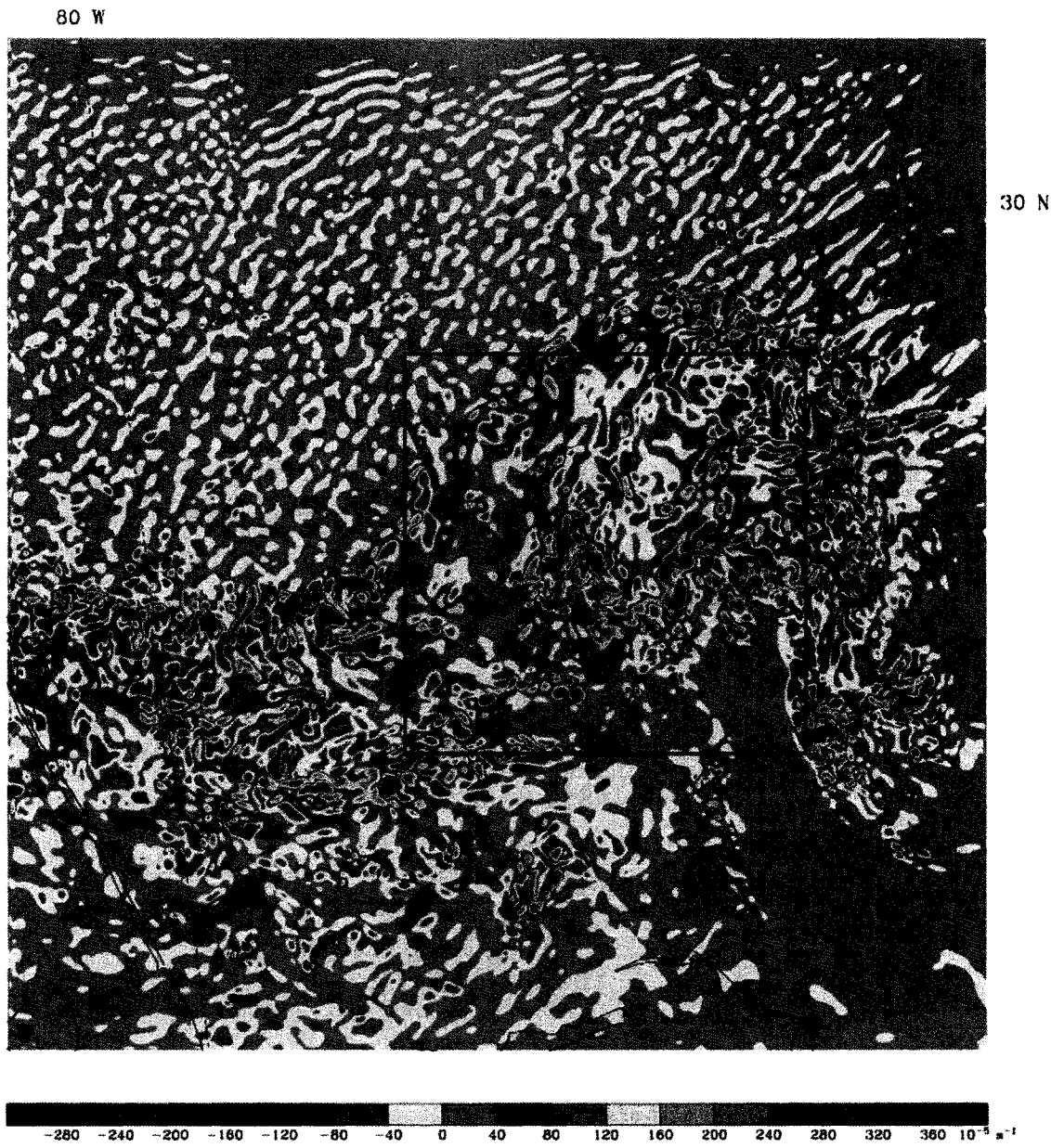

Figure 5.13. Plot of low-level absolute vorticity (p = 925hPa) on the 1km grid of the Diana1 simulation at t = 23h 30min (1130UTC 8 Sep). The box depicted in the east central portion of the domain shows the relative size and location of the close-up view that will be used to examine merger activity.

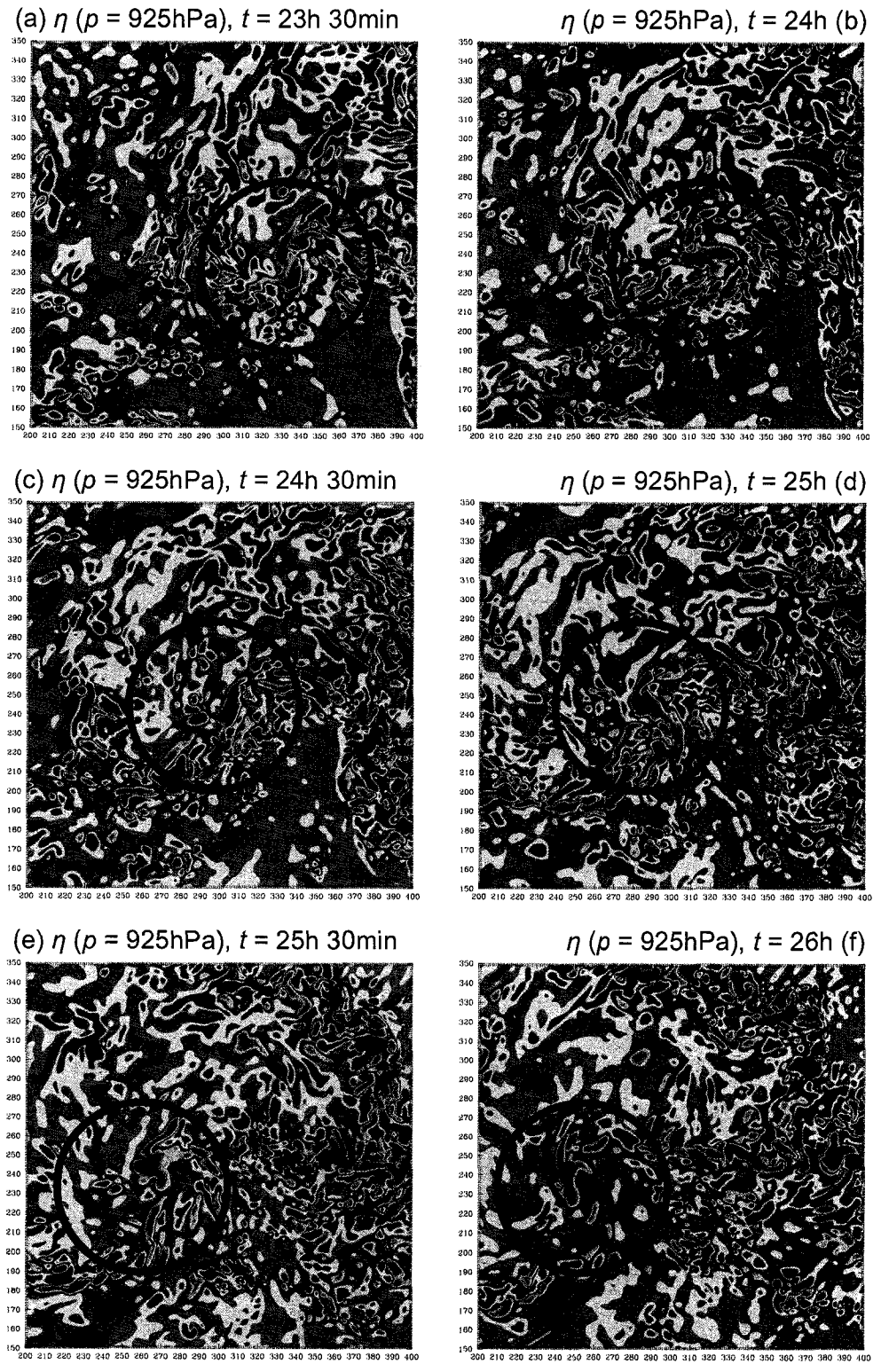

Figure 5.14. Close-up view of low-level (p = 925hPa) absolute vorticity during merger event on 1km grid of Diana1 simulation. See (Figure 5.13) for location of box relative to 1km grid. Tick marks on the bottom and left are gridpoints in units of kilometers from the domain origin. The black circle highlights a merger sequence.

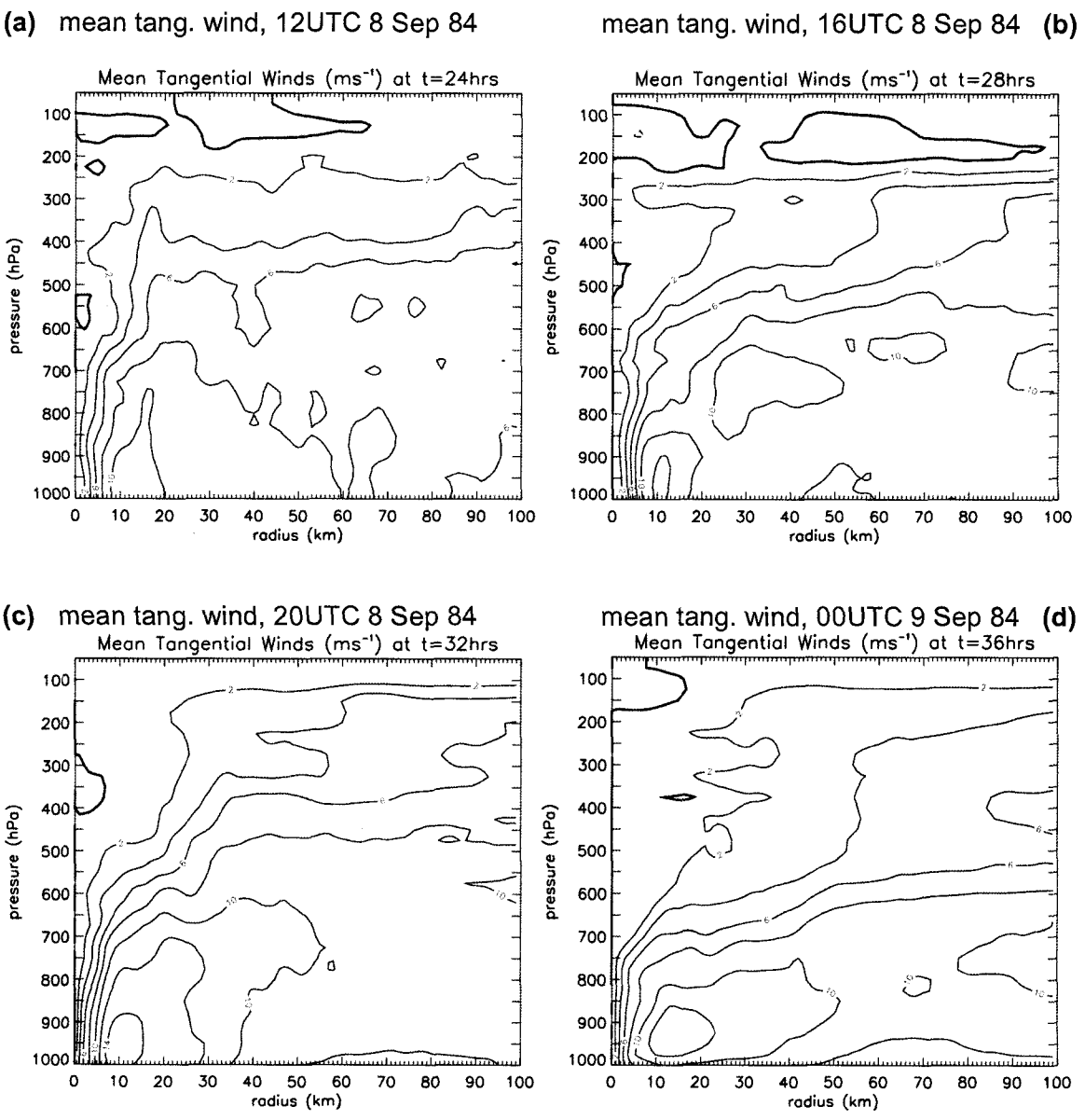

Figure 5.15. Radial profile of mean tangential wind speed for the emerging vortex based on data from the 3km grid of the Diana1 simulation. Fields are plotted at (a) 12UTC 8 Sep 84 (t = 24), (b) 16UTC 8 Sep 84 (t = 28h), (c) 20UTC 8 Sep 84 (t = 32h) and (d) 00UTC 9 Sep 84 (t = 36h). Contours are every 2ms^{-1}. The heavy black line is the zero contour.

Chapter 6

CONCLUSIONS AND RECOMMENDATIONS FOR FUTURE WORK

6.1 Summary of Current Study

In this study we have provided some new insights into the vortical hot tower route to tropical cyclogenesis as simulated in a full physics numerical weather prediction model (MM5) at near-cloud resolving scales. Specifically, we investigated the genesis of Hurricane Diana with 2 main goals: 1) determine if the primary conclusions of H04 and M06 change as horizontal grid-spacing decreases to 3km to 1km and 2) examine more closely the influence of vortical hot towers on the tropical cyclogenesis process from the perspective of a very high resolution mesoscale simulation.

As grid-spacing decreased from 3km to 1km, we found that the fundamental physics of the two-stage hurricane formation mechanism first proposed by H04 does not change significantly. In concert with the H04 study and the idealized study of M06, our very high resolution results suggest the first stage of this process, pre-conditioning, is characterized by the initiation of highly vortical deep convective cores, or vortical hot towers (VHTs), and the formation of a convective divergence profile (CDP, Mapes and Houze 1995, Houze 1997, Tory et al. 2006a and 2006b) with convergence at the surface to mid-levels and divergence aloft. In our high resolution simulation, the CDP was

observed in an area-averaged sense over a 3° by 3° box located within the genesis region. While we also found a stratiform-like component to this divergence profile, the significant area-averaged convergence near the surface indicated a broad scale secondary circulation generated by the VHTs. As first suggested by H04 and M06, and confirmed to a large degree by our analysis of the area-averaged vorticity fields, this secondary circulation results in a significant influx of angular momentum into the genesis region and a corresponding increase of low and mid-level absolute vorticity during the pre-conditioning period. In the upper troposphere, the situation is reversed with significant area-averaged divergence engulfing this region of the atmosphere, particularly during pre-conditioning, which results in a tendency toward decreasing values of absolute vorticity.

During the merger phase of development, we found further agreement between our study and the previous VHT studies. In both our high resolution simulation and in previous studies of H04 and M06, mergers of the vorticity anomalies dominate the development of the low level cyclonic vortex during this period of time. Low-level absolute vorticity values continue to increase, but the rate of increase is significantly slowed as the low-level convergence decreases and the system begins to consolidate the existing anomalies to create larger and/or more intense low-level vortices. This becomes particularly evident when we examined a merger event in our simulation in which multiple cyclonic vorticity anomalies consolidated to create the central warm core vortex of the simulated Tropical Storm Diana. What was most interesting in our simulation and in this merger event in particular, was the observation that merger activity was ubiquitous to the genesis process and was occurring on several horizontal scales during the

simulation. We noted, in particular, a series of mergers of small scale vorticity anomalies that appeared to form a band of elevated vorticity values spiraling into the storm center. The merger activity was shown to be an important process in this phase of tropical cyclogenesis and was consistent with merger observations in the numerical studies of H04 and M06. Since our Diana1 simulation was performed with 1km horizontal grid spacing compared to 2km and 3km for the H04 and M06 studies, respectively, we were able to resolve more fine-scale variability of individual hot towers and examine their impact on the genesis process.

This finer-scale variability also led to slight differences in terms of the general characteristics of our high resolution simulation. We found our Diana1 experiment generated nearly an order of magnitude more VHTs compared to the H04 simulation. Many of the updraft cores in our simulation also had significantly smaller horizontal scales relative to the H04 and M06 cores (up to a factor of 2 smaller), though both the altitude and intensity of the maximum mean vertical velocity were generally the same in all three simulations. However, the structure of the low-level vorticity anomalies associated with these updraft cores was distinctly different between the simulations. Due primarily to the order of magnitude increase in the number of gridpoints for a given area, our 1km simulation exhibited a highly more textured appearance to the low-level vorticity field with positive and negative vorticity cores permeating nearly the entire domains. In contrast, the H04 simulation displayed a large fairly contiguous area of positive vorticity values in the center of the genesis region with a limited number of anticyclonic cores on the periphery. Such differences in the texture of the vorticity field were expected given the increased resolution in our simulation.

What was not expected, however, was the difference in the magnitude of the negative vorticity cores. While the maximum values of cyclonic vorticity were consistent across the 3km and 1km simulations with $\eta_{max} \sim 3.5$ to $4.0\times10^{-3}s^{-1}$, the strength of the anticyclonic cores differed significantly. The Diana1 simulation created anticyclonic vorticity anomalies that possessed peak magnitudes of $\eta_{min} \sim -3.0\times10^{-3}s^{-1}$ compared to $\eta_{min} \sim -1.0\times10^{-3}s^{-1}$ for the H04 and M06 simulation. Additionally, the high-resolution simulation generated significantly more anticyclonic vorticity anomalies than the H04 and M06 studies. This resulted in a local environment in the Diana1 experiment that appeared not as primed for development. As a result, the rate of the tropical cyclogenesis at 1km horizontal grid spacing was tempered and did not develop as deep a storm as the H04 simulation.

In the moisture field on the VHT scale, we observed a completely different tendency. The Diana1 moisture profile through an example VHT core showed deep moistening of the column by the action of the convective updraft, particularly at mid-levels of the atmosphere. This feature was consistent in all of the individual vortical hot towers we examined. If we combine this observation with the fact that VHT convective cores exist throughout the domain and induce an area-averaged broad-scale in-up-out secondary circulation that converges angular momentum into the genesis region, we are must conclude that the simulated tropical cyclogenesis of Hurricane Diana has an intrinsic dependence on small scale features.

Finally, we offer that the tropical cyclogenesis process is inherently a bottom-up process which is controlled, to a certain degree, by the VHT activity occurring near the surface. While the mesoscale mid-level vortex in this simulation played an important

role through larger scale forcing and by creating an environment of rich cyclonic vorticity, the VHTs themselves and their collective impact on the genesis region were central in creating an environment conduce to tropical cyclogenesis.

6.2 Recommendations for Future Work

While we have uncovered several important aspects of the tropical cyclogenesis process in this study, there is still a great deal to be learned about the physics of hurricane formation and, specifically, how VHTs contribute to that process. As a result we suggest additional studies be completed to gain further insight into the tropical cyclogenesis process.

1. Perform additional high resolution cloud resolving numerical studies of Hurricane Diana with horizontal grid spacing of 100m or less. We recognize such a study would likely not be completed using MM5 or another mesoscale model due to their use of boundary layer parameterizations, but we feel such a study is imperative to gain a complete understanding of how cloud scale convective features like VHTs contribute to the larger scale spin-up of the tropical vortex. Since there were significant unexpected differences between our 1km simulation and the coarser resolution experiments of H04 and M06, it is likely that order 100m simulation would provide a more complete understanding of the genesis process.

2. Once we have completed simulations and analysis of Hurricane Diana at scales as fine as 100m and fully understand the Diana's genesis at all applicable scales, additional high resolution studies should be performed on idealized and real-case cyclogenesis events. The real-case events should include at the very least an early season storm and a

more typical mid season storm with origins in the deep tropics. The difficulty here will be selecting cases that have sufficient observations near the emerging vortex and prior to the genesis event such that the vortex does not have to be bogused into the applicable model. Because of the availability of observational data, it is likely that any future real-case storms to be studied would necessarily be fast developing storms that underwent genesis in the vicinity of the southeastern United States, Bahamas or Caribbean.

3. Perform sensitivity studies to determine the environmental conditions that control the formation, evolution and maintenance of VHTs. The goal of this study would be to determine if there are threshold values of environmental conditions that lead to VHT generation. Additionally, this study would likely be able to establish if certain conditions accelerate or slow down the generation of VHTs. It would also be important to understand if the lack of VHT production in a particular case necessarily inhibits the tropical cyclogenesis process.

4. Perform similar high resolution experiments in other ocean basins to determine if the VHT tropical cyclogenesis process is common outside of the Atlantic. In the event the VHT pathway to tropical cyclogenesis is common in other basins, determine if the characteristics of other basin VHT differ from the VHTs we observed.

REFERENCES

Bister, M., and K. Emanuel, 1997: The genesis of Hurricane Guillermo: TEXMEX analyses and a modeling study. *Mon. Wea. Rev.*, **125,** 2662-2682.

Bosart, L. F., and J. A. Bartlo, 1991: Tropical storm formation in a baroclinic environment. *Mon. Wea. Rev.*, **119,** 1979-2013.

Braun, S. A., 2002: A cloud-resolving simulation of Hurricane Bob (1991): Storm structure and eyewall buoyancy. *Mon. Wea. Rev.*, **130,** 1573-1592.

Bryan, G. H., J. C. Wyngaard, and J. M. Fritsch, 2003: Resolution requirements for the simulation of deep moist convection. *Mon. Wea. Rev.*, **131,** 2394-2416.

Charney, J. G., and A. Eliassen, 1964: On the growth of the hurricane depression. *J. Atmos. Sci.*, **21,** 68-75.

Cotton, W. R. and Coauthors, 2003: RAMS 2001: Current status and future directions. *Meteor. Atmos. Phys.*, **82**, 5-29.

Cressman, G. P., 1959: An operational objective analysis scheme. *Mon. Wea. Rev.*, **87,** 367-374.

Davis, C. A., and L. Bosart, 2001: Numerical simulations of the genesis of Hurricane Diana (1984). Part I: Control simulation. *Mon. Wea. Rev.*, **129,** 1859-1881.

Davis, C. A., and L. Bosart, 2002: Numerical simulations of the genesis of Hurricane Diana (1984). Part II: Sensitivity of track and intensity prediction. *Mon. Wea. Rev.*,

130, 1100-1124.

Davis, C. A., and L. Bosart, 2003: Baroclinically Induced Tropical Genesis. *Mon. Wea. Rev.,* **131,** 2730-2747.

DeMaria, M., 1996: The effect of vertical shear on tropical cyclone intensity change. *J. Atmos. Sci.,* **53,** 2076-2087.

Dudhia, J., 1989: Numerical study of convection observed during the Winter Monsoon Experiment using a mesoscale two-dimensional model. *J. Atmos. Sci.,* **46,** 3077-3107.

Dudhia, J., 1993: A nonhydrostatic version of the Penn State-NCAR mesoscale model: Validation tests and simulation of an Atlantic cyclone and cold front. *Mon. Wea. Rev.,* **121,** 1493-1513.

Emanuel, K. A, J. D. Neelin, and C. S. Bretherton, 1994: On large-scale circulations in convecting atmospheres. *Quart. J. Roy. Meteor. Soc.,* **121,** 1111-1143.

Enagonio, J., and M. T. Montgomery, 2001: Tropical cyclogenesis via convectively forced vortex Rossby waves in a shallow water primitive equation model. *J. Atmos. Sci.,* **58,** 685-706.

Frank, W. M., 1987: Tropical cyclone formation. *A Global View of Tropical Cyclones.* R. L. Elsberry, W. M. Frank, G. J. Holland, J. D. Jarell, and R. L. Southern, Eds., Office of Naval Research, 53-90.

Frank, W. M., and E. A. Ritchie, 2001: Effects of vertical wind shear on the intensity and structure of numerically simulated hurricanes. *Mon. Wea. Rev.,* **127,** 2044-2061.

Gray, W. M., 1968: Global view of the origin of tropical disturbances and storms, *Mon. Wea. Rev.,* **96,** 669-700.

Grell, G. A., J. Dudhia, and D. R. Stauffer, 1994: A description of the fifth-generation

Penn State/NCEP mesoscale Model (MM5). NCAR Tech. Note 398, 122pp.

Hendricks, E. A., M. T. Montgomery, and C. A. Davis, 2004: The role of "vortical" hot towers in the formation of Tropical Cyclone Diana (1984). *J. Atmos. Sci.,* **61,** 1209-1232.

Hendricks, E. A., and M. T. Montgomery, 2006: Rapid scan views of convectively generated mesovortices in sheared Tropical Cyclone Gustav (2002). Notes and Correspondence, *Wea. Forecasting,* **21,** 1041-1050.

Holton, J. R., 2004: *An Introduction to Dynamic Meteorology.* Fourth Edition, Elsevier Academic Press, 529 pp.

Hong, S.-Y., and H.-L. Pan, 1996: Nocturnal boundary layer vertical diffusion in a medium-range forecast model. *Mon. Wea. Rev.,* **124,** 2322-2339.

Houze, R. A., Jr., 1997: Stratiform precipitation in regions of convection: A meteorological paradox? *Bull. Amer. Meteor. Soc.,* **78,** 2179-2196.

Jorgensen, D. P., E. J. Zipser, and M. A. LeMone: Vertical motions in intense hurricanes. *J. Atmos. Sci.,* **42,** 839-856.

Kain, J. S., and J. Fritsch, 1990: A one-dimensional entraining/detraining plume model and its application in convective parameterization. *J. Atmos. Sci.,* **47,** 2784-2802.

Lawrence, M. B., and G. B. Clark, 1985: Annual summary: Atlantic hurricane season of 1984. *Mon. Wea. Rev.,* **113,** 1228-1237.

Liu, Y., D.-L. Zhang, and M. K. Yau, 1997: A multiscale numerical study of Hurricane Andrew (1992). Part I: Explicit simulation and verification. *Mon. Wea. Rev.,* **125,** 3073-3093.

Mapes, B. E., and R. A. Houze, Jr., 1995: Diabatic divergence profiles in western Pacific

mesoscale convective systems. *J. Atmos. Sci.,* **52,** 1807-1828.

McWilliams, J. C., 1984: The emergence of isolated coherent vortices in turbulent flow. *J. Fluid Mech.,* **146,** 21-43.

Möller, J. D., and M. T. Montgomery, 1999: Vortex Rossby waves and hurricane intensification in a barotropic model. *J. Atmos. Sci.,* **56,** 1674-1687.

Möller, J. D., and M. T. Montgomery, 2000: Tropical cyclone evolution via potential vorticity anomalies in a three-dimensional balance model. *J. Atmos. Sci.,* **57,** 3366-3387.

Montgomery, M. T., and R. J. Kallenbach, 1997: A theory for vortex Rossby waves and its application to hurricane spiral bands and intensity changes in hurricanes. *Quart. J. Roy. Meteor. Soc.,* **123,** 435-465.

Montgomery, M. T., and J. Enagonio, 1998: Tropical cyclogenesis via convectively forced vortex Rossby waves in a three-dimensional quasigeostrophic model. *J. Atmos. Sci.,* **55,** 3176-3207.

Montgomery, M. T., M. E. Nicholls, T. A. Cram, and A. B. Saunders, 2006: A "vortical" hot tower pathway to tropical cyclogenesis. *J. Atmos. Sci.,* **63,** 355-386.

Montgomery, M. T., and B. F. Farrell, 1993: Tropical cyclone formation. *J. Atmos. Sci.,* **50,** 285-310.

Nuss, W. A., and D. W. Titley, 1994: Use of multiquadric interpolation for meteorological objective analysis. *Mon. Wea. Rev.,* **122,** 1611-1631.

Ooyama, K., 1964: A dynamical model for the study of tropical cyclone development. *Geofis. Int.,* **4,** 187-198.

Ooyama, K., 1969: Numerical simulation of the life cycle of tropical cyclones. *J. Atmos.*

Sci., **26,** 3-40.

Ooyama, K., 1982: Conceptual evolution of the theory and modeling of the tropical cyclone *J. Met. Soc. Japan,* **60**, 369-379.

Pielke, R. A. and Coauthors, 1992: A comprehensive meteorological modeling system-RAMS. *Meteor. Atmos. Phys.,* **49**, 69-91.

Powers, J. G., and C. A. Davis, 2002: A cloud resolving regional simulation of tropical cyclone formation. *Atmos. Sci. Lett.*, **3,** 15-24.

Raymond, D. J., C. López-Carrillo, and L. López Cavazos, 1998: Case-studies of developing east Pacific easterly waves. *Quart. J. Roy. Meteor. Soc.,* **124,** 2005-2034.

Reasor, P. D., M. T. Montgomery, and L. D. Grasso, 2004: A new look at the problem of tropical cyclones in vertical shear flow: vortex resiliency. *J. Atmos. Sci.,* **61,** 3-22.

Reasor, P. D., M. T. Montgomery, and L. F. Bosart, 2005: Mesoscale observations of the genesis of Hurricane Dolly (1996). *J. Atmos. Sci.,* **62,** 3151-3171.

Ritchie, E. A., and G. Holland, 1997: Scale interaction during the formation of Typhoon Irving. *Mon. Wea. Rev.,* **125,** 1377-1396.

Ritchie, E. A., 2003: Some aspects of midlevel vortex interaction in tropical cyclogenesis. *Cloud Systems, Hurricanes, and the Tropical Rainfall Measuring Mission (TRMM), Meteor. Monogr.,* No. 51, Amer. Meteor. Soc., 165-174.

Rotunno, R., and K. Emanuel, 1987: An air-sea interaction theory for tropical cyclones. Part II: Evolutionary study using a nonhydrostatic axisymmetric numerical model. *J. Atmos. Sci.,* **44,** 542-561.

Rozoff, C. M., W. H. Schubert, B. D. McNoldy, and J. P. Kossin, 2006: Rapid filamentation zones in intense tropical cyclones. *J. Atmos. Sci.,* **63,** 325-340.

Schultz, P., 1995: An explicit cloud physics parameterization for operational numerical weather prediction. *Mon. Wea. Rev.*, **123,** 3331-3343.

Schumacher, C., R. A. Houze, Jr., and I. Kraucunas: The tropical dynamical response to latent heating estimates derived from the TRMM precipitation radar. *J. Atmos. Sci.*, **61,** 1341-1358.

Shapiro, L. J. and M. T. Montgomery, 1993: A three-dimensional balance theory for rapidly rotating vortices. *J. Atmos. Sci.*, **50**, 3322-3335.

Sheets, R. C., 1990: The National Hurricane Center—Past, present, and future. *Wea. Forecasting,* **5,** 185-232.

Simpson, J., E. Ritchie, G. J. Holland, J. Halverson, and S. Stewart, 1997: Mesoscale interactions in tropical cyclone genesis. *Mon. Wea. Rev.*, **125,** 2643-2661.

Sippel, J. A., J. W. Nielsen-Gammon, and S. E. Allen, 2006: The multiple vortex nature of tropical cyclogenesis. *Mon. Wea. Rev.*, **134,** 1796-1814.

Smith, R. K., 1997: On the theory of CISK. *Quart. J. Roy. Meteor. Soc.*, **123,** 407-418.

Tory, K. J., M. T. Montgomery, and N. E. Davidson, 2006: Prediction and diagnosis of tropical cyclone formation in an NWP system. Part I: the critical role of vortex enhancement in deep convection. *J. Atmos. Sci.*, **63**, 3077-3090.

Tory, K. J., M. T. Montgomery, and N. E. Davidson, 2006: Prediction and diagnosis of tropical cyclone formation in an NWP system. Part II: A diagnosis of Tropical Cyclone Chris formation. *J. Atmos. Sci.*, **63**, 3091-3113.

Yuter, S. E., and R. A. Houze, Jr., 1995: Three-dimensional kinematic and microphysical evolution of Florida cumulonimbus. Part II: Frequency distribution of vertical velocity, reflectivity, and differential reflectivity. *Mon. Wea. Rev.*, **123,** 1941-1963.

Zehr, R., 1992: Tropical cyclogenesis in the Western North Pacific. NOAA Tech. Rep. NESDIS 61, 181 pp.

APPENDIX

MODEL EQUATIONS

Pressure, temperature and density are defined as follows in terms of a constant reference state and perturbations from this state:

$$p(x,y,z,t) = p_0(x,y,z) + p'(x,y,z,t) \tag{A.1}$$

$$T(x,y,z,t) = T_0(x,y,z) + T'(x,y,z,t) \tag{A.2}$$

$$\rho(x,y,z,t) = \rho_0(x,y,z) + \rho'(x,y,z,t) \tag{A.3}$$

The vertical coordinate in the model is terrain following and defined as follows:

$$\sigma = \frac{p_0 - p_t}{p_s - p_t}, \tag{A.4}$$

where p_s and p_t are reference state pressures at the surface and at the model top, respectively. Given the reference state pressure (2.1) and the definition of the vertical coordinate (2.4), the total pressure at a grid point at a given time is:

$$p = p^* \sigma + p_t + p' \tag{A.5}$$

where:

$$p^*(x,y) = p_s(x,y) - p_t . \tag{A.6}$$

The model equations are from Dudhia (1993) and are given as follows:

Horizontal momentum:

$$\frac{\partial p^* u}{\partial t} = -m^2\left[\frac{\partial p^* uu/m}{\partial x} + \frac{\partial p^* vu/m}{\partial y}\right] - \frac{\partial p^* u\dot{\sigma}}{\partial \sigma} + uDIV$$

$$-\frac{mp^*}{\rho}\left[\frac{\partial p'}{\partial x} - \frac{\sigma}{p^*}\frac{\partial p^*}{\partial x}\frac{\partial p'}{\partial \sigma}\right] + p^* fv + D_u \tag{A.7}$$

$$\frac{\partial p^* v}{\partial t} = -m^2\left[\frac{\partial p^* uv/m}{\partial x} + \frac{\partial p^* vv/m}{\partial y}\right] - \frac{\partial p^* v\dot{\sigma}}{\partial \sigma} + vDIV$$

$$-\frac{mp^*}{\rho}\left[\frac{\partial p'}{\partial y} - \frac{\sigma}{p^*}\frac{\partial p^*}{\partial y}\frac{\partial p'}{\partial \sigma}\right] - p^* fu + D_v \tag{A.8}$$

Vertical momentum:

$$\frac{\partial p^* w}{\partial t} = -m^2\left[\frac{\partial p^* uw/m}{\partial x} + \frac{\partial p^* vw/m}{\partial y}\right] - \frac{\partial p^* w\dot{\sigma}}{\partial \sigma} + wDIV$$

$$+ p^* g\frac{\rho_0}{\rho}\left[\frac{1}{p^*}\frac{\partial p'}{\partial \sigma} + \frac{T_v'}{T} - \frac{T_0 p'}{T p_0}\right] - p^* g(q_c + q_r) + D_w \tag{A.9}$$

Pressure:

$$\frac{\partial p^* p'}{\partial t} = -m^2\left[\frac{\partial p^* up'/m}{\partial x} + \frac{\partial p^* vp'/m}{\partial y}\right] - \frac{\partial p^* p'\dot{\sigma}}{\partial \sigma} + p'DIV$$

$$-m^2 p^*\gamma\ p\left[\frac{\partial u/m}{\partial x} - \frac{\sigma}{mp^*}\frac{\partial p^*}{\partial x}\frac{\partial u}{\partial \sigma} + \frac{\partial v/m}{\partial y} - \frac{\sigma}{mp^*}\frac{\partial p^*}{\partial y}\frac{\partial v}{\partial \sigma}\right]$$

$$+ p_0 g\gamma\ p\frac{\partial w}{\partial \sigma} + p^*\rho_0 gw \qquad \text{(A.10)}$$

Temperature:

$$\frac{\partial p^* T}{\partial t} = -m^2\left[\frac{\partial p^* uT/m}{\partial x} + \frac{\partial p^* vT/m}{\partial y}\right] - \frac{\partial p^* T\dot{\sigma}}{\partial \sigma} + T\,DIV$$

$$+\frac{1}{\rho c_p}\left[p^*\frac{Dp'}{Dt} - \rho_0 g p^* w - D_{p'}\right] + p^*\frac{\dot{Q}}{c_p} + D_T, \qquad \text{(A.11)}$$

where

$$DIV = m^2\left[\frac{\partial p^* u/m}{\partial x} + \frac{\partial p^* v/m}{\partial x}\right] + \frac{\partial p^*\dot{\sigma}}{\partial \sigma} \qquad \text{(A.12)}$$

and

$$\dot{\sigma} = -\frac{\rho_0 g}{p^*}w - \frac{m\sigma}{p^*}\frac{\partial p^*}{\partial x}u - \frac{m\sigma}{p^*}\frac{\partial p^*}{\partial y}v. \qquad \text{(A.13)}$$

In the above equations, the D terms are horizontal, vertical and thermal diffusion terms. The $D_{p'}$ term is a correction to the thermal diffusion as a result of horizontal pressure differences.